12-2023

Developing High-Performance 2D Heterostructured Electrocatalysts and Photocatalysts for Hydrogen Production and Utilizationsts and Photocatalysts for Hydrogen Production and Utilization

Xiaohan Ma
xiaoham@g.clemson.edu

Recommended Citation

Ma, Xiaohan, "Developing High-Performance 2D Heterostructured Electrocatalysts and Photocatalysts for Hydrogen Production and Utilizationsts and Photocatalysts for Hydrogen Production and Utilization" (2023). *All Dissertations*. 3489.
https://tigerprints.clemson.edu/all_dissertations/3489

DEVELOPING HIGH-PERFORMANCE 2D HETEROSTRUCTURED ELECTROCATALYSTS AND PHOTOCATALYSTS FOR HYDROGEN PRODUCTION AND UTILIZATION

A Dissertation
Presented to
the Graduate School of
Clemson University

In Partial Fulfillment
of the Requirement for the Degree
Doctor of Philosophy
Material Science of Engineering

---

by
Xiaohan Ma
December 2023

Accepted by:
Dr. Jianhua Tong, Committee Chair
Dr. Luiz Jacobsohn
Dr. Ming Tang
Dr. Ming Yang

ABSTRACT

H_2 is a pivotal chemical in modern society, not only as a clean energy carrier but also as a versatile chemical reactant. However, traditional hydrogen production and utilization heavily rely on thermocatalysis, which is highly energy-intensive and can result in heavy carbon emission and severe environmental problems. Photocatalysis and electrocatalysis are greener alternatives to thermocatalysis that can capitalize on the renewable sunlight and electricity and thus dramatically reduce energy requirements. However, heterogeneous electro/photocatalysts are still far from application to hydrogen economy due to the lack of design principles that can lead to sufficient efficiency. To address this challenge, the dissertation primarily focuses on developing high-performance electrocatalysts and photocatalysts by understanding the impact of surface defects and interactions between different phases on catalytic performance. With the obtained understanding, electro/photocatalysts with high efficiency in H_2 production and utilization (herein, transfer hydrogenation) can be facilely fabricated. To better achieve an in-depth understanding of fabricating electro/photocatalysts used for the hydrogen economy, my thesis work starts with the research on H_2 evolution reaction (HER) via electrocatalysis, and then moves to the HER using the more challenging photocatalytic approach and finally proceeds to the most challenging part, photocatalytic transfer hydrogenation.

For electrocatalytic HER, MoS_2 nanosheets are in situ grown on carbon fiber paper for the fabrication of the proton exchange membrane (PEM) cell electrode. Impressively, this integrated electrode with an ultralow MoS_2 loading of 0.14 mg/cm^2 can achieve small cell voltages of 1.96 and 2.25 V under 1 and 2 A/cm^2, respectively, in a practical PEM cell, which is superior to most cells using noble-metal-free HER electrocatalysts even with extremely high catalyst loadings of 3~6 mg/cm^2 under the similar cell operation conditions. The ultrahigh

activity of the as-synthesized electrode is attributed to the intimate contact between MoS_2 and CFP, vertical alignment of MoS_2 nanosheets on CFP, the coexistence of 1T and 2H multiphase MoS_2 and the existence of various defects on MoS_2.

For photocatalytic HER, an Au nanocage/MoS_2 system is investigated to understand the effect of localized surface plasmon resonance (LSPR) on photocatalysis. The match between the LSPR wavelength of Au nanocages and the optical absorption edge of MoS_2 is found to be critical to the activity of the composite. When the match is achieved, a 40-fold activity increase over the bare MoS_2 is observed, while the other unmatched counterparts show much less activity enhancement (~15-fold). The near field enhancement (NFE) is proposed to govern the LSPR process with the energy of surface plasmon transferred from Au to MoS_2 to promote electron excitation in MoS_2, the efficiency of which maximized when the LSPR wavelength of Au matches the MoS_2 absorption edge.

In the photocatalytic transfer hydrogenation case, phenylacetylene (PA) semi-hydrogenation is selected as a model reaction to understand how vacancies in 2D semiconductors may be utilized to manipulate photocatalytic efficiency. 2D g-C_3N_4 nanosheets loaded with Ni single-atoms (SAs) are used as the catalyst for this reaction. By controlling both the Ni loading and the density of surface vacancies on g-C_3N_4, it is found that the numbers of vacancies and Ni SAs had a synergistic impact on the activity of the catalyst. Therefore, a fine tuning of both factors should be important to achieve an optimal hydrogenation activity.

Overall, all research examples highlight the important role played by surface defects and metal-semiconductor interactions, and the findings from the research can be potentially used to guide the design of high-performance photocatalysts for hydrogen evolution and hydrogenation reactions.

DEDICATION

This dissertation is dedicated to my parents, who are always supporting me both emotionally and financially. Thank you for gifting me the life to this world and guiding me how to realize the value of myself. I also want to express my sincere gratitude to my girlfriend Ziwei Liu, who has also been supporting me from every aspect of life. Life is always challenging, but with you it can be much easier to get through.

ACKNOWLEDGEMENT

First and foremost, I would like to express my appreciation to my advisors: Dr. Jianhua Tong and Dr. Zili Wu (Oak Ridge National Laboratory, ORNL). It is you who granted me the invaluable opportunity to conduct deep research work with high-end facilities in ORNL. Without your guidance, I cannot achieve what I have obtained so far. I am also grateful to my current and previous committee members: Dr. Luiz Jacobsohn, Dr. Ming Yang, Dr. Ming Tang and Dr. Kai He. Thank you for taking your valuable time to join my proposal, pre-defense and dissertation. Your suggestions and comments are of great value to my research.

Additionally, I would like to appreciate Yuanyuan Li, Xiang Wang, Yang He, Xinbin Yu, Weiwei Yang, Ilia Ivanov, Christopher Rouleau, David Geohegan, Harry Meyer III, Zhenghong Bao, Xiao Jiang, Jiawei Zhang and other group members and staff at Clemson University and ORNL. Your help, especially during my hard times, in my research greatly supports me and finally contributes to the completion of this dissertation.

Last but not least, all my works are supported by the GO! Program initiated by Center of Nanophase Materials Sciences (CNMS) in ORNL. This research is conducted as part of the theme science at the CNMS, which is a US Department of Energy, Office of Science User Facility at ORNL. I am sincerely grateful to this program and CNMS as it offers me the great opportunities to get involved in the frontier research in my field.

TABLE OF CONTENTS

Page

LIST OF TABLES

LIST OF FIGURES

CHAPTER ONE

INTRODUCTION

1.1 Research Background

"Hydrogen can play a pivotal role in transforming the world's clean energy options and infrastructure", as stated in the 2021 U.S. Department of Energy (DOE) Basic Energy Sciences Roundtable, for its "crucial global impact through its use as both an energy carrier (i.e., used as a fuel) and a chemical reactant (i.e., used in industrial processes)."[1] [as shown in **Figure 1.1 (a)**]. Considering the severe problems brought by the current fossil fuel economy like air pollution and global warming[2], a paradigm shift towards a low-carbon/carbon-neutral economy is needed. H_2 has an ultrahigh mass specific energy density (142 MJ/kg) and generates zero-emission during combustion[3], hence it has been recognized as the key component to creating a clean, sustainable energy system[4]. As a versatile reactant, H_2 can be used as the feedstock for processes like ammonia synthesis[5, 6], small alcohol synthesis (e.g., methanol[7] and ethanol[8]), hydrogenation of unsaturated hydrocarbons[9, 10], etc. Therefore, the hydrogen-dominated economy is considered as a promising greener alternative to the current fossil fuel economy.

The production process of H_2 requires H-containing chemical as the proton donor, as shown in **Figure 1.1 (b)**. Currently, the mostly used method for H_2 production is thermocatalysis [**Figure 1.1 (c)**]. Specifically, methane steam reforming (MSR) followed by water-gas shift (WGS) is widely used in the current industry, which uses natural gas (predominantly methane) and steam as feedstock and inevitably produced toxic CO and greenhouse gas CO_2 as the intermediate and byproduct, respectively[11, 12]. Additionally, given that the MSR process requires high temperature (typically 750 ~ 950 °C) and high pressure (typically 14 ~ 20 atm)[13], it is intensively energy-consuming and also a heavy carbon emitter.

As shown in **Figure 1.1 (c)**, electrocatalysis and photocatalysis have recently attracted a lot of attention in hydrogen industry for their milder reaction conditions (*e.g.* low temperature and ambient pressure[14]) compared with thermocatalysis and the use of renewable driving force (electrons or photons)[3]. Unlike thermocatalysis, which relies on heat from fossil fuels as the energy source, electrocatalysis uses the applied electric field (electrons) as the energy source and photocatalysis uses light (photons) as the energy source. The distinct driving force of photocatalysis and electrocatalysis weakens their dependence on temperature and thus has the potential to lead to net-zero hydrogen production. However, every coin has two sides. Shown in **Figure 1.1 (d)** are the major downsides of the two greener catalysis processes. For electrocatalytic HER, noble metals such as Pt and Ir are the mostly used catalysts for their outstanding stability and activity[15-17]. The high cost and criticality of the catalysts greatly limit their application. Therefore, noble-metal-free materials have been explored for electrocatalytic HER[17, 18]. But the activity and stability are still incomparable to noble metals and far from satisfactory. On the other hand, current photocatalysts for HER considerably suffer from their poor performance in electron-hole separation efficiency and sunlight usage[19, 20], which leads to the insufficient usable charge carriers generated in the catalyst system. This makes photocatalysis an even more challenging process than electrocatalysis, hindering its development. Therefore, for HER from both electrocatalysis and photocatalysis, more efforts are needed to address their challenges.

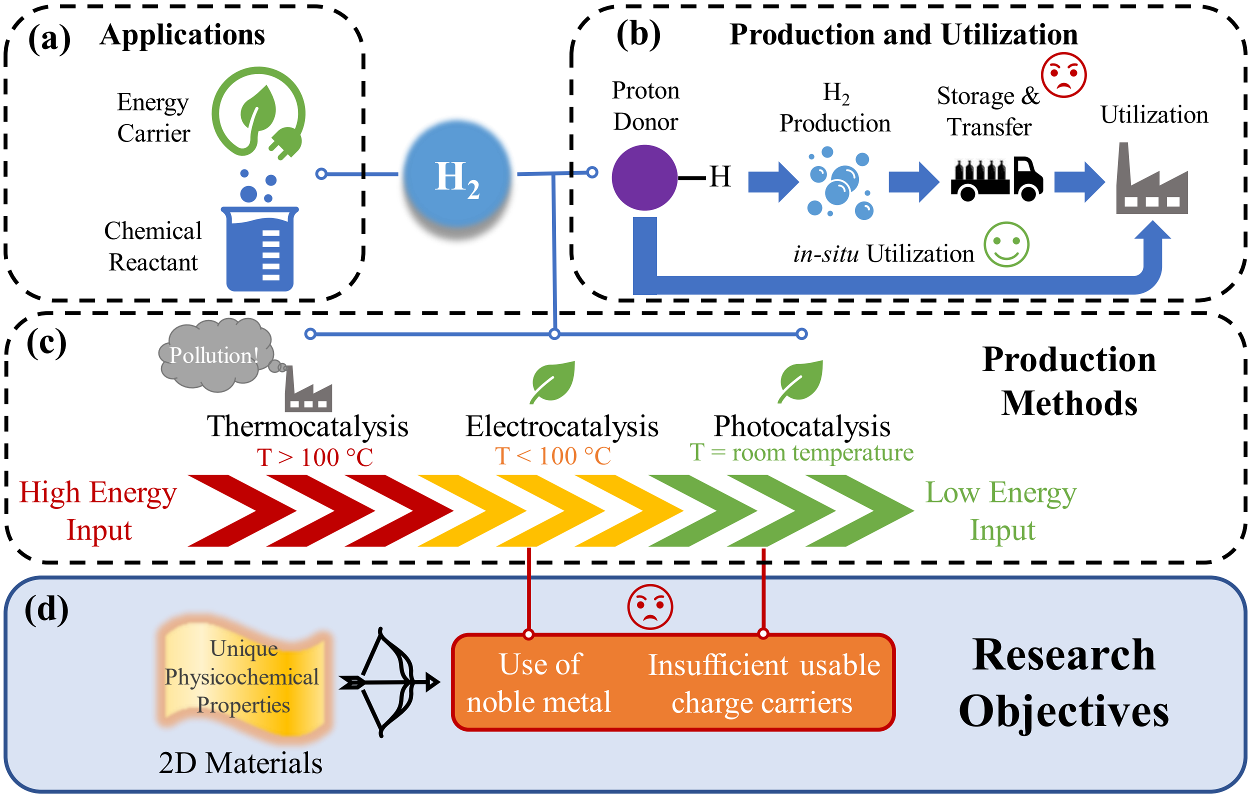

Figure 1.1 General scheme of the introduction

Additionally, it is noteworthy that H_2 is a gas at standard pressure and temperature, which results in its low volumetric energy density[21]. Therefore, methods like compression and liquefaction have been developed to efficiently store H_2[21, 22], which still have their limitations and can more or less increase the total cost in the hydrogen industry chain [**Figure 1.1 (b)**]. Therefore, when H_2 is used as the chemical reactant, the idea of "*in situ* utilization" of hydrogen is seemingly a better choice compared with storing H_2 before using. As illustrated in **Figure 1.1 (b)**, by omitting the challenging storage step and the following transportation step, it can considerably save the money and energy input and enhance the production efficiency of the hydrogen industry chain. So far, there are two main approaches for the "*in situ* utilization": (1) The H_2 gas is produced first as an intermediate product and then consumed immediately in the following reaction within the same system[23, 24]; (2) The H atoms from the H source can be directly used in reactions like transfer hydrogenation (TH) without the generation of H_2 gas[25, 26]. Apparently, compared with the stepwise utilization of H_2, TH is a direct pathway that omits the generation of H_2 gas. Besides, compared with pressurized H_2 gas, the H donors used in TH are usually small liquid organic acids and alcohols, which are readily available from renewable biomass, inexpensive and easier to handle under ambient conditions, which makes it a safer and simpler process[27] and hence, the dominantly studied one. Like HER, TH is commonly realized by thermocatalysis in industry as well. Although it usually requires much lower temperature (*c.a.* 100 - 300 °C)[28] than HER, once put into mass production, the elevated temperature can still cause considerable energy consumption and carbon emission. Similar to HER case, electrocatalysis and photocatalysis could also be greener substitutions for thermocatalysis in TH if their challenges can be well addressed. In general, the unsatisfied cost-activity balance is the major challenge of both electrocatalysis and photocatalysis, which greatly limits their mass industrial application. Therefore, the development of high-performance electrocatalysts and photocatalysts is eagerly desired to extend their applications in industry and convert the hydrogen production and utilization to economic and green processes.

As shown in **Figure 1.1 (d)**, two-dimensional (2D) materials have recently attracted intense research attention because dimensional reduction can lead to drastic changes in the electronic/chemical structures of 2D material compared with their 3D counterparts[29]. The unique physicochemical properties offer 2D material intriguing features like high specific surface area and rich options of host-guest species[30, 31], which makes it efficient and flexible to introduce extra active sites on them[29, 32]. This gives rise to the potential of 2D materials to address the challenges of electrocatalysis and photocatalysis. Specially for photocatalysis, the ultra-thin layer of 2D materials can greatly shorten the migration pathway of charges to the catalyst surface, which can efficiently suppress the electron-hole recombination[32-34]. Besides, due to the ultra-thin layered structure and high specific surface area, 2D material is a perfect platform to study the relationship between active sites and catalytic behavior at the atomic level. For example, compared with 3D bulk material, the types of active sites and the migration of charge carriers in 2D material are greatly limited due to the thin layered structure[32-34], making the manipulations on 2D materials easier to inspect. Meanwhile, the exposed surface atoms in the ultrathin 2D nanosheets can escape from the lattice easily to create surface vacancies, which provides a good opportunity for electronic, chemical, and structural modifications[29, 32]. Thanks to the high specific surface area of 2D materials, the effect of surface modification can be magnified and thus be characterized. All the above-mentioned superiorities of 2D materials strongly suggest that they are a promising “game changer” to overcome the aforementioned shortcomings of photocatalysts and electrocatalysts.

Concerning the above-mentioned merits and potential of 2D materials in electrocatalysis and photocatalysis, the objective of my research is focused on developing high-performance electrocatalysts and photocatalysts for hydrogen production and utilization by addressing the drawbacks of traditional bulk catalysts using 2D materials [**Figure 1.1 (d)**]. Therefore, it is necessary and helpful to briefly introduce the working mechanisms of H_2 production and TH using either electrocatalysis and photocatalysis as well as to review the recent advances and challenges of 2D materials used in these reactions to obtain clear motivations of my research.

1.2 Introduction to electrocatalytic H_2 production and transfer hydrogenation and the commonly used 2D electrocatalysts

1.2.1 Working mechanism of electrocatalysis

Electrocatalysis, as stated above, is a catalytic process that relies on an electric field to provide driving force for the reactions to occur. This concept incorporates two subdisciplines, namely, electrochemistry and catalysis, referring to the study of heterogeneous catalytic reaction that involves the electron transfer among reactants at the electrolyte-catalyst interface[35, 36]. Since in most cases, electrocatalysis is in nature an electrochemical process that is just sped up by a catalyst, the reaction process is quite analogous to the common electrochemical reaction (*i.e.*, water electrolysis). As shown in Figure 1.2, when the applied potential is high enough to overcome the barrier (known as overpotential, η) of the reaction in a given system, the electrons will be driven from the anode side to the cathode side[37]. Consequently, the oxidation reaction takes place on the anode side and the reduction reaction takes place on the cathode side. Meanwhile, in the electrolyte, the transfer of charge is realized by ion movement[38].

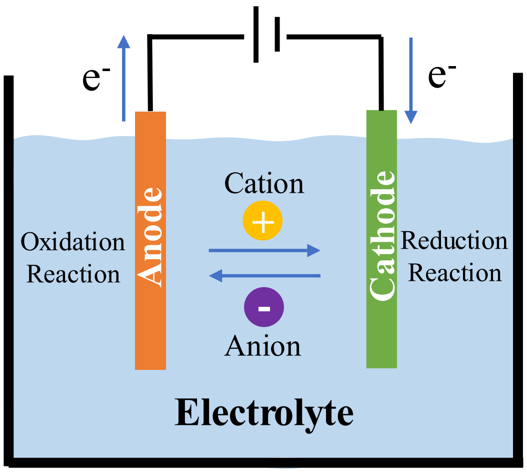

Figure 1.2 Scheme of the typical electrochemical reaction

1.2.2 Electrocatalytic H_2 production and transfer hydrogenation

For the electrocatalytic H_2 production, also known as hydrogen evolution reaction (HER), water is dominantly used as the proton source. This reaction can be carried out under either acidic or basic environment. The process basically contains two steps: (1) reduction and adsorption of the proton in hydronium cation (H_3O^+, Eq. 1) or water molecule (Eq. 2) in acidic or basic electrolyte, respectively (Volmer reaction); (2) the H_2 dissociation through one or both of the two processes, namely, the reaction between two adsorbed protons (Tafel reaction, Eq. 3) or the reaction between another proton source and the adsorbed proton (Heyrovsky reaction, Eq. 4 & 5)[37, 39]. Meanwhile, the HER is usually accompanied with the oxygen evolution reaction (OER) on the oxidation side, where H_2O (acidic environment) or OH^- (basic environment) is oxidized to O_2 to form an overall water splitting reaction[40], which is commonly called water electrolysis.

$$H_3O^+ + e^- \rightarrow H_{ads} + H_2O\ (acid) \qquad \text{Eq. 1}$$

$$H_2O + e^- \rightarrow H_{ads} + OH^-\ (alkline) \qquad \text{Eq. 2}$$

$$2H_{ads} \rightarrow H_2 \uparrow \qquad \text{Eq. 3}$$

$$H_3O^+ + H_{ads} + e^- \rightarrow H_2O + H_2 \uparrow (acid) \qquad \text{Eq. 4}$$

$$H_2O + H_{ads} + e^- \rightarrow OH^- + H_2 \uparrow (alkline) \qquad \text{Eq. 5}$$

For electrocatalytic TH, it is also a two-step process that usually involves water as the proton source. The proton in water is firstly reduced and adsorbed on the catalyst surface through Volmer reaction, which is the same as HER, followed by the hydrogenation reaction with the substrate that is adsorbed on the catalyst surface as well[41, 42]. However, as both electrocatalytic TH and HER rely on Volmer reaction to generate adsorbed protons, the activated protons also have the tendency to combine with each other and desorb as H_2, completing a typical HER process. This competition will inevitably lower the Faradaic efficiency (a parameter characterizing the percentage of electrons that are consumed in a desired reaction relative to the total electrons passed) of the desired hydrogenation process.

1.2.3 2D electrocatalysts for H_2 production and transfer hydrogenation

Due to the commonality shared by electrocatalytic HER and TH, their criterions on selecting catalysts are similar. However, it is noteworthy that when dealing with the TH, the selectivity requirement proposes a high standard on the design of the catalyst, which makes the development of TH electrocatalyst a more complicated research area. By far, the merits of noble metals still make them the most studied electrocatalyst materials in both reactions. Given the fact that the limited supply (criticality) of noble metal is the key factor limiting the development, many substitutions with earth abundancy have been developed such as (but are not limited to) non-noble metals (*e.g.,* Ni, Co and Cu), non-noble-metal-based materials (*e.g.,* oxide, nitride, carbide, dichalcogenide, phosphide and boride)[37] and nonmetallic material (*e.g.,* C, B and P-based material[43, 44]).

Considering the advantages of 2D materials, a lot of promising 2D electrocatalysts have also been developed in recent years. However, it is noteworthy that compared to HER, the development of TH using 2D electrocatalyst is still in its infancy. By far, most of the studies have targeted on small inorganic gas molecules like O_2, N_2 and CO_2.

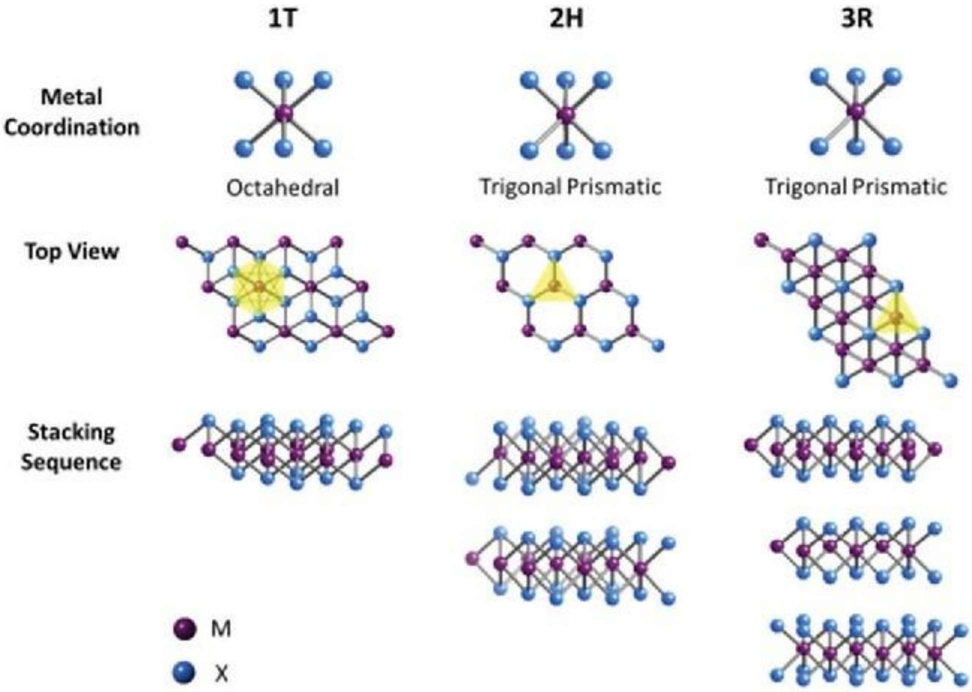

Figure 1.3 Metal coordination, top views and stacking sequences of the three main phases of TMD materials. Reproduced with permission from Toh *et al.*[45]. Copyright 2017, Royal Society of Chemistry

As a member of the non-noble-metal-based material, transition metal dichalcogenide (TMD) receives considerable attention for electrocatalytic HER due to its intrinsic 2D crystal structure and tunable layer-dependent electronic structure[46]. With a standard chemical formula as MX_2 (M: transition metal, X: S, Se or Te), its chemical phase can be changed by altering the stacking mode of X-M-X layer, forming three main phases, namely metallic 1T phase, semiconducting 2H phase and semiconducting 3R phase (**Figure 1.3**). However, as in some cases, the IT phase is not thermodynamically stable, a distorted 1T (1T') phase can usually be observed instead[47]. For 2D TMD materials, the commonly reported phases are 1T, 1T' and 2H. Due to the weak Van der Waals interaction between layers, the thickness and the resulting electronic properties of 2D TMD materials can be easily regulated[48]. The versatility of the electronic structure of TMD materials opens up opportunities for the design of highly efficient electrocatalysts for both HER and TH. Among the TMD family, MoS_2 is the most studied TMD material mainly due to the earth abundancy and excellent stability[49, 50]. As an HER catalyst, the S sites on the edge of the semiconducting 2H-MoS_2 nanosheets are the active sites in this reaction[51, 52]. However, its inert basal plane and poor conductivity limit the activity of MoS_2[53-55]. As a TH catalyst, it is the mainly reported to be a promising material for nitrogen reduction reaction (NRR)[56]. In NRR, Mo sites are regarded as the active center for N_2 fixation[57]. Like HER, the low activity is also a limitation of 2H-MoS_2 in NRR due to the lack of active sites on basal plane and the poor conductivity[56]. To address these two shortcomings, researchers turn to the metallic 1T-MoS_2, which indeed demonstrates a better performance than the 2H counterpart due to activation of basal sites and improved conductivity[56]. However, the metastability of this phase should be considered when designing the catalyst[58]. Therefore, the modifications of MoS_2 like the creation of S vacancies and holes and the partial phase transformation from 2H to 1T are necessary and have become a popular topic in recent years[49].

As a member of non-noble-metal-based carbide/nitride, MXene is also a promising group of 2D materials that is active for both electrocatalytic HER and TH. It has a general formula of $M_{n+1}X_nT_x$ (n = 1, 2 or 3), where M is an early transition metal, X is C or N, and T stands for surface terminations (*e.g.* -O, -OH and -F) inherited from the preparation process[59, 60]. The schematic illustration of MXene structure is shown in **Figure 1.4**. The superiorities of MXene can be concluded as follows: (a) excellent corrosion resistance under extremely acidic condition and electrooxidation environment[61]; (b) high electrical conductivity that facilitates the charge transfer through the material during the reaction[62]; (c) rich surface terminations that are pivotal to their electrocatalytic activity[63] and can also act as the anchoring sites for a variety of materials[60]. Therefore, MXene has been developed either as an electrocatalyst by itself (less common) or a conducting support for other electrocatalyst (more common) that usually has poor conductivity[44].

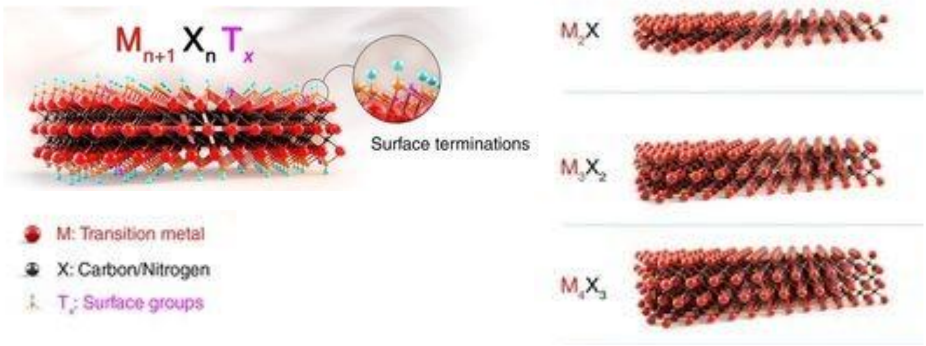

Figure 1.4 The crystal structure of MXene. Reproduced with permission from VahidMohammadi *et al.*[59]. 2021, Science.

Graphene, a star of 2D metal-free material famous for its outstanding conductivity, has also been reported to show activity on electrocatalytic HER and TH. However, the pristine graphene is electrochemically inert and has demonstrated low activity[64, 65]. The surface tailoring is again needed to improve the activity of graphene[43]. A more common way is to treat graphene as a 2D conducting support for other active electrocatalysts, which is the same role as MXene.

2D organic materials, namely metal organic framework (MOF) and covalent organic framework (COF), are also frequently studied. COF is featured by its high electron conductivity and facile electron migration[66, 67] while MOF is famous for the porous structure and abundant metal active sites[68, 69]. However, the applications of pristine MOF and COF in electrocatalysis are still quite challenging for their complicated synthesis procedure[70]. Besides, the pristine COF and MOF suffer a lot from the lack of active sites and the poor conductivity, respectively[71]. Consequently, further surface modification strategies are still necessary.

1.3 Introduction to photocatalytic production and transfer hydrogenation and the commonly used 2D photocatalysts

1.3.1. Working mechanism of photocatalysis

Photocatalysis, as stated previously, is a process driven by light/photons. The working mechanism of photocatalyst involves three significant steps: (1) light-harvesting to generate excited electron-hole pairs, (2) electrons-hole separation followed by migration to the catalyst surface, and (3) surface reduction reaction by electrons and surface oxidation reaction by holes[72, 73]. Obviously, photocatalyst is featured by the ability to absorb light which requires the material to have an energy gap in its electronic structure. Thus, the majority of photocatalysts are semiconductors, which are featured by valance band maximum (VBM) and conduction band minimum (CBM)[74]. Besides, some organic molecules can also be used as photocatalysts for their exhibition of semiconducting behaviors. These semiconducting molecules are featured by highest occupied molecular orbital (HOMO, analogous to VBM) and lowest unoccupied molecular orbital (LUMO, analogous to CBM)[74, 75]. However, as the semiconductors still dominate the photocatalyst materials, the terminology of VBM and CBM will be used for simplicity throughout the dissertation unless stated. The energy gap is then the energy difference between VBM and CBM, usually called bandgap. The working mechanism in energy space (K space) is schematically shown in **Figure 1.5** (a). Upon the irradiation of the light with the energy equal or higher than the energy gap of the material, electrons in the material will be excited from the VBM to the CBM, leaving the holes in the VBM[73, 74]. Consequently, the electrons will possess an energy equal to that of CBM and the holes will possess an energy equal to that of VBM. Therefore, it is apparent that no matter how high the energy of the incident light is, the energy and the corresponding redox potential of the electrons and holes are predetermined by the electronic structure of the material.

One can hardly expect a reaction to happen if the corresponding redox potential of the photocatalyst band edge (VBM or CBM) are lower than the requirement of the reaction. This leads to another significant difference between photocatalysis and electrocatalysis: in electrocatalysis, a given reaction can always happen if only the applied electrode potential is higher than the barrier of the reaction (including redox energy barrier and kinetic barrier). The potential, in the meantime, can be simply adjusted from the potentiostat. However, for photocatalysis, once the photocatalyst is fixed, the redox potential that the material can provide is then unchangeable. In other words, photocatalysis deals with both reaction kinetics and thermodynamics while electrocatalysts only need to deal with the reaction kinetics.

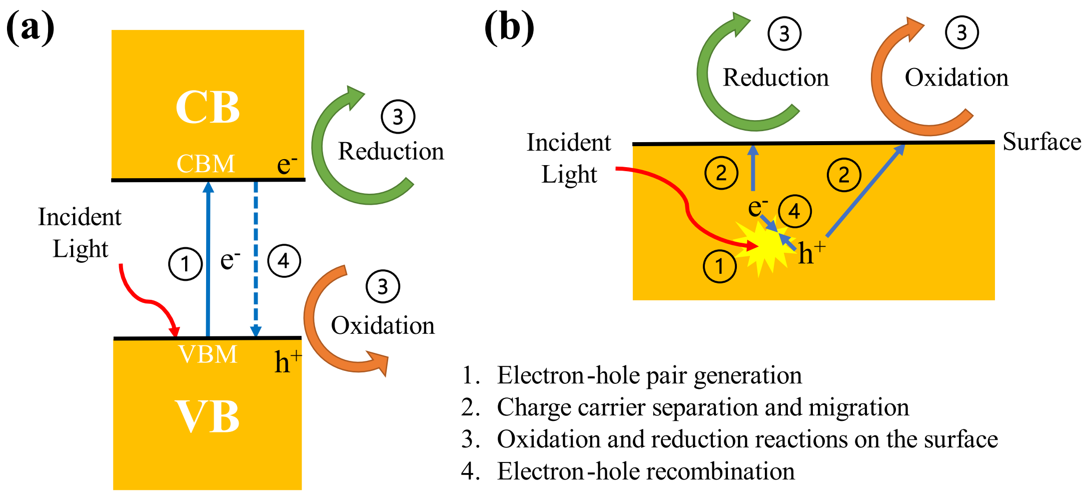

Figure 1.5 Working mechanism of photocatalysis in (a) K space and (b) real space.

Right after the excitation, the generated electrons and holes will start to migrate to the surface of the catalyst[73]. Since the movement of charge carriers takes place in the real space, it cannot be demonstrated in **Figure 1.5 (a)**. Therefore, **Figure 1.5 (b)** is a good illustration of what is happening in the photocatalyst. Then it is interesting to find that although the electrons and holes are much separated in K space, they are actually transporting in the same spatial region. Therefore, there is a great possibility for them to recombine with each other. The recombination is usually very fast (between picosecond and millisecond[76]), especially in the bulk of the photocatalyst[74]. The electron-hole recombination will cause a considerable loss to the quantum yield of photocatalyst, which is analogous to the Faradaic efficiency in electrocatalysis, reflecting the percentage of photogenerated electrons/holes used in the desired reaction[74, 77].

1.3.2 Cocatalysts and heterojunctions

Considering that the fast electron-hole recombination is one of the most severe challenges in photocatalysis, an impressive amount of work has been done to facilitate the real-spatial separation of electrons and holes. So far, there are two strategies that are mostly studied: (1) loading of cocatalysts and (2) construction of heterojunctions. The cocatalyst, usually metal, acts as the electron sink to attract photoelectrons, preventing them from recombining with holes[78]. As shown in **Figure 1.6 (a)**, the photoinduced electrons will transfer from the semiconductor to the cocatalyst, forming a Schottky junction at the interface[79]. Thus, when conducting reduction reactions, the cocatalyst will usually act as the active sites[80]. As the cocatalyst-semiconductor interaction is critical to the electron transfer between the two parts[80, 81], special care should be taken when designing this photocatalyst composite.

The heterojunctions are defined as the interface between two semiconductors with different electronic structures, which can result in the band alignment around the interface[82]. As shown in **Figure 1.6 (b-d)**, there are three main types of heterojunctions, namely type-I, type-II, and Z-scheme. Compared with the cocatalyst method, the fabrication of these heterojunctions is quite challenging. A general, facile, efficient, and economic methodology that can ensure the heterojunction interface with good morphology and contact has yet to be developed. Consequently, the loading of cocatalyst is still currently the best option for practical use in photocatalysis.

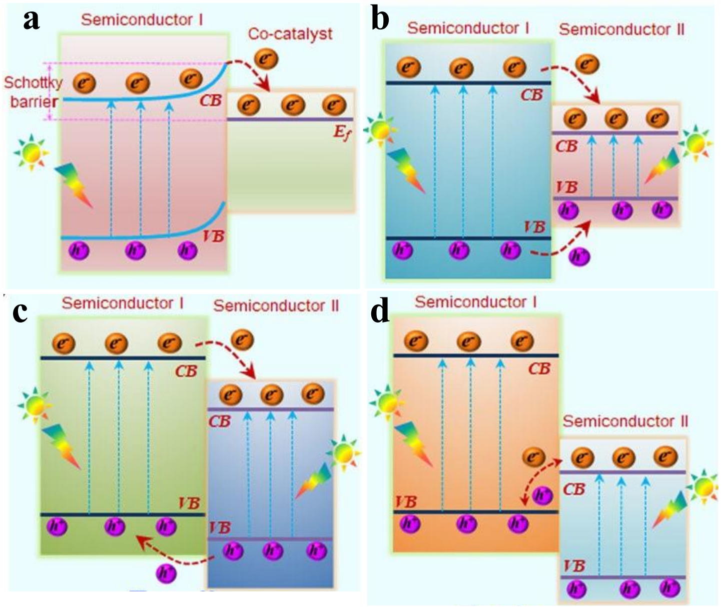

Figure 1.6 Illustration of photocatalyst with (a) cocatalyst, (b) type-I heterojunction, (c) type-II heterojunction and (d) Z-scheme heterojunction. E_f represents the Fermi level. Reproduced with permission from Ding *et al.*[79]. 2021, Wiley-VCH GmbH

1.3.3 Photocatalytic H_2 production and transfer hydrogenation

Due to the abovementioned benefits of cocatalysts, most of the photocatalytic HER and TH involves cocatalyst to produce an appreciable activity. Despite the different electron generating mechanism, the surface reduction mechanism of photocatalytic HER and TH are almost the same as the electrocatalytic ones.

Unlike electrocatalytic HER, the conventional study of photocatalytic HER usually uses hole scavengers to on the oxidation side to consume the photogenerated holes, a facile way to further suppress the electron-hole recombination. Scavengers are a class of chemicals that are ready to donate electrons. After the generation of holes, they will be instantly filled by the electrons from the scavengers, which can effectively increase the lifetime of the photogenerated electrons[83]. However, as the scavengers are dominantly small organics like amines, alcohols and acids[84], the use of which is costly in the real production process. Like electrocatalysis, the realization of overall water splitting is also the ultimate goal of photocatalysis. However, compared to HER, which is only a simple two-electron transferring process, OER is a complicated multi-step process that involves the transfer of four electrons and production of active intermediates[84]. As a result of the complexity of OER, the development of overall water splitting is quite limited compared with the HER half reaction that uses scavengers.

For the photocatalytic TH, alcohols and water are usually used as the proton source[85, 86]. The reaction pathway of the TH reactions (usually for small gas molecules like CO_2) using water is better understood compared with those with alcohols. Usually, water will be used as both proton source and solvent. After the oxidation of water by photogenerated holes, protons will be generated in the reaction solution. The free protons will then be consumed as the feedstock for the hydrogenation of the immobilized substrate initiated by the excited electrons[87, 88]. For the TH reactions of organic substrates like alkynes, alkenes and their aromatic derivatives, organic solvent like methanol and acetonitrile are usually used[85, 89]. As the free protons cannot be generated in the organic solvent, the proton transfer mechanism is currently still unclear.

1.3.4 2D photocatalysts used for H_2 production and transfer hydrogenation

As stated above, the requirements for photocatalysts are higher than electrocatalysts as the electronic structure of the photocatalyst must not only generate enough redox potential for the reaction, but also absorb appreciable amount of sunlight. TiO_2 has been traditionally regarded as an outstanding photocatalysts as its wide bandgap can initiate a wide range of reactions[90]. However, its absorption in the UV region and bulk nature limit its photocatalytic performance due to the fast electron-hole recombination and the inability to make use of visible light. Recently, 2D photocatalyst has become a promising option. Apart from the aforementioned physicochemical advantages, dimension reduction from 3D to 2D can drastically shorten the migration path of electrons and holes from bulk to surface. Considering that the recombination is especially severe in the bulk of photocatalysts (stated in Section 1.3.1), the ultrathin nature of 2D photocatalysts make it possible to address this challenge[91].

MoS_2, already introduced as a commonly used TMD electrocatalyst, is also a famous material in photocatalysis. However, the bulk MoS_2 is rarely used as the photocatalyst for HER due to its severe electron-hole recombination and narrow band gap[92]. Therefore, the mainstream strategy to utilize the merits of MoS_2 is to combine it with another facilitate the electron-hole separation by forming the Schottky barrier at the interface. By far, the discovered materials can be either plasmonic metals like Ag and Au[93] (which can generate electrons under illumination) or other photosensitive semiconductors like CdS and TiO_2[94]. In both cases, MoS_2 is actually doing the work as a "cocatalyst": attracting photogenerated electrons and acting as the reaction center. Therefore, in photocatalysis, MoS_2 is usually referred as a "cocatalyst" [94]. Differently, the monolayered 2D MoS_2 can be directly used as the photocatalyst for HER due to its suitable band structure[95] after the dimension reduction. However, although the ultrathin layer can suppress the electron-hole recombination, the strong exciton binding energy in 2D materials[96] will firmly "lock" the electron-hole pair, preventing them from forming free charge carriers[97]. This negative effect is considerably severe for monolayered MoS_2 due to its ultralow layer thickness. Therefore, there is still room for the activity enhancement of monolayered MoS_2. As introduced above, partially transforming 2H phase to 1T phase and combining MoS_2 with plasmonic species have been confirmed as effective strategies. Our group has already done a work on the former[95], hence, one of my work is focused on the latter, namely using plasmonic metal species to enhance HER activity of monolayered MoS_2, to further extend the limit of this fancy 2D material. However, unlike the classic heterogeneous photocatalysis with non-plasmonic metal cocatalyst, the design of the plasmonic photocatalyst system also deals with the optical interaction between the semiconductor and the metal species, not just the electron transfer across the interface. As the understanding of optical interaction has not been well established, it is still challenging to design the highly active MoS_2 based photocatalyst. Therefore, my research turns to enhance the MoS_2-based photocatalyst system by understanding the optical interaction between MoS_2 and the plasmonic species.

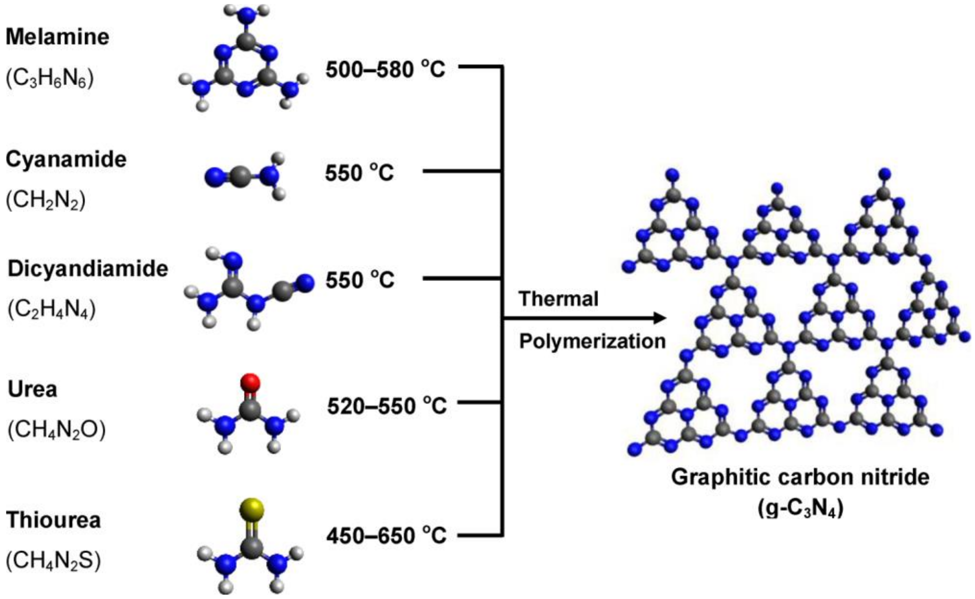

Figure 1.7 Illustration of the synthesis parameters and molecular structure of g-C_3N_4. Reproduced with permission from Ong *et al.*[98]. 2016, American Chemical Society

2D graphitic carbon nitride (g-C_3N_4) is another promising photocatalyst known for a few virtues: ultra-high specific surface area, earth-abundant metal-free composition, visible light activity and tunable chemical and electronic properties. The molecular structure is shown in **Figure 1.7**. Because of its similar composition and structure to graphene, this novel material is given the name “graphitic” and demonstrates an ultra-high theoretical specific surface area about 2500 m^2/g[99]. Meanwhile, as g-C_3N_4 is composed only by C and N, its precursors are usually cheap N-rich small organics like dicyandiamide, cyanamide, melamine, urea and thiourea[98], as summarized in **Figure 1.7**.

Combined with its facile synthesis method, namely thermal polymerization in air[98], g-C_3N_4 is a super competitive photocatalyst from the viewpoint of cost-efficiency. Moreover, according to the density functional theory (DFT) calculation, g-C_3N_4 has a narrow bandgap (~ 2.7 eV), which enables it to strongly absorb visible light (covers a photon energy range of 1.77 ~ 3.26 eV)[100]. The importance of visible light activity has been emphasized in recent years as visible light takes up ~ 43% energy of the sinlight[101]. As a comparison, the benchmark photocatalyst, TiO_2, can only utilize 3 ~ 4% of the sunlight irradiation due to its ultraviolet (UV) activity[102]. Besides, its chemical and electronical properties can be finely tuned by surface engineering strategies like doping[103], vacancy introduction[104] and functionalization[105], which makes g-C_3N_4 a quite versatile 2D photocatalyst. However, unlike graphene, the π-electrons in the g-C_3N_4 aromatic systems are localized[106], which significantly confined the mobility of the excited electrons in g-C_3N_4 under light illumination. The poor electron mobility directly leads to the poor electrical conductivity and further causes the severe electron-hole recombination of g-C_3N_4. Provided the outstanding merits of g-C_3N_4, it is chosen to be another studied photocatalysts in my research. However, efforts are needed to modify this material for better performance. As stated above, loading cocatalyst is a facile and effective solution and hence is adopted here.

Similar to TMD, 2D transition metal oxide (TMO) has also demonstrated considerable potential in photocatalysis. To date, there are two types of discovered 2D TMO: (1) TMD-like materials organized by the layer stacking via weak Van der Waals interaction and can usually be transformed into a 2D thin layer like MoO_3 and V_2O_5[48, 107]; (2) materials with intrinsic 3D structures but can be synthesized as 2D materials through self-assembly method like TiO_2, ZnO, Fe_2O_3, and Fe_3O_4 and MnO_2)[48, 108]. However, due to the complicated synthesis procedure, these materials are still under development.

Specially, 2D conducting materials like MXene and graphene are also widely used in photocatalysis. Although these materials are not photosensitive, they can be used as cocatalysts. Their high conductivity and specific surface area can excellently assist the electron-hole separation and increase the amount of active sites, respectively[19, 109].

1.4 Surface modification of 2D materials

As repeatedly stated above, surface modification is a crucial part for the improvement of 2D electro/photocatalyst performance. Therefore, some commonly used surface modification strategies are briefly reviewed in this section.

1.4.1 Surface vacancies

As one of the aforementioned merits of 2D materials, the instability of the surface atoms gives 2D materials a good opportunity for easy surface vacancy regulation. Generally speaking, as a type of 0D defects, surface vacancies can modify the electronic structure of material and/or act as the active sites for reactions[48, 88, 110, 111]. In photocatalysis, surface vacancies have more but somewhat contradictory impacts on the material. The benefits are their impressive contributions on promoting the visible light absorption and electron-hole separation by forming mid-gap defect levels[48, 88, 112]. However, it has been revealed that excessive vacancies can also act as electron-hole recombination centers, undermining the performance of the material[113]. Consequently, the subtle control is of great importance when introducing vacancies onto the photocatalysts.

As is has been introduced that a complete photocatalysis reaction involves to aspects: optical part (charge generation and migration) and surface reaction part, the discussion below will then focus on the impacts on surface reactions brought by different vacancies.

Basically, the surface vacancies can be classified into cation vacancies and anion vacancies, whereas vacancies of anions like O and S are more commonly studied due to their lower formation energy[114] and more widespread existence in various kinds of 2D TMO and TMD materials[48]. Specifically, O vacancies have been confirmed effective to provide reactive centers for CO_2, O_2 and N_2 adsorption and helpful to lower adsorption energy of these molecules due to the abundant localized electrons around the vacancies[115, 116]. Thus, the introduction of O vacancies will facilitate the TH of these gas molecules, namely $CO_2/O_2/N_2$ reduction reaction (CO_2RR, ORR and NRR, respectively). Meanwhile, S vacancies have not only demonstrated a similar impact as O vacancies in CO_2RR, but also in HER[117]. The S vacancies can act as the highly active sites for HER in TMD materials like MoS_2 and tune the hydrogen adsorption free energy (ΔG_H^*) close to zero, which is an optimal circumstance for HER catalysts. Bearing this in mind, S vacancies can be a powerful weapon to activate the basal plane of TMD materials[114]. Recently, N vacancies has also drawn a lot of attention due to the rise of g-C_3N_4 as a promising metal-free photocatalyst. Similar to O and S vacancies, the localized electrons around the N vacancies make them as the active sites for O_2 adsorption, which enables g-C_3N_4 for efficient oxygen reduction reaction (ORR), yielding H_2O_2 as the product[118].

On the other hand, cation vacancies also have considerable influence on the electronic structure and physicochemical properties of 2D materials because the cations in 2D materials are dominantly transition metals, which have various electron configurations and orbital distributions[119]. However, as a result of their high formation energy, it is challenging to introduce and manipulate cation vacancies, hindering the study of their functions[114]. Differently, as a metal-free material, g-C_3N_4 can easily form cation vacancies, *i.e.*, C vacancies. The introduction of C vacancies to g-C_3N_4 can enhance the adsorption of small molecules like NO, O_2, O_2, and H_2O by generating adsorption sites[120]. It has also been reported that the generation of amine functional groups around the C vacancies can become the preferred anchoring sites of the cocatalysts, leading to an intimate contact between the two parts[121].

1.4.2 Dopants

As another type of 0D defects, dopants can also have profound influence on the electronic structure of 2D materials. Similar to vacancies, the introduction of dopants can also optimize the adsorption behavior of molecules on the surface of the materials by redistributing the electron density[111]. In photocatalysis, the defect energy level can be generated as well, improving the visible light response and electron-hole separation of the material[48]. However, the more exciting fact is that dopants can enhance the conductivity of materials. As stated above, a lot of electrocatalysts suffer from low conductivity. Doping heteroatoms into the structure is seemingly a promising solution as its impact on conductivity is so profound that it has even been reported able to make the typical semiconductor show metallic characteristics (for example, zero bandgap and positively temperature-related electrical resistivity[122]).

1.4.3 Edge defects

Since TMD is a very important type of electro/photocatalyst for HER, extensive research has been done to optimize their performance through tailoring surface defects. As a natural defect in TMDs, the edge sites have been proved to be the active site for HER[52]. Thus, exposing more edge defect sites is essential to improve the HER activity of TMD materials[123]. To date, making pinholes on the basal plane of TMD materials has become a popular method because it can introduce extra edge sites to the basal plane[124, 125], activating it for HER. Moreover, the edge defects are not only valuable for TMD modifications, but also for graphene. It was reported that the edge C sites were more active than the basal-plane C sites in electrocatalytic ORR, which validates the merit and versatility of edge defect engineering.

1.5 Motivation and research design

As stated above, although electrocatalysis and photocatalysis are greener alternatives of the traditional thermocatalysis for HER and TH, their development is still challenging. For example, electrocatalysis severely suffers from the low activity of the cheap alternatives of noble metal catalyst and the development of photocatalysis is hindered by massive electron-hole recombination. Hence the objective of the dissertation is to develop high-performance electrocatalysts and photocatalysts for HER and TH through understanding and tuning the interfaces and defects in 2D material-based heterostructures. Based on all the information presented above, 2D materials possess superior properties like high specific surface area and ultrathin layer structure, which offers a great opportunity to construct catalysts with abundant surface active sites, highly tunable surface chemistry and suppressed electron-hole recombination. The high specific surface area also makes 2D materials a good platform to study the impact of tuning parameters on activity. Therefore, 2D materials are used in my research to address the challenges in electrocatalysis and photocatalysis.

As displayed in **Figure 1.8**, to achieve the dissertation goal , the research is divided into three parts. The first two parts are focused on HER. Due to the promising role played by 2D MoS_2 in HER, it is adopted in this two works. Given the current challenges and complexity in photocatalysis compared to electrocatalysis, despite its greener nature, I start with the research on electrocatalytic HER, which only deals with electronic properties, and then move towards photocatalytic HER, which deals with optoelectronic properties in addition to electronic ones. Finally, Part 3 continues to focus on photocatalysis but moves a step forward to the more complicated *in situ* TH. It has been introduced that defect engineering and interface construction (heterojunction) and tuning are of great potential for catalytic activity enhancement. Therefore, Part 1 and Part 2 aim to verify the positive effect of defects and interface tuning on the catalytic performance, respectively, while Part 3 synergizes the merits of defects and interface together to study the most challenging topic photocatalytic TH. Considering the highly tunable surface chemistry, g-C_3N_4 is chosen as an ideal platform to conduct this research. By following this sequential research map, the valuable insights acquired in the Part 1 & 2 (*e.g.*, how to defects and interface can positively influence the performance of catalyst) can be readily used as a guiding framework for the research of the most challenging Part 3.

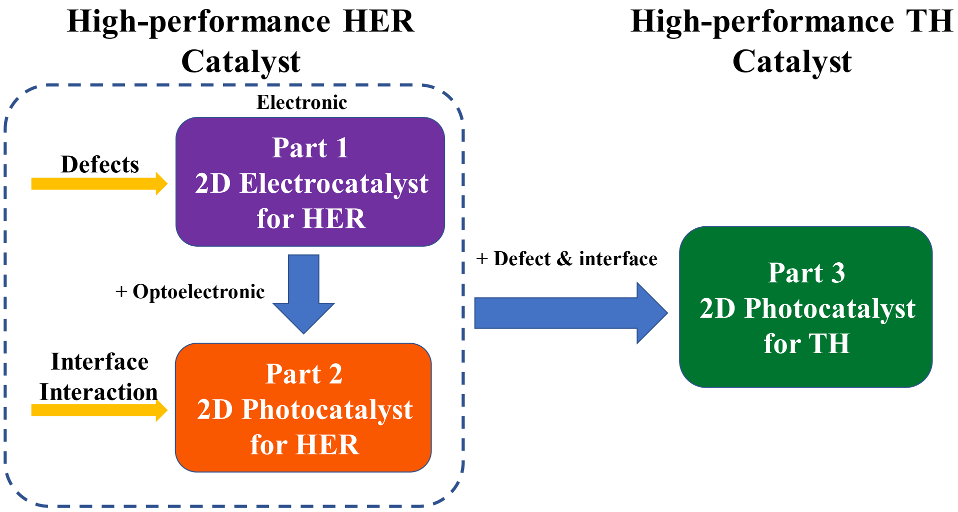

Figure 1.8 Outline scheme of the dissertation.

CHAPTER TWO

in situ GROWTH OF DEFECTIVE 2D MoS_2 NANOSHEETS ON CARBON FIBER PAPER FOR ELECTROCATALYTIC HYDROGEN EVOLUTION

2.1 Introduction

As illustrated in the research design map (**Figure 1.8**), the work on electrocatalytic HER is presented in this chapter. Herein, an electrocatalysis system called proton exchange membrane electrolyzer cell (PEMEC) was adopted as it is an outstanding and commonly used technique to efficiently generate high-purity H_2 from various renewable energy resources[126-129]. **Figure 2.1** schematically shows the typical water electrolysis process in PEMEC. The basic working mechanism is similar to the traditional electrochemical reaction system shown in **Figure 1.2**. However, instead of having free ions moving in the liquid electrolyte (*i.e.* salts, acids and bases, a solid polysulfonated membrane (Nafion, fumapem) is used in as the electrolyte to conduct only proton[130].

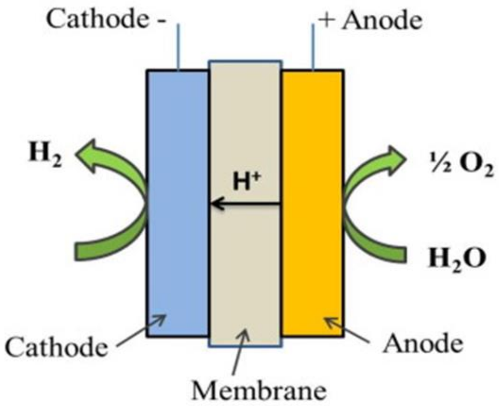

Figure 2.1 Illustration of water electrolysis in PEMEC. Reproduced with permission from Kumar *et al.*[130]. 2019, Elsevier

However, the practical application of PEMECs remains challenging due to the high loading (1~3 mg/cm^2) of platinum group metal (PGM) , scarcity of supply and costly electrode fabrication.[131-134] Therefore, it is highly urgent yet challenging to develop PGM-free or ultralow PGM-loaded electrocatalysts with competitive electrocatalytic activity, durability and low cost. In Chapter 1, it has already been discussed that MoS_2 is a promising noble-metal-free 2D electrocatalyst for HER, but the thermodynamically stable 2H-MoS_2 intensively suffers from the poor electrical conductivity and inert basal plane. The introduction of S vacancies, pinholes and extra exposed edge sites have been confirmed as effective strategies to activate its inert basal plane by maximizing the number of active sites. More recently, phase engineering of MoS_2 from semiconducting 2H phase into more catalytically active 1T phase by doping, plasma treatment and flash Joule heating can greatly enhance the intrinsic catalytic activities due to the excellent electrical conductivity and active basal plane of metallic 1T phase[135-140]. However, most methods reported up to date are of very limited application in practical water electrolyzers, mainly owing to their manipulation/synthesis complexity, poor scalability and high ohmic losses in the real cell. Furthermore, due to low intrinsic catalytic activity and conductivity, very high MoS_2 based catalyst loadings (3~6 mg/cm^2) are usually required in water electrolyzers to achieve acceptable cell performances at high current densities, leading to very limited cost reduction compared to PGM-based catalysts.[141-145]

To address the above challenges, we fabricate the integrated HER electrode by *in situ* growing vertically aligned MoS_2 nanosheets on highly conductive carbon fiber paper (CFP) via a facile one-step hydrothermal method. The as-synthesized MoS_2NS/CFP electrode are found to concurrently have multiple unique advantages as follows: (a) ideal 1T-2H phase integration can combine the excellent structural stability of 2H phase and the active basal plane and high conductivity of metastable 1T phase; (b) highly defective ultrathin nanosheets with rich exposed edges and additional basal-plane defects (pinholes, atomic sulfur vacancies) can further maximize the active sites on basal plane; (c) *in situ* growth method enables the intimate contact and strong adhesion of MoS_2 nanosheets and 3D porous conductive carbon support, resulting in significant reduction of ohmic losses and mass transport losses and remarkable stability enhancement in the practical electrolyzer cell. Benefitting from the above synergistic effects, the defect-rich 1T-2H MoS_2NS/CFP integrated electrode with an extremely low catalyst loading of 0.14 mg/cm^2 not only shows significantly improved HER performances in liquid acidic electrolyte, but also demonstrates outstanding cell performances in practical PEMECs. Under 1 and 2 A/cm^2, the required cell voltages are only 1.96 and 2.25 V, respectively. Such remarkable cell performances are superior to a lot of non-precious HER catalysts with much higher loadings of 3 ~ 6 mg/cm^2 under the similar cell operation conditions reported in the literature. The successful fabrication of the high-performance MoS_2NS/CFP electrode reveals that a suitable amount of surface and edge defects and strong interaction between different phases are quite beneficial to improve the electrocatalytic HER activity of the catalysts. Therefore, we believe the *in situ* growth method presented in this work builds up a bridge to connect catalyst optimization to electrode fabrication, which provides some insights into the general fabrication strategy of highly active electrocatalysts for HER.

2.2 Experimental

2.2.1 Fabrication of defect-rich 1T-2H MoS_2 nanosheet integrated electrodes

The 0.6 g sodium molybdate dihydrate ($Na_2MoO_4 \cdot 2H_2O$) and 1.2 g thioacetamide (C_2H_5NS) were dissolved in deionized water (20 mL) under continuous stirring at room temperature for 30 minutes. Then, the above 20 mL solution was added into a Teflon-lined autoclave (50 mL). The carbon fiber paper was vertically immersed into the reactor. Afterwards, the autoclave was well sealed and kept heating to 220 °C for 24 h in a box oven. After cool-down of the autoclave to room temperature for another 24 h, the sample was obtained and rinsed with water and alcohol for at least three times, respectively. Finally, the defect-rich 1T-2H MoS_2NS/CFP was obtained after drying at 60 °C overnight.

For comparison, MoS_2 assemblies/CFP electrodes were fabricated by a conventional spray coating method. The spray coated catalyst layer was composed of 80 wt.% MoS_2 assembly powders and 20 wt.% Nafion ionomer binders. The loading of MoS_2 assemblies was controlled to be 3.0 mg/cm^2 on the CFP support. The geometric area of MoS_2 assemblies/CFP electrode was 5 cm^2.

2.2.2 Characterizations

The SEM morphology and elemental mapping images were obtained from Zeiss Merlin scanning electron microscope coupled with energy-dispersive X-ray spectroscopy (EDX) detector from Oxford Instruments. The detailed structural information was characterized by aberration-corrected scanning transmission electron microscopy (STEM) on a JEOL JEM-ARM200F "NEOARM" operated at an acceleration voltage of 80 kV. The surface chemistry and phase composition were identified by X-ray photoelectron spectroscopy (XPS) analysis on a Thermo Scientific K-Alpha spectrometer. Raman spectroscopy was conducted on a multiwavelength Raman system at room and elevated temperatures. Raman scattering was measured by a triple Raman spectrometer (Princeton Instruments Acton Trivista 555). The 532 nm laser was applied as the excitation beam with a 30 s exposure time and 10 times accumulations. The sample stage is movable with a zigzag style in a dimension of 4 mm * 4 mm to check the homogeneity of measured sample and to minimize any potential laser damage.

2.2.3 Electrochemical measurements

The HER performances of defect-rich 1T-2H MoS_2/CFP and spray coated MoS_2 assemblies/CFP were compared via *ex-situ* electrochemical measurements in 0.5 M H_2SO_4 liquid electrolyte. Before electrochemical measurements, the electrolyte was de-aerated by continuously bubbling of high-purity Ar gas for at least 1 hour. The as-prepared defect-rich 1T-2H MoS_2/CFP or spray coated MoS_2 assemblies/CFP was employed as the working electrode, a graphite rod as the counter electrode and the Ag/AgCl reference electrode were used in the three-electrode system. The linear sweep voltammetry (LSV) data were collected by a Potentiostat (Bio-Logic) at a scan rate of 5 mV s^{-1}. Chronopotentiometry (CP) test of the working electrode was carried out under −10 mA cm^{-2} for 38 hrs. The electrochemical impedance spectroscopy (EIS) measurements were obtained between 100 KHz and 50 mHz.

2.2.4 The PEMEC assembly and testing

For the assembly of the PEMEC, the defect-rich 1T-2H MoS_2NS/CFP electrode or spray coated MoS_2 assemblies/CFP with the geometric area of 5 cm^2 was sandwiched between PEM surface and AXF-5Q graphite bipolar plate at cathode. The catalyst-coated membrane (CCM) with 3 mg/cm^2 $IrRuO_x$ catalyst (FuelCellEtc) coated on a Nafion 115 membrane (~ 127 µm in thickness) and a titanium-made liquid/gas diffusion layer (LGDL) were adopted at anode for all cell tests. Two stainless-steel endplates were used to compress the PEMEC (4.52 N·m of torque). The PEMEC performance comparison between defect-rich 1T-2H MoS_2NS/CFP electrode and spray coated MoS_2 assemblies/CFP were carried out at 80 °C and atmosphere pressure with a water flow rate of 20 ml/min at anode. The active area of the PEMEC was controlled to be 5 cm^2. As the baseline, commercial CCMs with IrRuOx (3.0 mg/cm^2) at the anode, Pt/C (0.2 mg_{Pt}/cm^2) at the cathode, and Nafion 115 with a thickness of 127 µm as the PEM were tested in the PEMEC. The polarization curves were measured on a Potentiostat (VSP/VMP3B-100, Bio-Logic). The EIS plots were recorded under 0.2 A/cm^2 between 100 KHz and 50 mHz.

2.3 Results and discussion

2.3.1 Structure and morphology of defect-rich 1T-2H MoS_2

Although the edge S sites have been widely recognized as the intrinsic active sites of MoS_2 for HER, the real performance of the electrode can depend on many factors and will be affected by the geometrical factors. The triple phase boundary (TPB) sites hence become the real active site in electrocatalytic reactions, which requires the intrinsic active sites to be accessible to water, electrons and electrolyte at the same time in this system. As depicted in **Figure 2.2 (a)**, a conventional PGM-free electrode for the HER in a PEMEC is commonly fabricated by the spray coating of ionomer-mixed catalyst ink onto the 3D porous media such as CFP substrate. In this electrode, large MoS_2 assemblies and a certain quantity of Nafion binders are mixed to form a non-uniform catalyst layer on the CFP substrate. It is obvious that the geometry and aggregation issues of the MoS_2 assemblies greatly limit the accessibility of water and electrolyte to the MoS_2 nanosheets in the assemblies, and the poor electrical conductivity of the Nafion binders significantly limit the availability of electrons on MoS_2. As a result, the available TPB sites for the HER are limited in this conventionally spray-coated electrode. Furthermore, the poor electrical conductivity caused by the binders can also result in large ohmic losses.

To this end, as illustrated in **Figure 2.2 (b)**, we design and synthesize novel MoS_2 ultrathin nanosheets *in situ* grown on CFP with desirable phase composition, defects and morphology via a one-step hydrothermal method, forming the defect-rich 1T-2H MoS_2NS/CFP integrated electrode for both liquid and solid electrolyte-based water electrolyzers. Unlike the spray-coated electrode, the *in situ* growth of MoS_2 nanosheets on CFP can get rid of the binders and create an intimate contact between the MoS_2 and CFP. Also, the nanosheets can be vertically aligned on the carbon fibers, enhancing the accessibility of MoS_2 nanosheets to the electrolyte and water. Both of the merits can increase the available TPB sites in this electrode. Additionally, the absence of binders can largely decrease the ohmic loss, giving this electrode another superiority over the spray-coated counterpart.

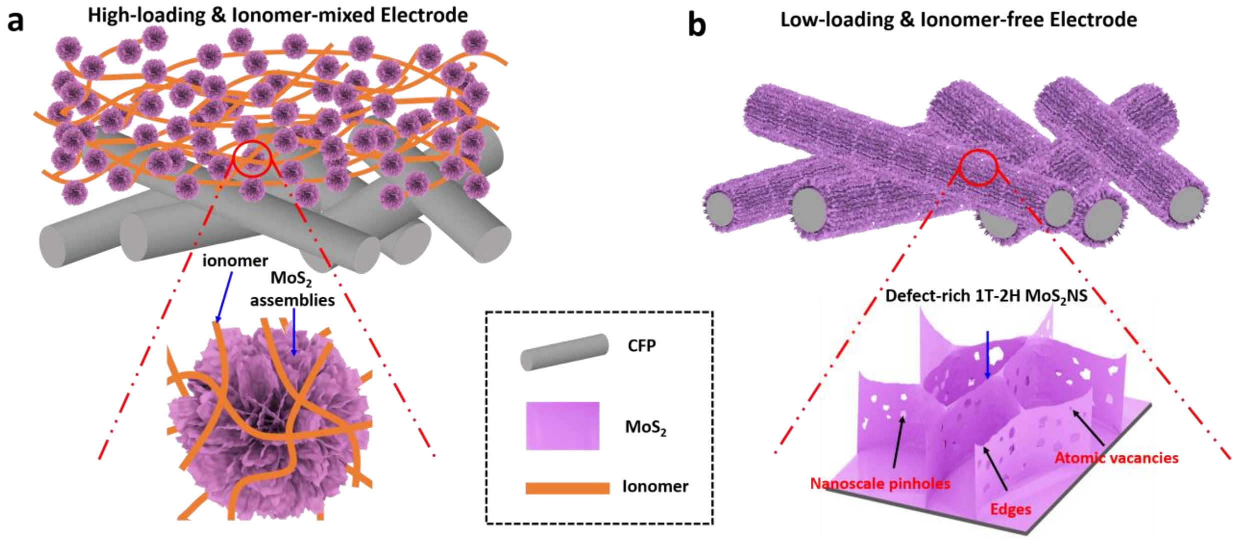

Figure 2.2 Schematic illustration of PGM-free electrode designs for the HER in a PEMEC. (a) A conventional electrode with spray coated high-loading MoS_2 powders mixed with ionomer. (b) Ionomer-free electrode with *in situ* grown ultralow-loading and defect-rich 1T-2H MoS_2 nanosheets. Reproduced with permission from Xie, Ma *et al.*[146]. 2022, Elsevier

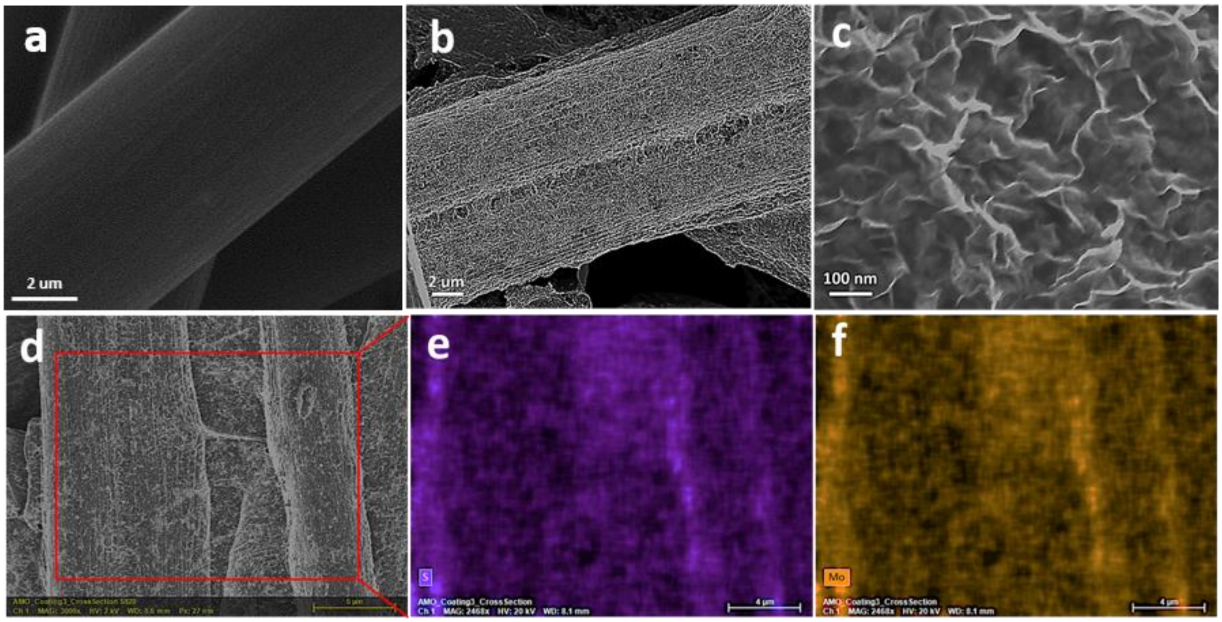

Figure 2.3 (a) SEM image of CFP. (b, c, d) typical SEM images of defect-rich 1T-2H MoS_2NS/CFP, and SEM-EDX mapping images of (e) S and (f) Mo, respectively. Reproduced with permission from Xie, Ma *et al.*[146]. 2022, Elsevier

With the help of SEM technique, the morphology difference between the electrodes fabricated via the two methods stated above can be visualized. The CFP substrate is composed of individual carbon fibers with relatively smooth surfaces, as shown in **Figure 2.3 (a)**. The SEM images in **Figure 2.3 (b)** and **(c)** indicate the successful growth of numerous vertically aligned nanosheets on the CFP substrate with a large quantity of exposed edge sites. The SEM-EDX mapping images in **Figure 2.3 (d-f)** verify the homogenous elemental distribution of S and Mo in the integrated electrode. By comparison, the SEM images in **Figure 2.4** show that conventional spray coated MoS_2 assemblies/CFP are composed of large assemblies on the CFP with Nafion ionomer binders, and the ionomer mixed catalyst layer is not uniformly distributed across the entire carbon fibers. As explained previously, the non-uniformity and large assemblies of the MoS_2 catalyst layer on the CFP would result in insufficient TPB sites for reactions and large ohmic losses in a PEMEC.

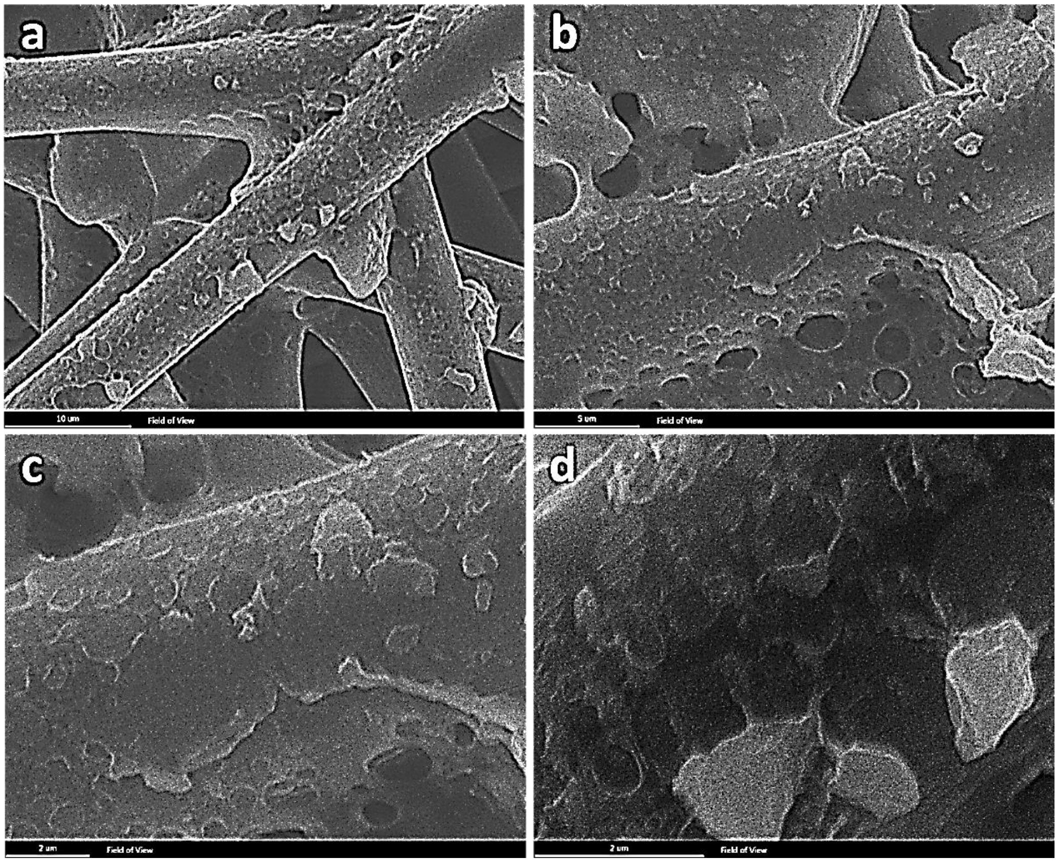

Figure 2.4 Typical SEM images of spray coated MoS_2 assemblies/CFP electrode. Reproduced with permission from Xie, Ma *et al.*[146]. 2022, Elsevier

To better visualize the nanostructure of MoS_2 nanosheets, the HAADF-STEM characterizations were carried out. As seen from **Figure 2.5 (a-c)**, highly distorted edges such as folds, sharp vertices and propagating ridges are all identified within different MoS_2 nanosheets. The lateral size of nanosheets is estimated to be 50 ~ 100 nm. The calculated thickness of the whole nanosheets is about 3.9 ~ 5.2 nm, corresponding to 6 ~ 8 layers of MoS_2. To further scrutinize the structure of MoS_2 basal planes at nanoscale, both the areas near the edges and on the basal plane are highlighted in **Figure 2.5 (d-f)**. Interestingly, it is found that nanoscale pinholes (1 ~ 2 nm) and atomic vacancies co-exist on the basal plane, as marked by yellow and red dash lines. Furthermore, as seen from **Figure 2.5 (e)** and **(f)**, the edges of the nanosheets with a few clear steps in the flat area indicate that edges of MoS_2 nanosheets are mainly composed of 1 ~ 3 layers. It is noted that the presence of bilayer MoS_2 is also verified, as marked by a purple dash line in **Figure 2.5 (f)**.

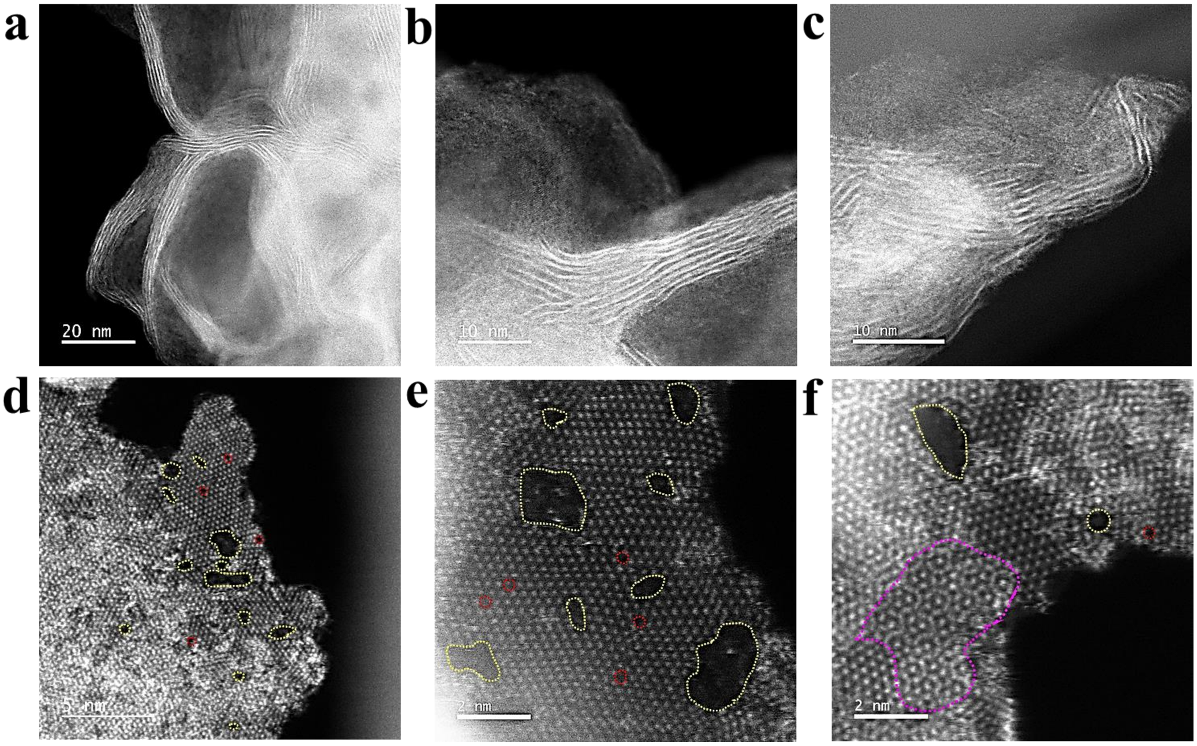

Figure 2.5 HAADF-STEM images of defect-rich 1T-2H MoS_2NS/CFP, confirming the co-existence of edges, pinholes & atomic vacancies. Reproduced with permission from Xie, Ma *et al.*[146]. 2022, Elsevier

The possible explanations for the formation of different phases and various defects in the MoS_2 nanosheets in the 1T-2H MoS_2NS/CFP are as follows. As introduced in the Experimental section, sodium molybdate dihydrate ($Na_2MoO_4 \cdot 2H_2O$) and thioacetamide (C_2H_5NS) are used as the Mo and S source, respectively, and water is used as the only solvent for the *in situ* synthesis of MoS_2 nanosheets on the CFP support without the requirement of any additive, pH adjuster or stabilizer. Based on the literature, Mo (IV) species play a dominant role in the formation of 1T-phase MoS_2 under hydrothermal or solvothermal conditions.[147, 148] The proposed formation mechanism of 1T-2H MoS_2 nanosheets is as follows. Initially, Mo (VI) species are reduced to Mo (IV), which usually appears in an octahedral coordination in [MoO_6]. Subsequently, the sulfurization proceeds by replacement of O^{2-} ligands in the [MoO_6], resulting the 1T-phase MoS_2 with the retained octahedral coordination structure. With the prolonged reaction time, the consumption of the $CS(NH_2)_2$ leads to the reduced Mo (IV) species, which allows the formation of the 2H-phase MoS_2. Finally, the integration of 1T and 2H phases is *in situ* grown on the CFP. The defects within 1T-2H MoS_2 nanosheets are formed during the synthesis because of the excess thiourea, which can restrict the oriented crystal growth via adsorption on the surface of MoS_2 primary nanocrystals to some extent.

2.3.2 Phase and chemical states of defect-rich 1T-2H MoS_2

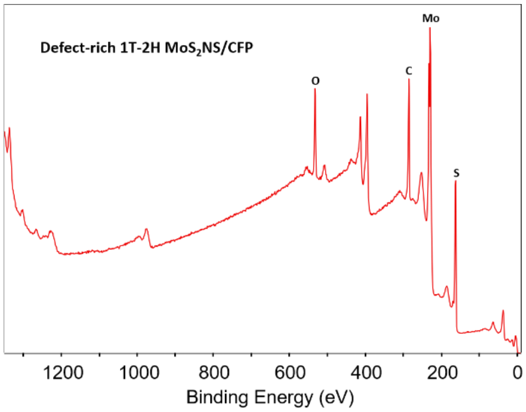

Figure 2.6 XPS full survey of defect-rich 1T-2H MoS_2NS/CFP electrode. Reproduced with permission from Xie, Ma *et al.*[146]. 2022, Elsevier

The XPS was performed to analyze the surface chemistry and phase composition of defect-rich 1T-2H MoS_2/CFP integrated electrode. The full survey in **Figure 2.6** shows the overall surface composition of Mo, S, O, C, and a small amount of N. As seen from the high-resolution XPS spectra of Mo 3d + S 2s in **Figure 2.7 (a)**, the Mo 3d, which overlaps with S 2s, shows several features. One Mo 3d doublet is assigned to the “1T”, and a second Mo doublet is assigned to “2H”. These results are well consistent with the literatures.[149-152] Along with them, two Mo satellites belonging to the “1T” and “2H” configurations and two S 2s peaks are also observed. Based on the calculation from the peak fit for high-resolution spectra of Mo 3d, the 1T/2H phase ratio is determined to be 1.56, indicating that 1T phase is predominant in MoS_2 nanosheets. In **Figure 2.7 (b)**, the high-resolution XPS spectra of S 2p show two doublets. One is assigned to S-Mo and the other is assigned to S-C bonding. The presence of S-C bonding strongly confirms the *in situ* growth of MoS_2 onto CFP instead of physical deposition or coating and directly proves the intimate contact between the MoS_2 nanosheets and the CFP support, which then gives rise to the large amount of the available TPB sites in this material. Additional evidence of C-S bonding in **Figure 2.7 (c)** also indicates the existence of chemical bonding between the catalyst and CFP. The high-resolution of C 1s shows the presence of both C-C bonding and C-S bonding. Raman spectroscopy was utilized to further confirm the phase composition of MoS_2 in defect-rich 1T-2H MoS_2NS/CFP integrated electrode. As seen from **Figure 2.8**, the distinct strong signal at 150 cm^{-1} is caused by the cut off of the laser filter and the J_1 mode of 1T phase might be buried under. The distinct phonon modes at 218 (J_2) and 327 cm^{-1} (J_3) can be assigned to the 1T super lattice structure. The broadening of 407 (A_{1g}) and 376 cm^{-1} (E^1_{2g}) modes are mainly attributed to the 2H phase of MoS_2. Therefore, ultrathin MoS_2 nanosheets in the integrated electrode are composed of both 1T and 2H phases.

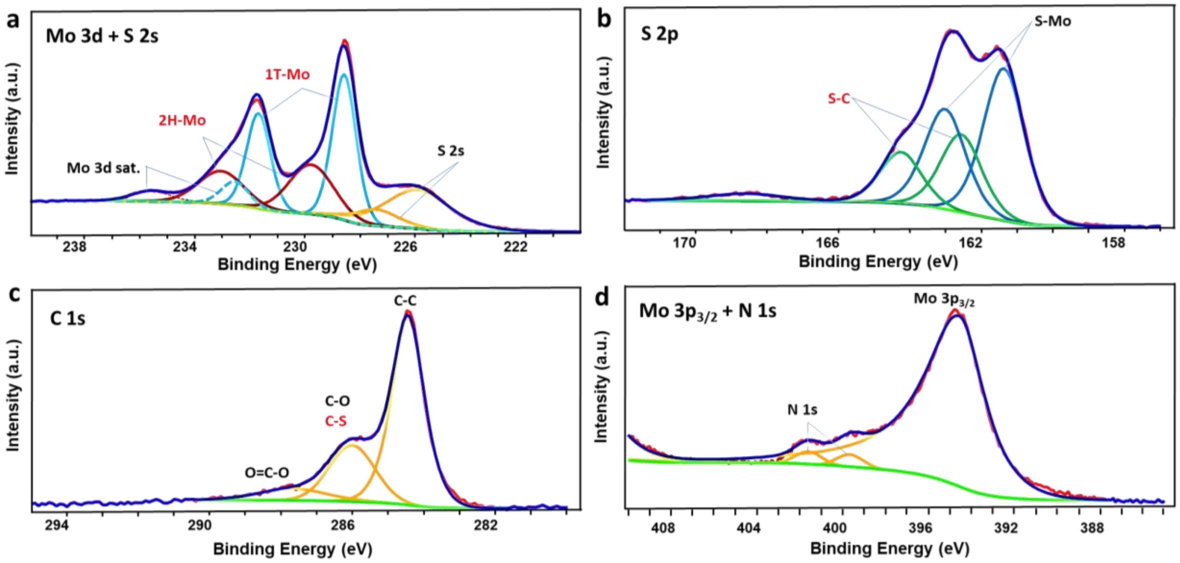

Figure 2.7 High-resolution XPS spectra of defect-rich 1T-2H MoS_2NS/CFP. (a) Mo 3d + S 2s, (b) S 2p, (c) C 1s and (d) Mo 3p + N 1s, respectively. Reproduced with permission from Xie, Ma *et al.*[146]. 2022, Elsevier

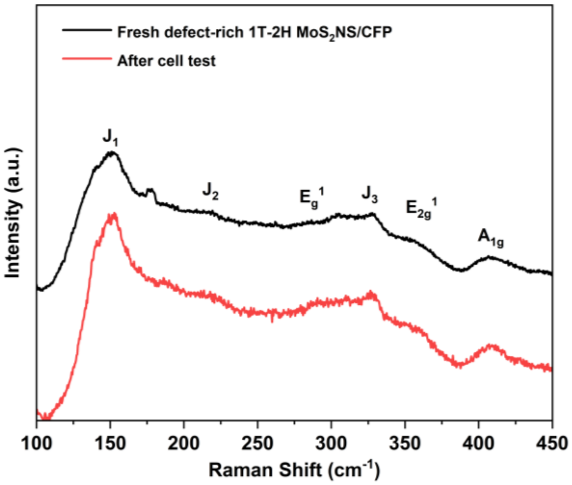

Figure 2.8 Raman spectra of defect-rich 1T-2H MoS_2NS/CFP electrode before and after the electrolyzer cell test. Reproduced with permission from Xie, Ma *et al.*[146]. 2022, Elsevier

The above SEM, HAADF-STEM, XPS and Raman characterizations collectively reveal that 1T-2H MoS_2 nanosheets with rich defects such as exposed highly distorted edges, basal-plane pinholes and atomic vacancies are successfully *in situ* grown on CFP substrate, with strong chemical coupling between catalyst layer and conductive substrate. We anticipate that the rich defects (vacancies and pinholes) would activate conventional “inert” 2H-MoS_2 basal planes with additional catalytically active sites, the existence of 1T phase leads to even more basal plane active sites and the ultrathin vertical-aligned nanosheets that are chemically bonded onto CFP would enhance the electrical conductivity in MoS_2 nanosheets and between the MoS_2 catalyst layer and the substrate.[153] Therefore, both catalytic activity of the integrated electrode should be boosted for HER application in practical acidic water electrolyzers.

2.3.3 Catalytic performances in liquid electrolyte

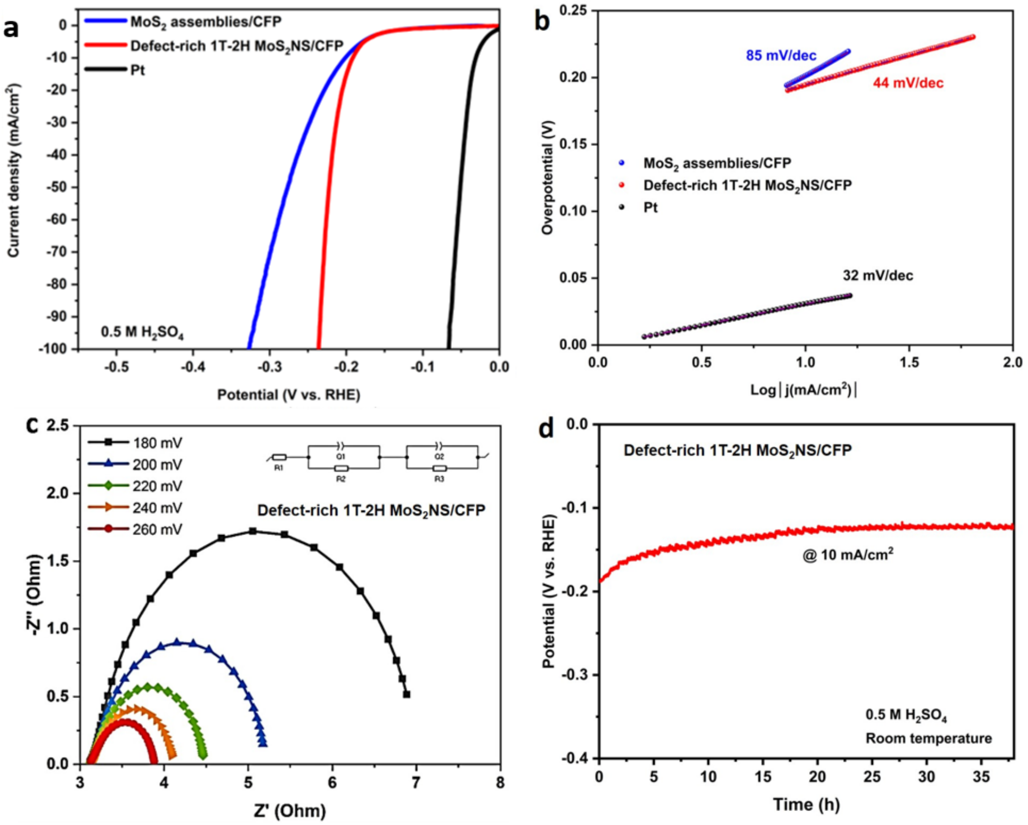

Figure 2.9 (a) Polarization curves of defect-rich 1T-2H MoS_2NS/CFP and MoS_2 assemblies/CFP. (b) Corresponding Tafel plots. (c) Nyquist plots of defect-rich 1T-2H MoS_2NS/CFP at various overpotentials. (d) Electrode stability test of defect-rich 1T-2H MoS_2NS/CFP at 10 mA/cm^2 for over 38 h. Reproduced with permission from Xie, Ma *et al.*[146]. 2022, Elsevier

To validate our hypothesis that the defect-rich and multiphase features of MoS_2 nanosheets and the intimate contact between MoS_2 nanosheets and CFP can lead to a better HER activity, electrochemical characterizations of MoS_2NS/CFP integrated electrode and spray coated

MoS_2 assemblies/CFP were conducted in 0.5M H_2SO_4 at room temperature. The MoS_2 catalyst loading in the integrated electrode is 0.14 and 3.0 mg/cm^2 for MoS_2NS/CFP and MoS_2 assemblies/CFP. As shown in **Figure 2.9 (a)** and **(b)**, the integrated electrode exhibits a low overpotential of 192 Mv (at 10 mA/cm^2) and small Tafel slope of 44 mV/dec, outperforming MoS_2 assemblies/CFP (202 mV 85 mV/dec) and a lot of previous results of MoS_2-based catalysts in the literatures. As seen from the Nyquist plots in **Figure 2.9 (c)**, the plots all display the similar single arc impedance properties at each overpotential, suggesting that the stable and similar electrochemical processes occur at all overpotentials tested between 180 and 260 mV. The charge transfer resistance can then be obtained by measuring the diameter of the EIS arcs and the derived results of the electrode were 3.679, 1.897, 1.145, 0.657 and 0.263 Ω at overpotentials of 180, 200, 220, 240 and 260 mV, respectively, indicating the ultrafast Faradaic process and a superior kinetics for HER. The measured small transfer resistances can be attributed to the synergetic effects of the integrated electrode, in which the intimate contact between MoS_2 and CFP ensures fast electron transport from CFP substrate to both MoS_2 edge sites and activated basal planes with more defects as active sites for HER.

To study the electrode durability during long-term operation, the 38-h electrochemical stability test at 10 mA/cm^2 was performed. As seen from **Figure 2.9 (d)**, gradual activation may proceed in the first 20 hours and then the overpotential keeps stable for the rest of test. No obvious catalyst or electrode degradation is observed in liquid acidic electrolyte, indicating high electrode durability in long-term operation. There are two possible reasons for this gradual activation phenomenon. Firstly, we hypothesize that more liquid electrolyte may gradually penetrate into the whole catalyst layer and then increase more active sites for the HER in the first 20 h-testing. Afterwards, the liquid electrolyte may saturate the whole catalyst layer and stabilize the HER performance in the rest of 18 h-testing. Secondly, a possible surface reconstruction (*e.g.*, extra edge distortions and defects) may occur in MoS_2 nanosheets, probably creating more active sites for the HER and resulting in gradual activation of catalysts in the first 20 h-testing. However, such gradual activation phenomenon is still not fully understood. In the future, *in situ* characterizations (e.g., *in situ* TEM and *in situ* Raman) would be warranted to better understand the gradual activation mechanism.

2.3.4 Full cell characterization in PEMECs

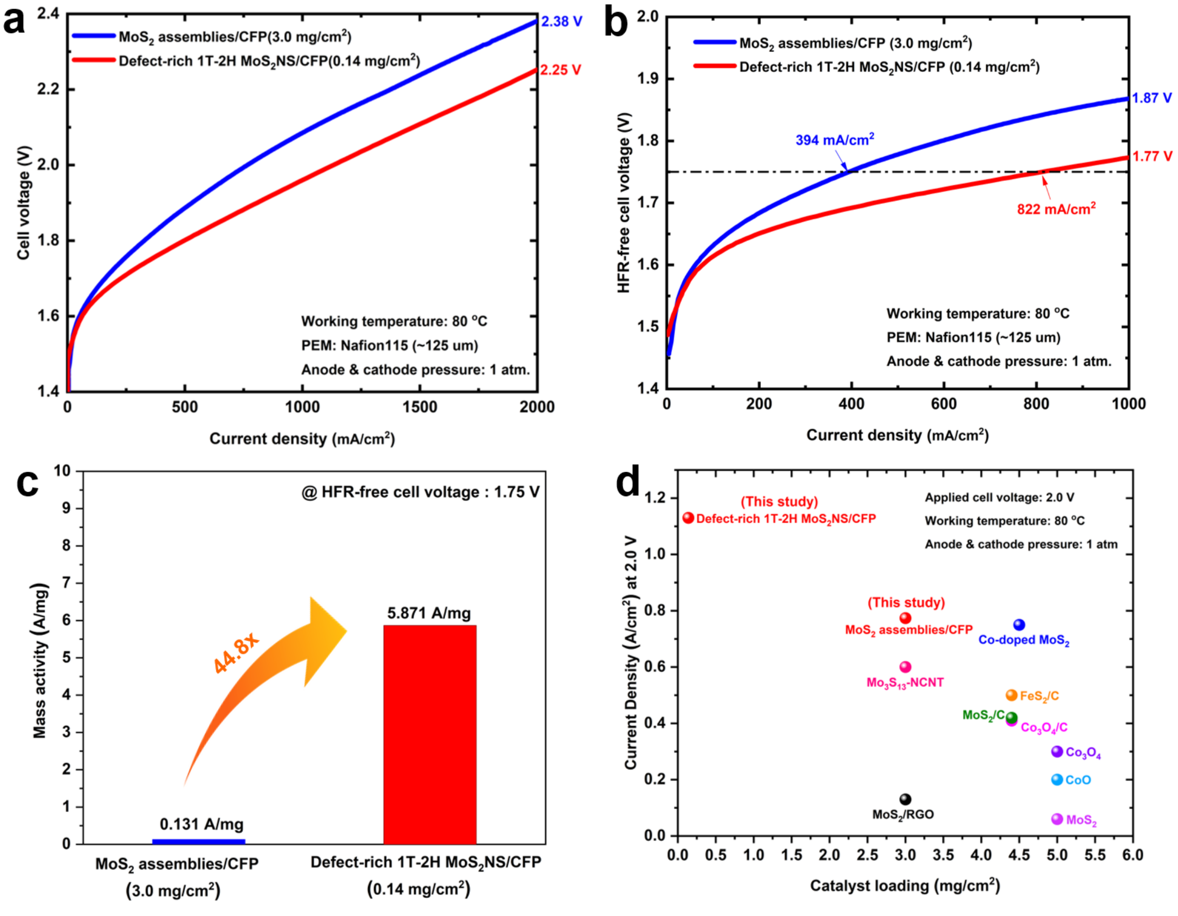

Figure 2.10 (a) Polarization curves of defect-rich 1T-2H MoS_2NS/CFP and MoS_2 assemblies/CFP in a PEMEC at 80 °C. (b) HFR-free polarization curves. (c) Mass activity comparison at the HFR-free cell voltage of 1.75 V. (d) Comparison of achievable current densities under the same applied cell voltage of 2.0 V and working temperature of 80 °C between this study and previously reported non-precious cathode catalysts with different loadings in a PEMEC. Reproduced with permission from Xie, Ma *et al.*[146]. 2022, Elsevier

Figure 2.10 (a) shows the *in situ* cell performance comparison of defect-rich 1T-2H MoS_2NS/CFP and MoS_2 assemblies/CFP in a PEMEC. By comparison, at 2000 mA/cm^2, defect-rich 1T-2H MoS_2NS/CFP with an ultralow loading of 0.14 mg/cm^2 demonstrates a much lower cell voltage of 2.25 V than that of MoS_2 assemblies/CFP (2.38 V). High frequency resistance (HFR) is another key parameter of the electrode that is usually used to represent the total ohmic resistance of the PEM electrolyzer cell. The HFR curves in **Figure 2.11**, the average of HFR value of defect-rich 1T-2H MoS_2NS/CFP is about 187 mΩ·cm^2, which is smaller than that of MoS_2 assemblies/CFP (217 mΩ·cm^2), indicating the ohmic losses can be greatly reduced with defect-rich 1T-2H MoS_2NS/CFP electrode in a PEMEC. The HFR-free polarization curves in **Figure 2.10 (b)** further identify that the activation losses of defect-rich 1T-2H MoS_2NS/CFP electrode is significantly lower than MoS_2 assemblies/CFP, as evidenced by the cell voltage decrease of 100 mV at 1000 mA/cm^2. These results validate that the defect-rich 1T-2H MoS_2NS/CFP possesses greatly maximized TPB sites and improved electrical conductivity compared to conventional spray coated electrodes.

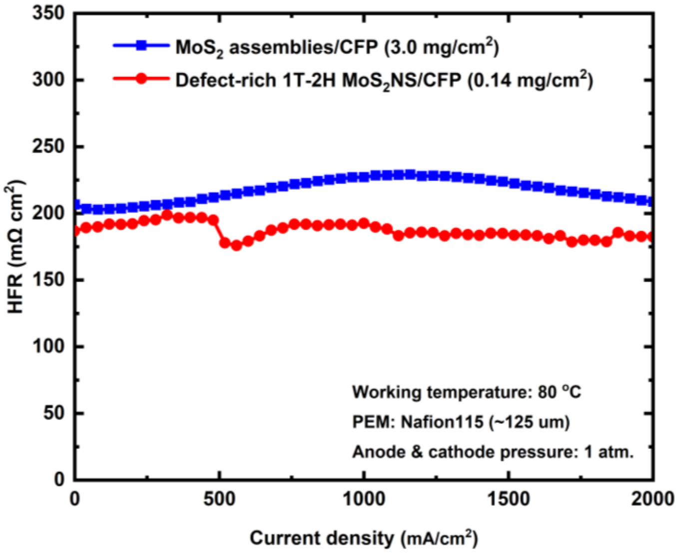

Figure 2.11 HFR curves of defect-rich 1T-2H MoS_2NS/CFP and MoS_2 assemblies/CFP electrodes. Reproduced with permission from Xie, Ma *et al.*[146]. 2022, Elsevier

By calculation of mass activities at HFR-free cell voltage of 1.75 V, it is found that the mass activity of defect-rich 1T-2H MoS_2NS/CFP is as high as 5.871 A/mg, which is over 44.8 times higher than that of a conventional spray coated electrode. **Figure 2.10 (d)** shows the comparison of achievable current densities under the same applied cell voltage of 2.0 V and working temperature of 80 °C between this study and previously reported PGM-free cathode catalysts with different catalyst loadings in PEMECs. It is clearly seen that our defect-rich 1T-2H MoS_2/CFP electrode can afford a significantly higher current density of 1.13 A/cm^2 at the applied cell voltage of 2.0 V than a lot of previous studies in the literatures[141-145]. More importantly, our study shows that about 20~40 times lower loadings of nonprecious catalysts compared to previous publications can be achieved by using defect-rich 1T-2H MoS_2NS/CFP integrated electrode.

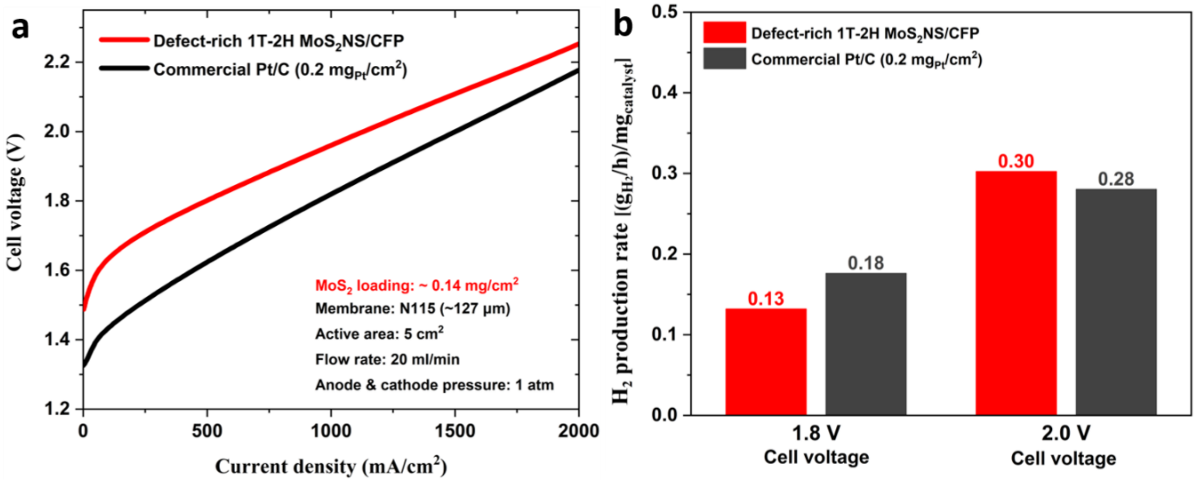

Figure 2.12 (a) Polarization curves of defect-rich 1T-2H MoS_2NS/CFP and commercial Pt/C in a PEMEC at 80 °C, (b) H_2 production rate comparison under the applied cell voltages of 1.8 V and 2.0 V, normalized to per mg of cathode catalysts. Reproduced with permission from Xie, Ma *et al.*[146]. 2022, Elsevier

For performance comparison with commercial cathode catalysts, we also tested the commercial Pt/C catalyst with a similar loading of 0.2 mg/cm^2 under the identical conditions. By comparison of polarization curves in **Figure 2.12 (a)**, a commercial Pt/C catalyst-based cathode shows a lower cell voltage of ~ 2.18 V than that of a defect-rich 1T-2H MoS_2NS/CFP cathode (2.25 V). The hydrogen production rates for both defect-rich 1T-2H MoS_2NS/CFP and Pt/C catalysts were calculated and compared in **Figure 2.12 (b)**. At the applied cell voltage of 1.8 V, H_2 production of 0.13 g/h per mg cathode catalyst can be achieved for defect-rich 1T-2H MoS_2NS/CFP, which is lower than that of Pt/C catalysts (0.18 g/h per mg cathode catalyst). However, at the higher applied cell voltage of 2.0 V, defect-rich 1T-2H MoS_2NS/CFP displays a H_2 production rate of 0.30 g/h, which is comparable to Pt/C catalysts (0.28 g/h per mg cathode catalyst). Considering the earth-abundance and much lower cost of MoS_2 materials than expensive PGM-based catalysts, the developed defect-rich 1T-2H MoS_2NS/CFP cathode in this work would hold great potential for large-scale water electrolyzer applications.

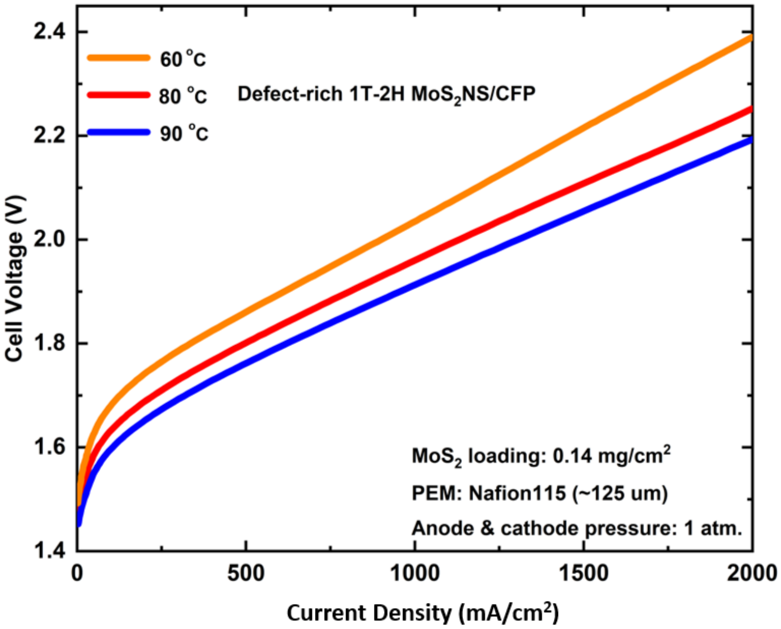

Figure 2.13 *in situ* cell performances of defect-rich 1T-2H MoS_2NS/CFP in a PEMEC under working temperatures of 60, 80 and 90 °C. Reproduced with permission from Xie, Ma *et al.*[146]. 2022, Elsevier

Figure 2.13 shows the *in situ* cell performance characterizations of defect-rich 1T-2H MoS_2/CFP as cathode in PEMECs tested under three typical working temperatures of 60, 80 and 90 °C. As a result, with an ultralow MoS_2 loading of 0.14 mg/cm^2, the obtained integrated electrode can afford high current densities of 1 A/cm^2 under 60, 80, and 90 °C by applying low cell voltages of 2.04, 1.96 and 1.91 V, respectively. Even at a higher current density of 2 A/cm^2, the applied cell voltages are only about 2.39, 2.25 and 2.19 V, respectively. These results demonstrate that defect-rich 1T-2H MoS_2NS/CFP can be directly applied as an efficient integrated cathode in PEMECs under the temperature range of 60~90 °C.

2.3.5 Post-analysis of defect-rich 1T-2H MoS_2 after electrolyzer test

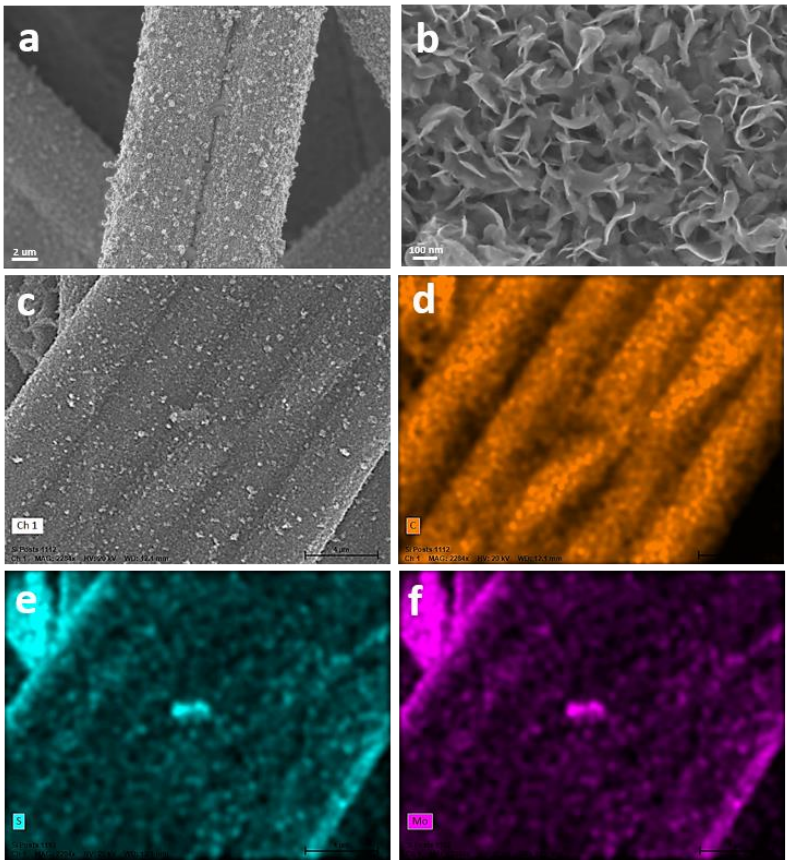

Figure 2.14 (a-c) Top-view SEM images of defect-rich 1T-2H MoS_2NS/CFP after the electrolyzer cell test, and SEM-EDX mapping images of (d) C, (e) S and (f) Mo, respectively. Reproduced with permission from Xie, Ma *et al.*[146]. 2022, Elsevier

Firstly, to unveil the morphological and structural changes of catalysts, the top-view and cross-sectional SEM and EDX as well as STEM characterizations of defect-rich 1T-2H MoS_2NS/CFP after the electrolyzer cell test is carried out. As seen from the top-view SEM images in **Figure 2.14 (a-c),** although MoS_2 nanosheets aggregate in some areas of the CFP substrate, the vertically aligned nanosheets are still maintained and fully cover the entire surface of the substrate. The SEM-EDX mapping images in **Figure 2.14 (d-f)** display a relatively uniform distribution of S and Mo elements on the CFP substrate, suggesting no significant detachment of the catalyst layer from the substrate. The cross-sectional SEM and EDX mapping images in **Figure 2.15** further verify the good coverage of MoS_2 nanosheets on the CFP substrate surface, demonstrating a good mechanical stability of the as-synthesized defect-rich 1T-2H MoS_2NS/CFP in a practical PEMEC. Moreover, the HAADF-STEM images in **Figure 2.16** confirm that MoS_2 nanosheet structures and defects of distorted edges, nanoscale pinholes and atomic vacancies still remain almost the same as the fresh sample before the electrolyzer cell test.

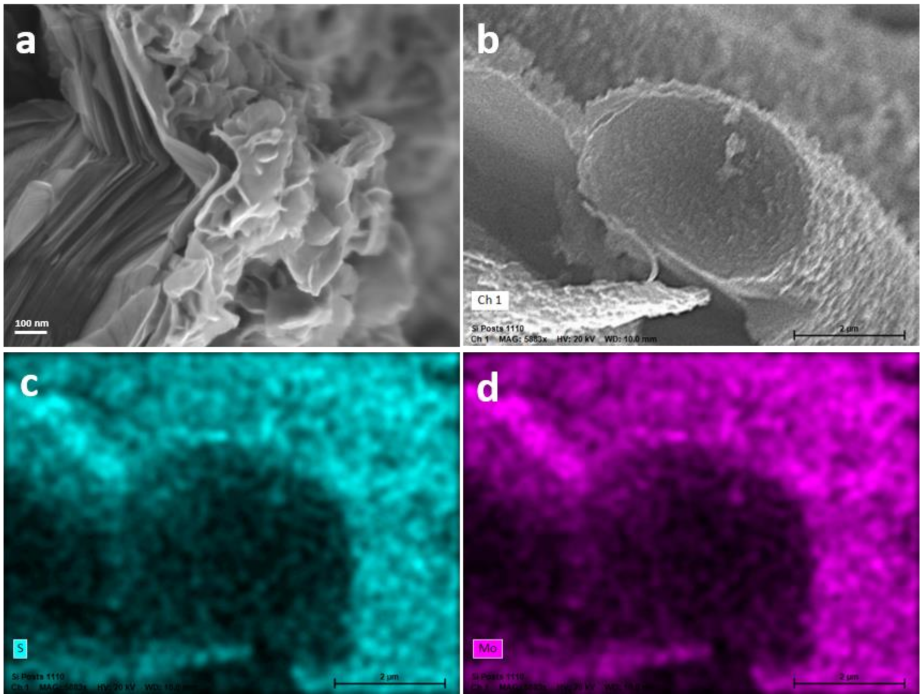

Figure 2.15 (a, b) Cross-sectional FE-SEM images of defect-rich 1T-2H MoS_2NS/CFP after the electrolyzer cell test, and SEM-EDX mapping images of (c) S and (d) Mo, respectively. Reproduced with permission from Xie, Ma *et al.*[146]. 2022, Elsevier

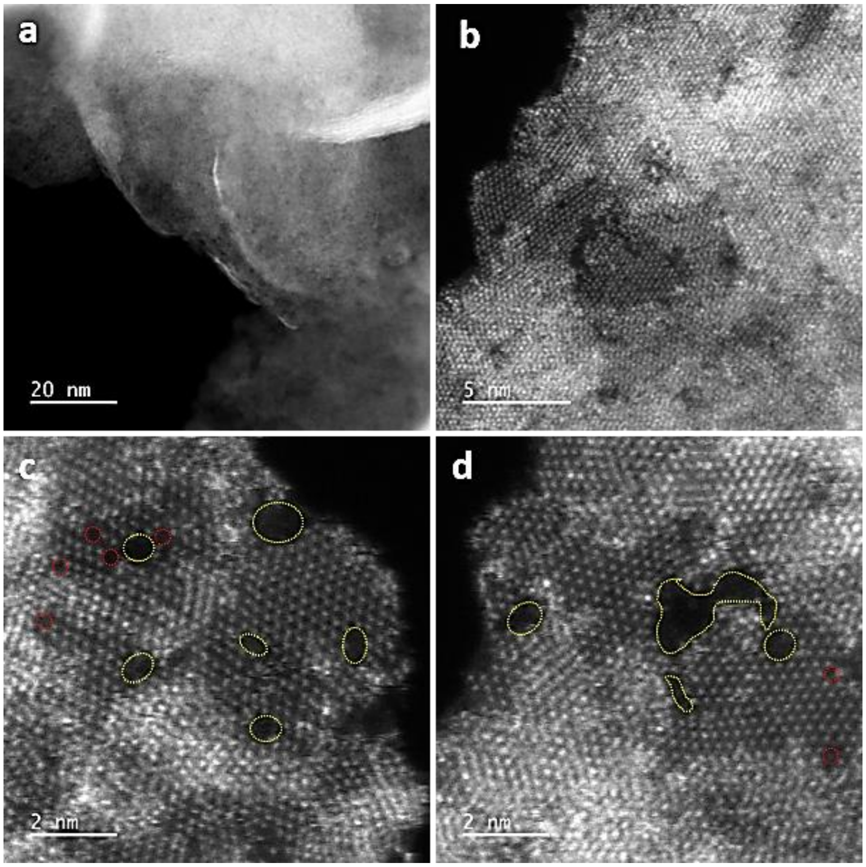

Figure 2.16 HAADF-STEM images of defect-rich 1T-2H MoS_2NS/CFP after the electrolyzer cell test. Reproduced with permission from Xie, Ma *et al.*[146]. 2022, Elsevier

Secondly, the phase composition change of catalysts was also analyzed by the Raman spectroscopy and XPS techniques. **Figure 2.8** exhibits similar Raman spectra of defect-rich 1T-2H MoS_2NS/CFP electrode before and after the electrolyzer cell test, which indicates the 1T and 2H MoS_2 phases are retained after the electrolyzer cell test. The analysis of high-resolution XPS spectra of Mo 3d + S 2s in **Figure 2.17 (a)** further reveal the slight decrease of 1T/2H phase ratio from 1.56 for the fresh sample to 1.33 for the tested sample. The partial 1T phase conversion into the 2H phase is probably attributed to the metastability of 1T phase at 80 °C in a practical PEMEC. [154-156] The high-resolution XPS spectra of S 2p in **Figure 2.17 (b)** show the same two doublets with the fresh sample in **Figure 2.7 (b)**, which are assigned to S-Mo and S-C bonding.

But it is found that the oxidized S content is increased from about 1.0 at.% for the fresh sample to about 4.0 at.% for the tested sample.

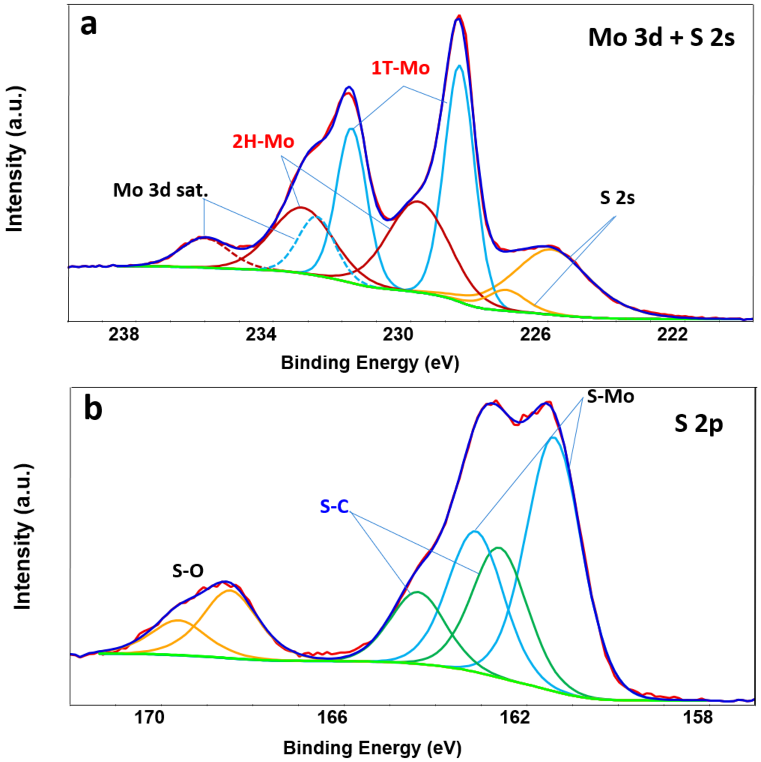

Figure 2.17 High-resolution XPS spectra of defect-rich 1T-2H MoS_2NS/CFP after the electrolyzer cell test. (a) Mo 3d + S 2s, (b) S 2p, respectively. Reproduced with permission from Xie, Ma *et al.*[146]. 2022, Elsevier

2.4 Conclusions

In this chapter, a one-step facile approach to *in situ* vertically growing MoS_2 nanosheets on the conductive CFP support is reported. This synthesis method can yield a unique type of MoS_2 nanosheets that possess various kinds of defects and 1T-2H hetero-phase simultaneously, which has not been reported previously. The Raman and XPS characterizations verify the coexistence of 1T and 2H phases in the MoS_2 nanosheets and the 1T phase was dominant. The HAADF-STEM images further elucidate the rich defects of atomic vacancies, nanoscale pinholes and distorted edges were formed within ultrathin MoS_2 nanosheets. Impressively, this integrated electrode with an ultralow MoS_2 loading of 0.14 mg/cm^2 can achieve small cell voltages of 1.96 and 2.25 V under 1 and 2 A/cm^2, respectively, in a practical PEMEC, superior to almost all cell performances of noble-metal-free HER electrocatalysts even with extremely high loadings of 3 ~ 6 mg/cm^2 under the similar cell operation conditions. The defect and multiphase features are thought to contribute to the outstanding electrocatalytic HER activity of the as-synthesized MoS_2 nanosheets. Additionally, the strong interaction generated by the intimate contact between conductive CFP support and the *in situ* grown MoS_2 nanosheets is also believed to be beneficial to the activity. Therefore, this work clearly reveals the positive impact of defects, multiphase and strong interaction between different parts of the electrode material on the HER performance of the electrode, which gives us valuable hints when designing the high-performance HER catalysts.

CHAPTER THREE

ENHANCING THE PHOTOCATALYTIC HYDROGEN EVOLUTION ACTIVITY OF 2D MoS_2 NANOSHEETS USING PLASMONIC Au NANOCAGES AS COCATALYST

3.1 Introduction

In the previous chapter, 2D multiphasic MoS_2 nanosheets have demonstrated the potential in electrocatalytic HER. Therefore, MoS_2 will continue to be used in this chapter as a catalyst for HER, however, in the more challenging photocatalysis pathway (as indicated in the research design map, **Figure 1.8**). But as stated in Chapter 1, 2D MoS_2 nanosheets were scarcely used as main photocatalyst due to its strong exciton binding energy. Therefore, a modification method is also necessary here for this research. As described in Chapter 1, apart from a spectrum of surface modifications, the construction of heterojunction is another commonly used strategy in photocatalysis.

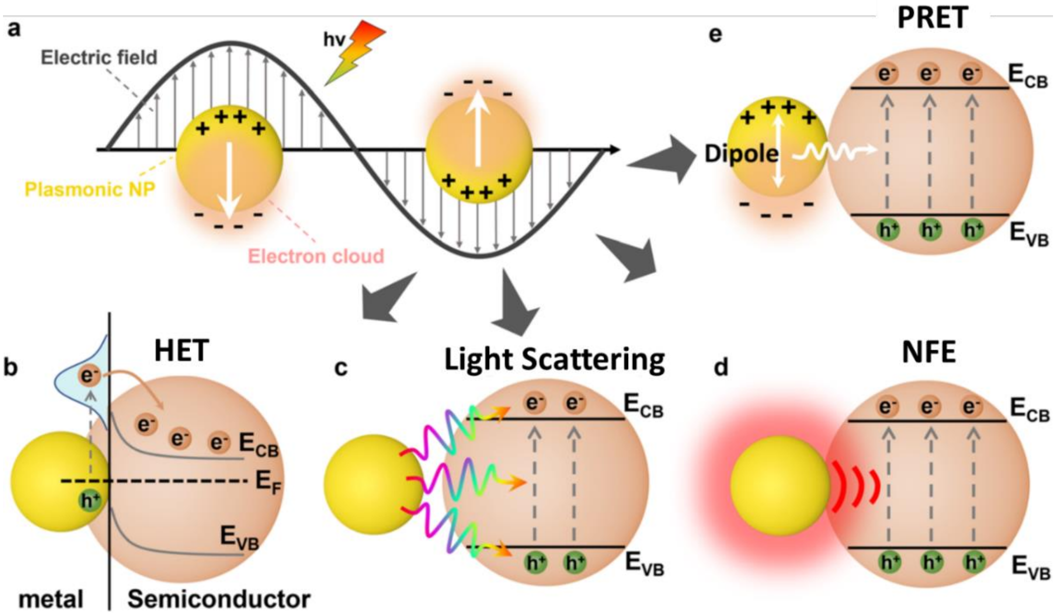

Figure 3.1 (a) Schematic illustration of LSPR and the four different working mechanisms of LSPR-enhanced photocatalysis: (b) HET, (c) light scattering, (d) NFE and (e) PRET. Reproduced with permission from Ye *et al.*[157] 2023, Royal Society of Chemistry

According to Chapter 1, a special family of metals with plasmonic effect have recently been studied widely as effective materials to boost the overall activity in semiconductor-based photocatalysis by forming the heterojunction structure, especially for photocatalytic HER[158-162]. The free electrons of these plasmonic metals can be driven by the electric field of the incident light to produce a collective oscillation if the light wavelength matches the intrinsic frequency of the metal material[157, 163]. This phenomenon is called surface plasmon resonance (SPR). When the SPR is activated on metal nanoparticles, it is usually referred as localized SPR (LSPR)[163]. Therefore, by combining plasmonic metal species with MoS_2, the LSPR effect can significantly enhance the light absorption of MoS_2 nanosheets, producing more photo-generated electrons in the material system. The LSPR process is schematically shown in **Figure 3.1 (a)**. The working mechanisms of LSPR-enhanced photocatalysis are quite complicated due to several possible concurrent ones. As illustrated in **Figure 3.1 (b-e)**, these processes basically include hot-electron transfer (HET), light scattering, near-field enhancement (NFE) and plasmon resonant energy transfer (PRET) [157, 161, 162, 164-166].

For HET [**Figure 3.1 (b)**], disequilibrium arrangement of the electrons in the metal nanostructure and surface "hot electrons" can be generated by LSPR. As the metal species are coupled with a semiconductor, the LSPR-induced hot electrons can be injected into the conduction band of the semiconductor that is in contact with the metal, which is a nonradiative process[161, 162, 164-166].

The light scattering process [**Figure 3.1 (c)**] occurs when the excited plasmon decay by releasing photons. The emitted photons will then be absorbed by the nearby semiconductors. In this case, the plasmonic metal nanoparticles act as the "mirrors" to increase the probability of the semiconductors to absorb the incident photons[167]. However, among the four processes, the contribution from light scattering is usually the weakest[157, 168] and hence not discussed in this chapter.

NFE [**Figure 3.1 (d)**], however, is a radiative process. The near electromagnetic field generated by the plasmon dipole on metal surface can significantly enhance the inter-band or other optical transitions in the nearby semiconductor (not necessarily in contact) as the generated field is typically orders of magnitude higher than the incident light[165, 166, 169]. Therefore, the plasmonic metal is acting like a secondary light source and transferring the energy to the semiconductor. One feature for the radiative process is that the emitted photon will possess the same energy as the absorbed photon[169]. Therefore, NFE requires the match of LSPR wavelength to the absorption edge of the semiconductor to maximize the process efficiency.

For PRET [**Figure 3.1 (e)**], the energy can be transferred from plasmonic metal species to semiconductors to generate excited electrons through nonradiative dipole-dipole coupling between plasmonic dipole and electron-hole exciton in semiconductors[165, 166]. Like NFE, no direct contact of the metal and semiconductor is required for PRET, but the energy transfer efficiency highly depends on the spectrum overlap between plasmonic metal and semiconductor and the special distance between the two parts[162, 165, 166, 169]. Additionally, it has a reverse and competing process called Förster resonant energy transfer (FRET), where energy will transfer from semiconductor to plasmonic metal. It becomes stronger when the spatial separation between metal and semiconductor becomes larger[170].

Besides, as metal materials, plasmonic metal species can also accept photogenerated electrons from the semiconductor through a classic electron transfer pathway, which makes the process even more complex. But considering that in the previous chapter, the strong interactions between different parts of the catalyst system has been proved critical to the overall performance, the interaction mechanism between the plasmonic metal species and MoS_2 hence becomes a key point in this research. This drives us to design a MoS_2-based plasmonic photocatalyst system that has tunable properties as a platform to understand the interaction between metal species and MoS_2 nanosheets.

As a famous plasmonic metal, various plasmonic Au nanostructures, such as Au nanorods[171-174], nanoplates[174, 175], nanocubes[174, 176], nanoantenna[175, 177], and nanoparticles[160, 178-180] have been reported to couple with MoS_2 nanosheets to investigate the plasmonic effect on the electronic and/or optical behaviors of the MoS_2. While the shape effect of Au nanostructures on LSPR behaviors has become a hot topic, the LSPR wavelength, another pivotal parameter of plasmonic metal nanostructures, has received less attention. So far, only limited work has been done to reveal how the variation of their various LSPR absorption behaviors impact the activity of photocatalyst system[181-184]. For example, it has been proposed that PRET may compete with HET when LSPR wavelength is close to the adsorption edge of semiconductor in the Ag@Cu_2O core-shell system and hence suppress the plasmonic enhancement[183]. Yue *et al.* [184] reported a Au-Ag/CdS catalyst system, which was composed by CdS as the semiconductor and Au-Ag nanoparticles (NPs) as the plasmonic nanostructure. The Au-Ag NPs were prepared by galvanic replacement. By adjusting the synthesis parameters, the LSPR wavelength of Au-Ag NPs can be finely tuned to a desired frequency. With the help of this feature, they found that excess absorption spectral overlap between the plasmonic metal and semiconductor can lead to a decrease in activity[184]. However, a comprehensive understanding of the system was still lacking as they only considered the PRET process of LSPR.

In the light of the merits of Au plasmonic materials and the insufficient understanding of the interaction between Au and semiconductors, we herein design a series of photocatalysts composed of 2D MoS_2 nanosheets loaded with Au nanocages with varying LSPR wavelengths. Firstly reported by Xia's group in 2007[185], Au nanocages are in nature Au shells on the surface of Ag nanocubes. They are similar to the Au-Ag NPs mentioned above as both of them are Au/Ag heterostructures prepared by galvanic replacement and their LSPR wavelength can be finely tuned, which offers a good opportunity to study the effect of LSPR wavelength of plasmonic species on MoS_2 nanosheets. Furthermore, considering the shape effect, Au nanocages can impose a stronger LSPR effect than the sphere-like Au-Ag NPs as Au nanocages have sharper features[169, 186]. The stronger LSPR effect around their edges and corners[169] can lead to a greater impact on photocatalytic performance, making it easier to be observed and analyzed.

Therefore, in this chapter, by tuning the LSPR wavelength of Au nanocages, we are able to investigate the impact of LSPR adsorption behavior of Au nanocages on the performance of the photocatalyst system in a comprehensive way. The underlying interaction mechanism between Au nanocages and MoS_2 nanosheets is characterized by microscopy, optical and time-resolved transient absorption spectroscopy of the Au nanocages and MoS_2 nanosheets. The knowledge learned from this research can provide insights into the design of high-performance photocatalysts for HER based on coupling of plasmonic materials and 2D semiconductors.

3.2 Experimental

3.2.1 Photocatalyst synthesis

Synthesis of Chemically Exfoliated MoS_2. The synthesis of the exfoliated, multiphasic MoS_2 nanosheets followed the previous report[153]. Briefly, bulk MoS_2 sample (ultrafine powder obtained from Graphene Supermarket) was dried in a vacuum oven at room temperature for 2 days to remove the adsorbed water molecules on the surface. Afterward, the dried MoS_2 sample was transferred to an Argon-filled glovebox. Then bulk MoS_2 was added to a Li superhydride solution [1.0 M in tetrahydrofuran (THF), Sigma Aldrich] with the concentration of 10 mg/mL. The mixed solution was sealed in an air-tight round bottom flask. After that, the round-bottomed flask was discharged from the glove box and put in a sonication bath at room temperature. The mixed solution was sonicated for 2 h to allow thorough diffusion of the Li sources into the layers of pristine MoS_2. Subsequently, the round-bottomed flask was placed into an oil bath and heated at 100 °C for 5 days. The sample was then washed with THF (≥ 99.0%, Sigma Aldrich) four times at room temperature to remove excessive Li precursor and organic residuals from the sample. Finally, the Li_xMoS_2 sample was dried under Argon atmosphere at room temperature. In order to obtain the exfoliated ultrathin MoS_2 nanosheets, the freshly prepared Li_xMoS_2 sample was dispersed in de-ionized (D.I.) water (18.2 MΩ/cm). Upon the addition of Li_xMoS_2 to D.I. water, continuous bubbles can be observed, which is ascribed to the formation of hydrogen gas. The mixture was then subjected to an additional 1 h of sonication in an ice bath to maintain the temperature. After sonication, the mixed solution was centrifuged several times to remove the unexfoliated MoS_2 while simultaneously washing out excess Li residuals from the sample. The exfoliated MoS_2 was collected and stored at room temperature for further use.

Synthesis of Ag Nanocubes. Ag nanocubes with an edge length 45-50 nm were prepared using a previously reported protocol[187]. In brief, 50 mL of ethylene glycol (EG) was preheated at 150 °C for 30 min. During this time, four separate solutions were prepared: (1) 2.0 mg NaSH in 11.89 mL EG (sample concentration: 3 mM), (2) 3 µL HCl in 12 mL EG (sample concentration: 3 mM), (3) 0.3500 g polyvinylpyrrolidone (PVP) (MW ≈ 55,000) in 17.5 mL EG, and (4) 0.3000 g CF_3COOAg (>99.99% metal basis, Aldrich) were dissolved in 4.18 mL EG (sample concentration 282 mM). Each of these solutions was sufficiently stirred to dissolve the precursors. Next, 0.6 mL of (1) was added to the EG solution at 150 °C. After 4 minutes, 5 mL of (2) was added to the reaction. After another 2 minutes, 12.5 mL of (3) was added to the reaction. After another 2 minutes, 4 mL of (4) was added to the reaction. The reaction was cooled in an ice bath after ~ 60 min. The Ag nanocubes were purified by dispersing the products of the reaction in acetone and collecting by centrifugation at 4,900 rpm for 8 min. The Ag nanocubes were washed three times in D.I. H_2O (18.2 MΩ/cm), collected by centrifugation at 14,000 rpm for 15 min, and combined in 8 mL of D.I. H_2O to create a stock solution of Ag nanocubes.

Synthesis of Au Nanocages. Au nanocages were prepared by galvanic replacement with $HAuCl_4$.[188, 189] Briefly, 1.000 mL of the stock solution of Ag nanocube solution was added to 20 mL of D.I. H_2O (18.2 MΩ/cm) and preheated for 20 min at 90 °C. A syringe (BD plastic, 30 mL) was filled with a freshly prepared stock solution of $HAuCl_4$ (0.75 mM, 20 mL), which was injected into the Ag nanocube solution at a rate of 4.5 mL/h. The reaction was monitored by UV-vis spectroscopy, and once the desired localized surface plasmon resonance was reached (460, 680, and 750 nm), the reaction was cooled in an ice water bath, stirred for 1 h with excess NaCl to form $AgCl_4^{3-}$, and centrifuged at 10,000 rpm for 20 min. The pellet containing Au nanocages was washed five times by re-dispersing in 25 mL D.I. H_2O and centrifuging at 10,500 rpm. The as prepared Au nanocages were labeled as Au-460, Au-680 and Au-750 regarding their respective LSPR wavelength.

Assembly of Au/MoS_2-Al_2O_3 Photocatalysts. The photocatalysts for solar hydrogen production were assembled by depositing Au nanocages and exfoliated MoS_2 nanosheets onto Al_2O_3 (Sigma Aldrich, surface area: 155 m^2/g) support materials. 0.6 g of Al_2O_3 were added into 5 mL of synthesized aqueous Au nanocages solution and sonicated for 2 h to achieve an intended 0.5 wt.% of Au. The sample was collected by centrifugation and dried at room temperature.

Subsequently, the dried powder sample was dispersed into 10 mL as-prepared MoS_2 solution to obtain 0.33 wt.% MoS_2. The mixed solution was shaken vigorously for 2 h. At last, the final product was collected again by centrifuging and dried at room temperature. For the sake of conciseness, the samples were labeled as AMA-460, AMA-680, and AMA-750 in which the AMA stands for Au, MoS_2, Al_2O_3 and the number indicates the LSPR wavelength of the Au nanocages.

3.2.2 Characterizations

Powder X-ray diffraction (XRD) patterns of the AMA samples were recorded from PANalytical X'Pert Pro Powder Diffractometer equipped with a Ni-filtered Cu Kα radiation. Scanning electron microscopy (SEM) images of exfoliated MoS_2 nanosheets deposited on Si wafer were collected with a Zeiss Merlin SEM at 3.0 kV. The transmission electron microscopy (TEM) images of exfoliated MoS_2 nanosheets deposited on lacy carbon grid was performed on an aberration-corrected FEI Titan S 80-300 TEM/scanning transmission electron microscopy (STEM) operated at 300 kV with a Gatan charge coupled device (CCD) camera. The STEM- X-ray energy dispersive spectroscopy (STEM-EDS) was performed on an FEI Talos F200X equipped with an EDS detector (Bruker) operated at 200 kV. Elemental maps were collected with a STEM spot size of 6. Raman and photoluminescence spectra of the exfoliated MoS_2 aqueous sample was performed on Acton TriVista 555 spectrometer (Princeton Instruments) with laser excitation at 532 nm. Diffuse reflectance spectroscopy (DRS) analysis of the AMA samples was carried out by Cary 5000 UV-visible spectrophotometer equipped with a praying mantis diffuse reflectance accessory. XPS measurements were completed on each powder sample (MoS_2-Al_2O_3) with a Thermo Scientific K-Alpha spectrometer. All spectra were collected using an Al Kα microfused monochromatized source (1486.6 eV) with a step size of

0.1 eV over 50 scans. For all spectra, the spot size was 400 μm and the operating pressure was under 3.0×10^{-7} mbar.

Femtosecond transient absorption measurements of the Au/MoS_2 deposited on a glass slide were carried out on a home-built pump-probe spectrometer (PPS). A full description of the PPS can be found elsewhere.[190] Briefly, the PPS is based on a titanium sapphire (Ti:Sa) oscillator (Micra, Coherent) with its output seeded a Ti:Sa Coherent Legend amplifier (USP-HE) operating at 1 kHz repetition rate. The amplifier provides pulses centered at 800 nm, with ~45 fs duration and 2.2 mJ energy per pulse. The output of the Legend amplifier was divided into two portions: 90% was attenuated to 0.5 mJ and focused on a BBO crystal to generate 400 nm pump pulse. The second portion (10%) was used to generate the white light continuum (WLC) probe in a 2 mm thick sapphire window. The WLC, which covers the spectral range from 450 nm to 900 nm, was collimated after generation and focused onto the sample using high reflective parabolic mirrors to minimize temporal chirp. After that, the transmitted probe was focused onto a 100-micron core fiber coupled with a spectrometer linear CCD array (USB2000ES, Ocean Optics). The pump passes through a controllable stage-delay and was chopped at 500 Hz frequency to allow the measurement of absorbance change in the transmitted probe between each two successive laser shots. At the sample, the pump and probe spot sizes were 100 and 50 μm, and the pump energy was ~ 4 μJ/cm^2.

3.2.3 Photocatalytic hydrogen evolution reaction.

In a typical photocatalytic experiment, 40 mg of the photocatalyst was dispersed in a solution composed of 30 mL deionized water and 10 mL methanol (Alfa Aesar) as the scavenger in a quartz reactor. Prior to the photocatalytic reaction, the quartz cell was purged by continuous flushing with ultrahigh pure Argon gas for 30 min. The light input is provided by a 200 W Hg lamp equipped with a cut-off filter to allow the pass of visible light with wavelength longer than 400 nm. The suspension was stirred vigorously during the entire photocatalytic reaction and the temperature of the system was maintained at 25 °C by the cooling water circulating around the entire quartz cell. The yielded hydrogen gas was determined and quantified using gas chromatography (GC) compiled with hydrogen calibration plot, with model BUCK 910 (molecular sieve column, TCD detector, and Argon as carrier gas). The photocatalytic hydrogen production rate was calculated by normalizing the produced hydrogen to the amount of MoS_2 in the catalysts per hour.

3.3 Results and discussion

3.3.1 Structure and morphology

In order to investigate the crystallographic structures of the AMA samples, powder XRD was employed. **Figure 3.2 (a)** shows the XRD patterns of the composite AMA samples along with a pure Al_2O_3 support material. The XRD patterns of the Au and MoS_2 incorporated samples exhibit a similar pattern to that of Al_2O_3, *i.e.*, intrinsic diffraction peaks of Al_2O_3 can be observed from all the samples. A few small diffraction peaks falling at 18.1° can be assigned to the presence of $Al_2O_3{\cdot}3H_2O$ (PDF: 00-001-0259). No peak of Au or MoS_2 can be observed due to their low loading on Al_2O_3.

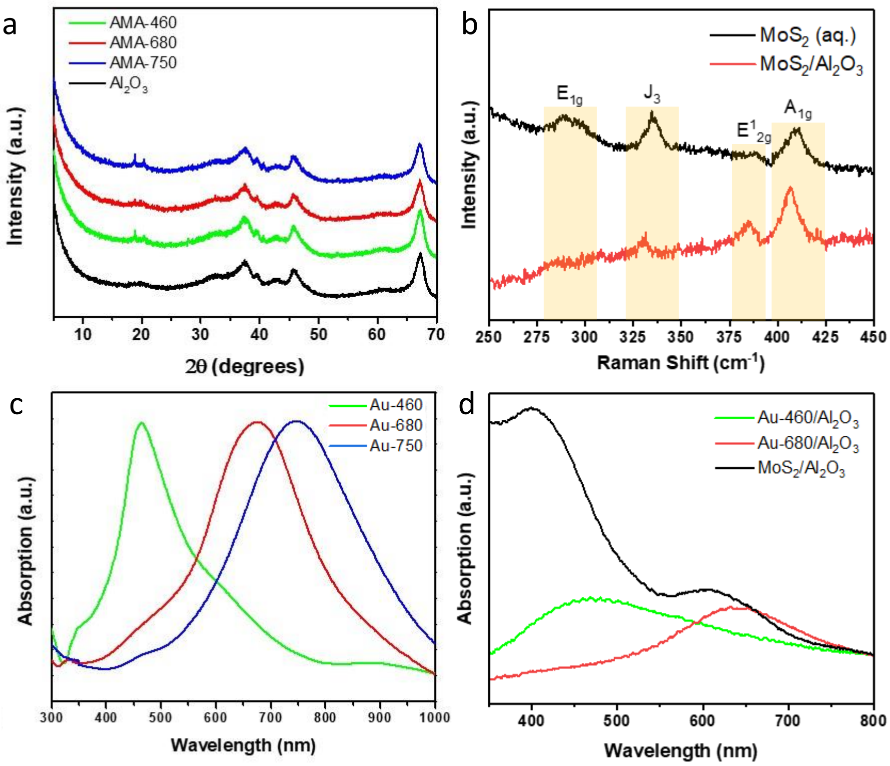

Figure 3.2 (a) XRD patterns of Al_2O_3 supported Au/MoS_2 samples. (b) Raman spectrum of the as-exfoliated MoS_2 nanosheets suspended in water (black) and loaded on Al_2O_3 (red). (c) UV-vis absorption spectra of as-synthesized three Au nanocages. (d) UV-vis DRS of Au-460, Au-680 and MoS_2 nanosheets loaded on Al_2O_3.

Similar to the previous work[153], Raman spectroscopy is applied to identify the 2D and multiphasic nature of the as-synthesized MoS_2 nanosheets. The Raman spectra of the freshly prepared MoS_2 aqueous suspension is shown in **Figure 3.2 (b)**. The typical in-plane mode (E^1_{2g}) and out-of-plane mode (A_{1g}) peaks of MoS_2 sample can be observed at 388 and 409 cm^{-1}. Compared with those (385 and 410 cm^{-1}) of the bulk MoS_2, the shift of the two peaks indicates the effective exfoliation of the Li intercalated MoS_2 layers and the presence of single-layer MoS_2[191]. In addition to the E^1_{2g} and A_{1g} vibration modes, the exfoliated MoS_2 nanosheets also present two unique peaks around 285 (E_{1g}) and 333 cm^{-1} (J_3), both of which originate from the metallic 1T-like phase of MoS_2 formed during the Li intercalation[153, 192]. The Raman spectrum of MoS_2/Al_2O_3 is also inspected to check if there is any structure change after the loading on Al_2O_3.

Although the E_{1g} peak becomes less obvious, the existence of J_3 still reveals the existence of 1T-like phase. Meanwhile, although there is a slight peak shift for E^1_{2g} (from 388 to 386 cm^{-1}) and A_{1g} (from 409 to 407 cm^{-1}), probably caused by the dielectric effect from Al_2O_3, the separation between these two peaks is almost unchanged after the loading process, suggesting that the MoS_2 nanosheets are well dispersed and do not restack on Al_2O_3.

The AFM image and the layer thickness profiles of three representative nanosheets displayed in **Figure 3.3 (a, b)** demonstrate that the majority of the MoS_2 nanosheets are about 1 nm thick. This also confirms the successful preparation of single-layer MoS_2. Combining the SEM image of these exfoliated nanosheets shown in **Figure 3.3 (c)** and from the previous work on the same MoS_2 system[153], it can be concluded that monolayered multiphasic MoS_2 nanosheets have been successfully obtained by following our preparation procedures.

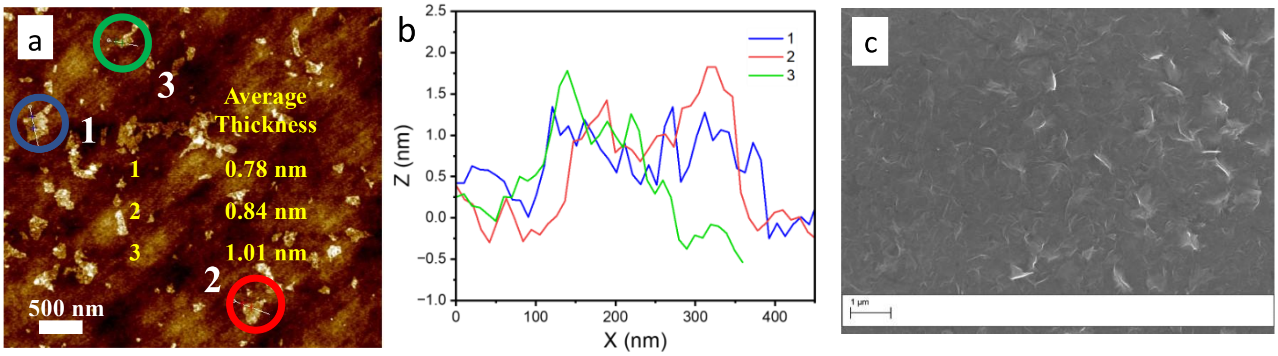

Figure 3.3 (a) AFM image of the as-exfoliated single-layer and (b) the hight profiles of three selected regions indicated in the figure. (c) SEM image of exfoliated MoS_2 sample.

The LSPR of the Au nanocages is verified before dispersing onto the Al_2O_3 support. The Au nanocages are prepared via galvanic replacement between Ag nanocubes and $HAuCl_4$ in an aqueous solution set to 90 °C, similar to the previous reports[188]. To systematically investigate the effect of the LSPR on the performance of photocatalytic activity over MoS_2 samples for photocatalytic HER, the LSPR of the Au nanocages was tuned to three different wavelengths:

460, 680, and 750 nm [**Figure 3.2 (c)**] that are off, on, and off the light absorption edge of MoS_2. **Figure 3.2 (d)** displays the UV-vis diffuse reflectance spectra (DRS) of the Au nanocages loaded on Al_2O_3. Only slight peak shift is observed that does not affect the relative position to each other. A good match of the absorption edge of MoS_2 and the LSPR wavelength of Au-680 can also be observed from the spectra. The as-synthesized Au nanocages have an average size of 48 ± 3.5 nm as measured by transmission electron microscopy (TEM) (**Figure 3.4**). When Au nanocages are titrated with different amounts of $HAuCl_4$, their wall thickness changes and pushes the LSPR towards the near-infrared spectral region.

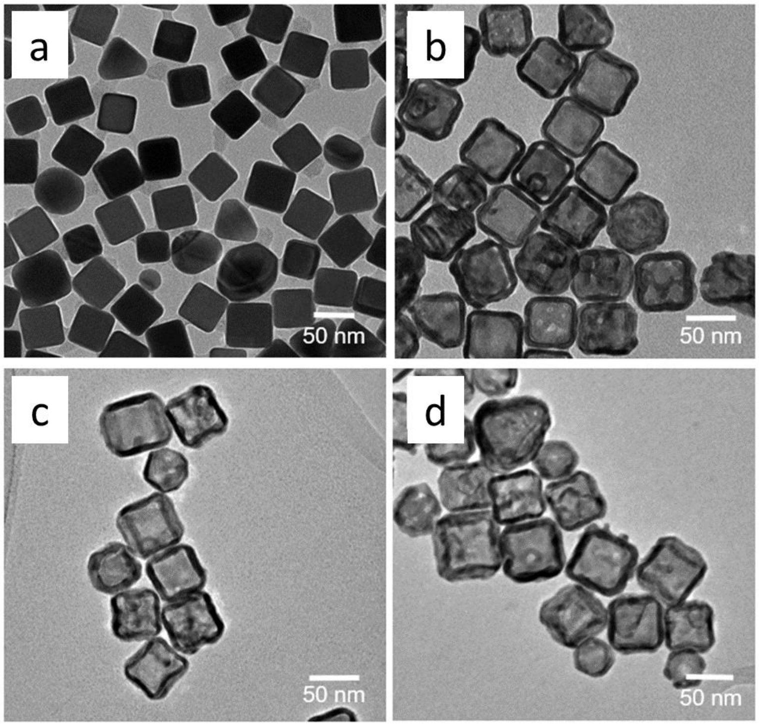

Figure 3.4 Representative TEM images of (a) Ag nanocubes and Au nanocages with LSPR wavelength at (b) 460 nm, (c) 680 nm, and (d) 750 nm.

To investigate the heterojunction between gold nanocages and MoS_2 nanosheets, we prepare a representative sample for high-angle annular dark-field (HAADF) scanning transmission electron microscopy (STEM) and bright-field STEM (BF-STEM) imaging. **Figure**

3.5 shows the BF- and HAADF-STEM images of the AMA-680 sample as a representative. The BF-STEM images clearly reveal the lattice for the gold nanocage and the honeycomb structure for MoS_2. We also investigated the elemental distribution of Au, Mo, S, Ag and Al of the AMA-680 sample by energy-dispersive X-ray spectroscopy (EDS) based on STEM. The STEM-EDS elemental mappings are shown in **Figure 3.6**, where Au nanocage is clearly seen in contact with MoS_2, as expected, on the Al_2O_3 support. However, it should be noticed that due to the tremendous morphology and size differences between the Au nanocages and MoS_2 nanosheets, some of the MoS_2 nanosheets are not in contact with Au, which can also be observed from **Figure 3.6**.

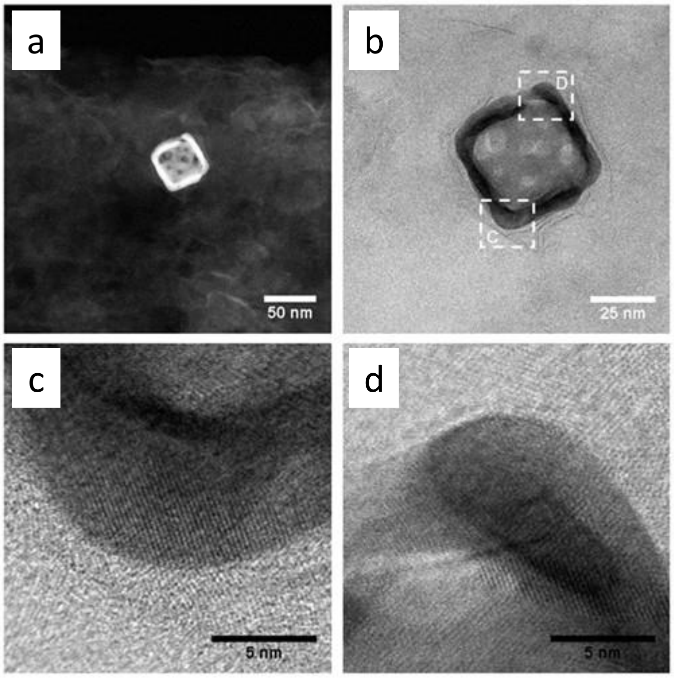

Figure 3.5 Representative (a) HAADF- and (b-d) BF-STEM images of AMA-680 sample

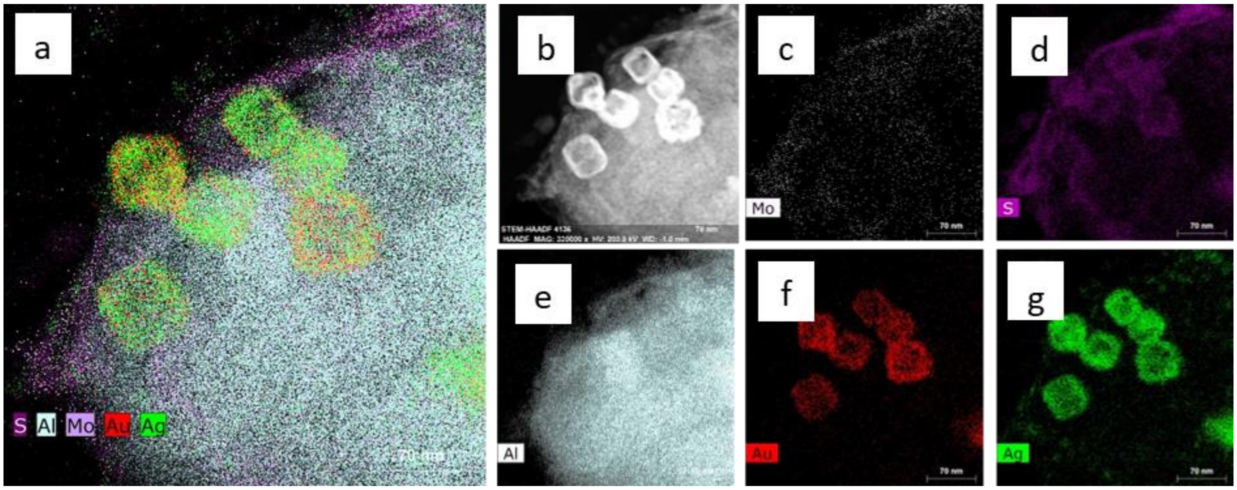

Figure 3.6 (a) STEM-EDS overall elemental map, (b) the corresponding STEM image and the individual mappings of (c) Mo (d) S (e) Al (f) Au and (g) Ag of AMA-680.

The phase properties of the chemically exfoliated MoS_2 are evaluated by X-ray photoelectron spectroscopy (XPS). It must be noted that the thermodynamically stable form of MoS_2 is the 2H phase, where each Mo is prismatically coordinated with six S atoms. The 1T-like phase, on the other hand, is composed of octahedrally coordinated Mo with six S atoms. The structure of MoS_2 has been previously reported to undergo a structural transformation from the 1T-like to 2H phase by thermal treatment between room temperature and 300 °C[153]. XPS is then employed to further investigate the multiphasic properties of the 2D MoS_2 in different AMA samples, as shown in **Figure 3.7**. The Mo 3d spectra [**Figure 3.7 (a)**] consist of peaks around 229 and 232 eV, corresponding to Mo^{4+} $3d_{5/2}$ and Mo^{4+} $3d_{3/2}$, respectively. Deconvolution of the Mo 3d spectra reveals a shift in the spectra to higher binding energies (by ~ 0.9 eV) when the MoS_2 nanosheets are annealed at increased temperatures (*e.g.,* 60 and 120 °C). This shift to higher binding energies can be attributed to the phase transformation from the metallic 1T-like to the 2H phase (**Table 3.1**). The S 2p spectra shown in **Figure 3.7 (b)** display a similar shift to higher binding energies when multiphasic MoS_2 is annealed at increased temperatures. The S 2p spectra display doublet peaks, S $2p_{1/2}$, and S $2p_{3/2}$, appearing at ~163 and ~161.9 eV, respectively. Deconvolution of these peaks clearly illustrates the phase shift from metallic 1T-like phase to the 2H phase when the samples are annealed at 60 and 120 °C. It is worth noting that no peaks are observed from 235 to 240 eV, suggesting that oxidation of Mo^{4+} to Mo^{6+} is minimal. The oxidation state and thermal stability of the Au nanocages are also investigated by XPS and TEM imaging after the thermal annealing at 60 and 120 °C. XPS measurements are also collected of the Au 4f region for the different gold nanocages. As shown in **Figure 3.7 (c)**, the Au 4f region shows clear doublet peaks at 84.0 and 87.7 eV, corresponding to Au^0 $4f_{5/2}$ and Au^0 $4f_{7/2}$, respectively. TEM images of the Au nanocages before and after heat treatment at 60 and 120 °C show that the gold nanocages retain their morphology (**Figure 3.8**).

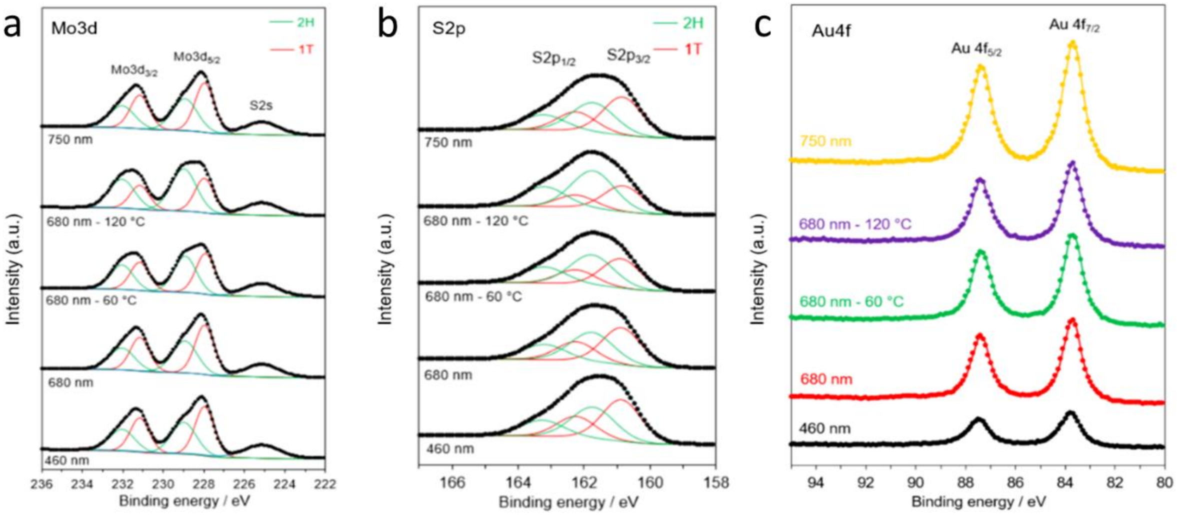

Figure 3.7 XPS spectra of (a) Mo 3d, (b) S 2p, and (c) Au 4f core level regions of the various AMA samples.

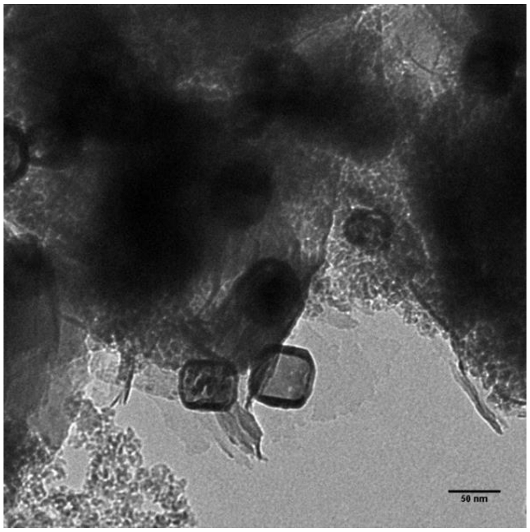

Figure 3.8 TEM image of the AMA-680-120 sample.

Table 3.1 Relative fraction of 1T and 2H phases in different samples from XPS analysis.

Sample	**Relative fraction**	
	1T	2H
460 nm	0.59	0.41
680 nm	0.60	0.40
680 nm - 60 °C	0.53	0.47
680 nm - 120°C	0.45	0.55
750 nm	0.60	0.40

UV-vis DRS is conducted to investigate the optical properties of the AMA samples. **Figure 3.9 (a)** displays the spectra of the AMA samples assembled with various Au nanocages. All the spectra in **Figure 3.9 (a)** are similar to each other, a result of the strong light absorption by MoS_2. Several absorption bands in the visible light region can be observed in these samples. Two strong absorption peaks that belonged to typical MoS_2 are observed in all the samples. The one at ~420 nm corresponds to convoluted C and D excitonic and the one at ~620 nm corresponds to A and B excitonic peaks arising from the K point of the Brillouin zone.[193] Due to the high intensity of these two peaks, the absorption of Au-460 and Au-680 is eclipsed. However, the Au-750 presents an appreciable while broad absorption band at ~750 nm that can be clearly monitored. We also perform the UV-vis DRS on the annealed AMA-680 samples and their spectra are shown in **Figure 3.9 (b)**. It can be seen that all the samples display similar absorption curves indicating the similar chemical composition of the samples after heat treatment.

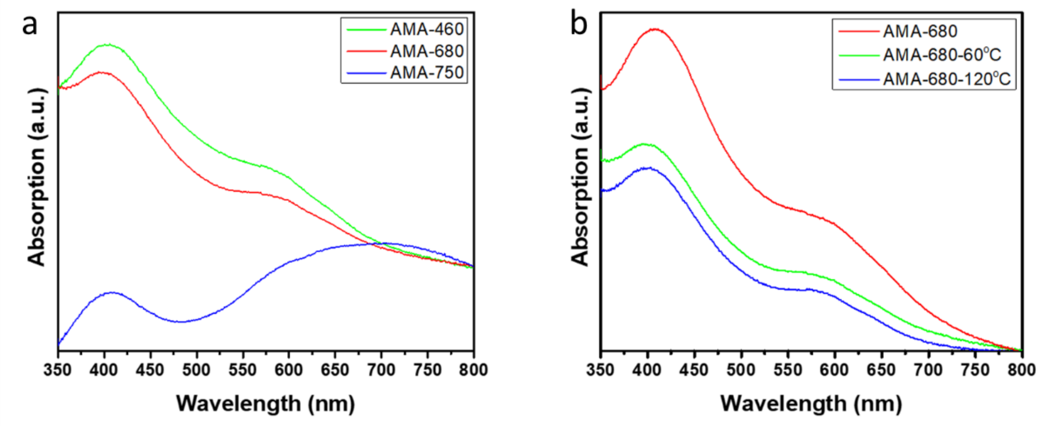

Figure 3.9 UV-vis DRS of (a) AMA samples with various Au nanocages and (b) AMA 680 samples treated at various temperatures.

3.3.2 Photocatalytic performance

In order to investigate the LSPR effect on the photocatalytic HER performance, the activity of the AMA samples is studied under identical experimental conditions. **Figure 3.10** shows the kinetic plot of the AMA samples in terms of the hydrogen evolution rate normalized to MoS_2 weight as a function of reaction time. It can be seen that compared with the pure MoS_2 sample, all Au-containing samples exhibit over an order of magnitude enhancement on the hydrogen evolution rate. This phenomenon is thought to be the result of the LSPR effect from Au nanocages. These surface plasma aroused from Au nanocages have been proven as beneficial factors during the photocatalytic hydrogen evolution reaction.[194, 195] Interestingly, it can be seen that the AMA-680 sample presents strikingly higher photocatalytic hydrogen evolution rate compared with the other two AMA samples. As shown in **Figure 3.10 (a)** and **(c)**, a ~40-fold increase in the hydrogen evolution rate is obtained on the AMA-680 over the bare MoS_2 nanosheets while about a 15-fold increase is found on the other two AMA samples. The superior photocatalytic activity in the AMA-680 sample may be rationalized by the more efficient energy and/or electron transfer between the Au-680 nanocages and the MoS_2 nanosheets. A more detailed discussion will be presented in the following part of this chapter regarding the mechanism. **Figure 3.10 (d)** showed the cyclic stability of AMA-680 in photocatalytic HER, above 90% of the activity can be retained after 5 cycles. This indicates the Au-MoS_2 composite is highly stable under the testing conditions.

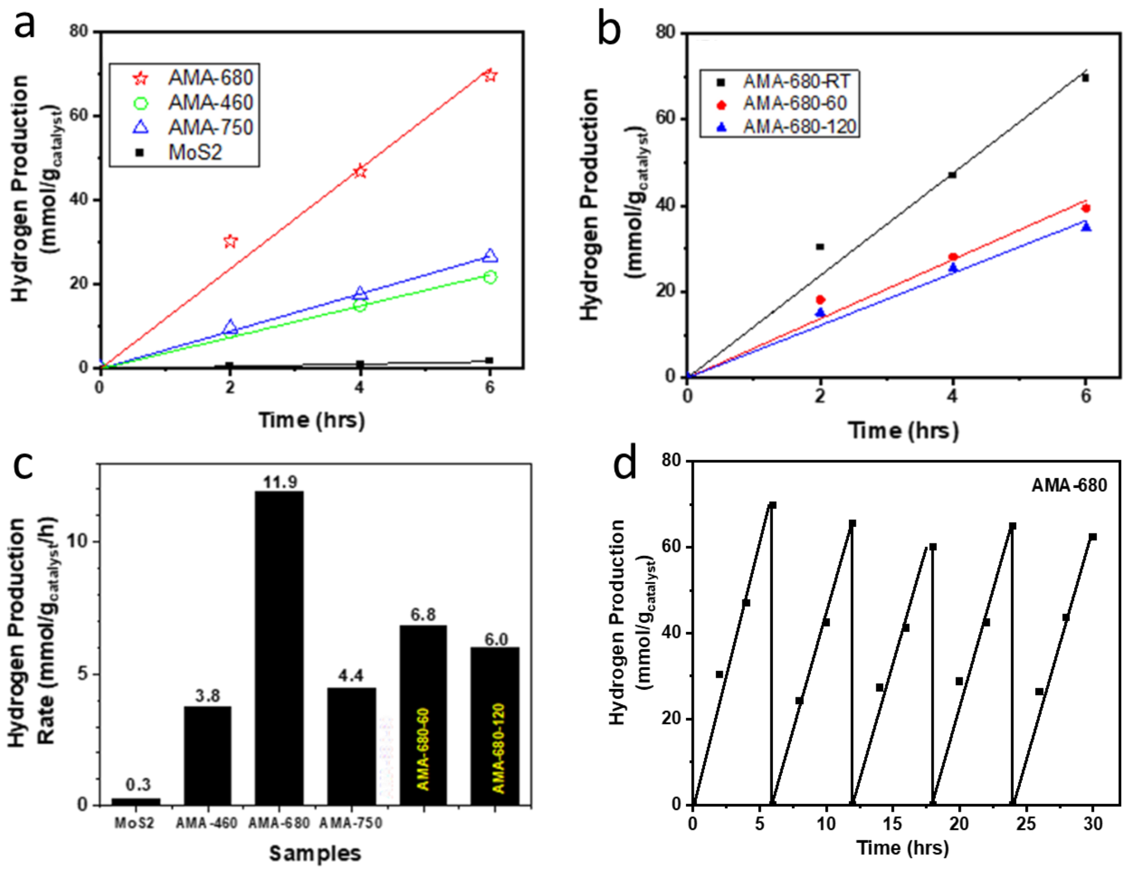

Figure 3.10 Photocatalytic hydrogen evolution as a function of time over (a) AMA samples with Au nanocages with varying LSPR and (b) AMA-680 samples treated at various temperatures. (c) Comparison of the photocatalytic hydrogen production rate over different samples. (d) Cyclic stability test result of AMA-680 in photocatalytic hydrogen evolution.

To reveal the role played by the multiphases feature of MoS_2 in this reaction, AMA-680 IS heated to 60 and 120 °C to vary the ratio of the 1T-like and 2H phases and tested for HER performance. As shown in **Figure 3.10 (b)**, the heat treatment, which leads to decreased proportion of 1T-like phase as shown in **Table 3.1**, results in a decrease in HER rate from 11.9 to 6.8 and 6.0 mmol $H_2/g_{catalyst}$ /h for AMA-680-60 and -120, respectively [**Figure 3.10 (c)**]. The observation suggests an important role of 1T-like phase in the HER, consistent with the previous result[153]. It is previously shown that the photogenerated electrons from the 2H phase of MoS_2 had the tendency to diffuse to the 1T-like phase, where the protons were more likely to be reduced into hydrogen. The 1T-like metallic phase of MoS_2 is known as a good "electron sink" and exhibits superior electron affinity to the 2H phase MoS_2. Hence, the electrons generated, no matter the origin, are inclined to migrate to the 1T-like MoS_2 to conduct the HER. But the HER rate of AMA-680-60 and AMA-680-120 is still ~ 50% higher than that of the AMA-460 and AMA-750 samples, again pointing to the key role of the match between Au nanocage LSPR wavelength and MoS_2 absorption edge.

3.3.3 Mechanism discussion

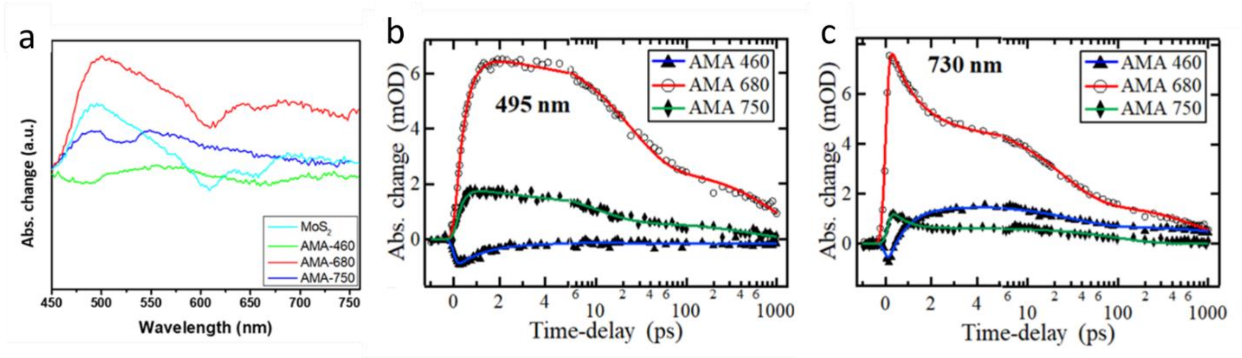

Figure 3.11 A) Transient absorption spectra of the AMA samples and bare MoS_2 (recorded 0.4 ps after excitation at 400 nm) and transient absorption dynamics for AMA samples monitored at B) 495 nm and C) 730 nm following pump excitation at 400 nm. Symbols are experimental data, and solid plots are fits. The time-delay axis is shown in linear scale up to 5 ps, and logarithmic scale thereafter.

In order to unveil the origin of the excited electrons, time-resolved transient absorption spectroscopy (TAS) is carried out to track the destiny of the electrons in the AMA system. In this work, 400 nm, 45 fs laser pulse is used as the pump to excite the electrons in AMA samples and the time-resolved differential transmission spectra were recorded to track the decay dynamic of the excited electrons. The transient absorption spectra recorded 0.4 ps after excitation are shown in **Figure 3.11 (a)**. They contain a broad feature with a positive sign (pointing up). Within this band, there are two depletion signals (pointing down) around 660 and 610 nm originating from excitons A and B of MoS_2, respectively[196, 197]. The broad positive band contains two peaks around 500 nm (strong) and 700 nm (weak). Considering that the UV-vis spectra of the three samples also showed strong absorption around these two wavelengths, we monitor the three samples at 495 and 730 nm up to 1 ns time-delay after the probe excitation and plotted their decay dynamics as functions of time in **Figure 3.11 (b)** and **(c)** in order to get better signals as well as facilely inspect the electron transfer mechanism under the excitation on and off the LSPR wavelength of Au nanocages. According to the previous reports[198, 199], excitons in 2D-TMDs decay through three distinct mechanisms: a fast process ascribed to thermalization takes place within the first picoseconds after excitation, followed by the relaxation during the next few picoseconds, and finally a much slower process that can take hundreds of picoseconds or longer assigned to defect-assisted recombination. Based on this, we fitted the dynamics shown in **Figure 3.11 (b)** and **(c)** to the following tri-exponential decay function:

$$A_1 e^{-\frac{t}{t_1}} + A_2 e^{-\frac{t}{t_2}} + A_3 e^{-\frac{t}{t_3}}$$

t_1, t_2, and t_3 (ps) are the time-constants assigned to thermalization, relaxation and defect-assisted recombination processes, respectively, and A_1, A_2 and A_3 (milli optical density, mOD) are their corresponding amplitudes. All the three time constants can be affected if there is any electron/energy transfer taking place at the MoS_2/Au nanocage interface. However, in this material system, only t_1 is the direct indicator of LSPR effect since the plasmonic energy and/or hot electrons are mostly available during the first few hundreds of femtoseconds after the excitation, which is within the scope of t_1. As t_2 and t_3 represent slower processes, they are good indicators of the classic electrons transfer from MoS_2 to Au nanocages as this process is not efficient enough to affect t_1. The fitted time constants and amplitudes are listed in **Table 3.2** and **Table 3.3**.

Table 3.2 Fitted results of three times constants (ps) of the AMA samples monitored at 495 and 730 nm.

Time constant	Au-680	MoS2	AMA-460	AMA-680	AMA-750
t_1-495	2.21	0.43	0.88	0.48	0.33
t_1-730	5.36	0.17	0.89	1.40	0.18
t_2-495	3.48	18.58	30.53	22.85	9.70
t_2-730	5.37	8.17	30.23	26.40	0.51
t_3-495	7044	1011	2940	1010	516
t_3-730	2267	788	2915	960	99

Table 3.3 Fitted results of three amplitudes (mOD) of the AMA samples monitored at 495 and 730 nm.

Amplitude	Au-680	MoS_2	AMA-460	AMA-680	AMA-750
A_1-495	8.3	-4.2	-2.6	-6.8	-1.9
A_1-730	-12.9	-1.9	-2.6	3.3	-2.1
A_2-495	-13.1	2.9	0.9	4.3	1.3
A_2-730	8.1	1.6	0.9	3.2	1.7
A_3-495	0.9	1.3	0.7	2.6	0.6
A_3-730	0.9	0.3	0.7	1.6	0.6

By comparing the fitted time constants of the three AMA samples with bare MoS_2 nanosheets (shown in **Table 3.2**), it is found that they demonstrate three distinct behaviors.

For AMA-460, all the three time constants are seemingly not affected by LSPR, which suggests that the classic electron transfer from MoS_2 to Au nanocages is the dominant process in this system and the effect of LSPR is negligible, as shown in **Figure 3.12 (a)**. This system is a classic photocatalyst system, where MoS_2 is the semiconductor and Au-460 works as cocatalyst.

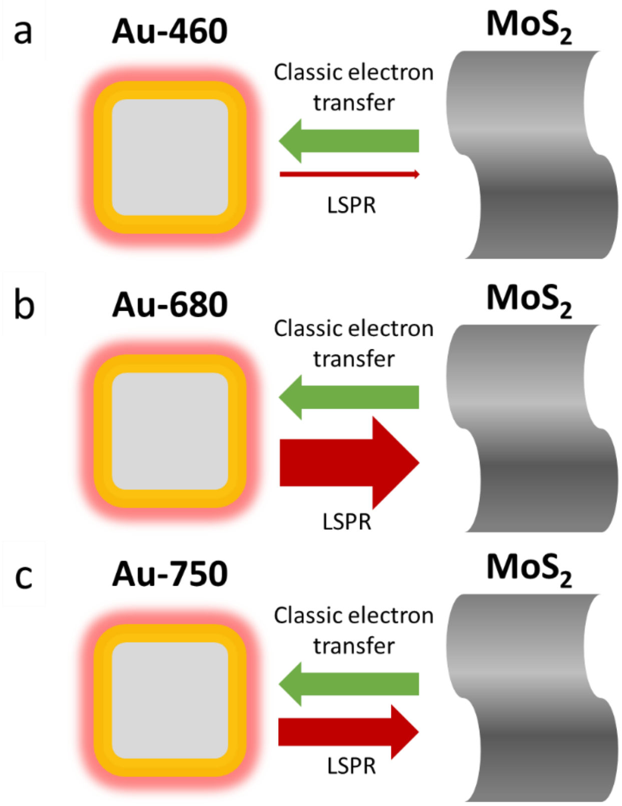

Figure 3.12 Schematic illustration of the electron transfer process in (a) AMA-460, (b) AMA-680 and (c) AMA-750.

For AMA-750, however, it is a much more complicated situation. Its decay dynamics is sensitive to the monitoring wavelength and starts to take the shape of bare MoS_2. This highly implies that the LSPR effect in this system becomes strong enough to nullify the contribution from the classic electron transfer. When monitoring at 730 nm, where LSPR is strong for Au-750, the t_1 of AMA-750 is slightly longer than MoS_2 while t_2 and t_3 are greatly shortened. Considering their above-mentioned indications, this clue suggests that the LSPR wins the competition, but just marginally. However, it completely changes the electron migration direction. Therefore, the whole system is then converted to a plasmonic photocatalyst system, as shown in **Figure 3.12 (c)**. The strong LSPR effect under 730 nm intensively prohibited the classic electron transfer.

For AMA-680, its decay dynamics was also dependent on monitoring wavelength. However, unlike AMA-750, the decay behavior of AMA-680 was more analogous to Au nanocages, not MoS_2. This strongly suggested that this system was dominated by LSPR, as shown in **Figure 3.12 (b)**. It is noteworthy that AMA-680 demonstrated the longest t_1 (t_1-730, 1.4 ns) of the three AMA samples. As t_1 is the indicator of LSPR effect, it means AMA-680 was influenced by LSPR most, which can account for its highest photocatalytic activity.

Therefore, based on the fitted time constants, the AMA-460 system is a classic heterojunction photocatalyst system with Au-460 being the metal cocatalyst [**Figure 3.12 (a)**]. However, as Au is usually not considered as a great cocatalyst for HER[200], it cannot enhance the activity significantly. Meanwhile, the LSPR effect in AMA-750 just becomes strong enough to marginally overcome the classic electron transfer process [**Figure 3.12 (c)**]. Although it converts the system to a plasmonic photocatalyst system, it does not show much enhancement in activity as well due to the overall weak LSPR effect. Different from AMA-750, AMA-680 is thought to be an LSPR-dominant system [**Figure 3.12 (b)**]. It also exhibits much longer t_1 around its LSPR wavelength (t_1-730, 1.4 ns) than AMA-750 (t_1-730, 0.18 ns) and AMA-460 (t_1-495, 0.88 ns). As t_1 is the indicator of LSPR effect, it further confirms that AMA-680 has stronger LSPR effect than AMA-750 and AMA-460, which can account for its highest photocatalytic activity.

As stated in the introduction section, there are potentially several LSPR processes working simultaneously in the plasmonic photocatalyst system, namely HET, NFE and PRET. Assuming the classic electron transfer efficiency is identical for all three AMA systems (as they are prepared in the same way, the contact between Au and MoS_2 should be similar), the LSPR effect in the three systems follows the order AMA-680 > AMA-750 > AMA-460 (expressed in **Figure 3.12** by the weight of arrows) according to the TAS results. Importantly, it should be noticed that the approximations of their LSPR wavelength to the absorption edge of MoS_2 follow exactly the same order. Based on the introduction part, NFE is the only one process whose efficiency relies on the match of LSPR wavelength with the absorption edge of the semiconductor. Therefore, the results strongly evidence that NFE is the dominant LSPR process in this system. Meanwhile, the HET process was significantly suppressed probably due to the insufficient direct contact between Au nanocages and MoS_2 stated above. For the PRET process, although it does not require a direct contact, the bare MoS_2 nanosheets around Au nanocages impose a strong FRET effect, nullifying the PRET effect. NFE, however, has no competing process and can affect an area that is 50 nm away[169] hence dominates the LSPR process in the AMA-680 system.

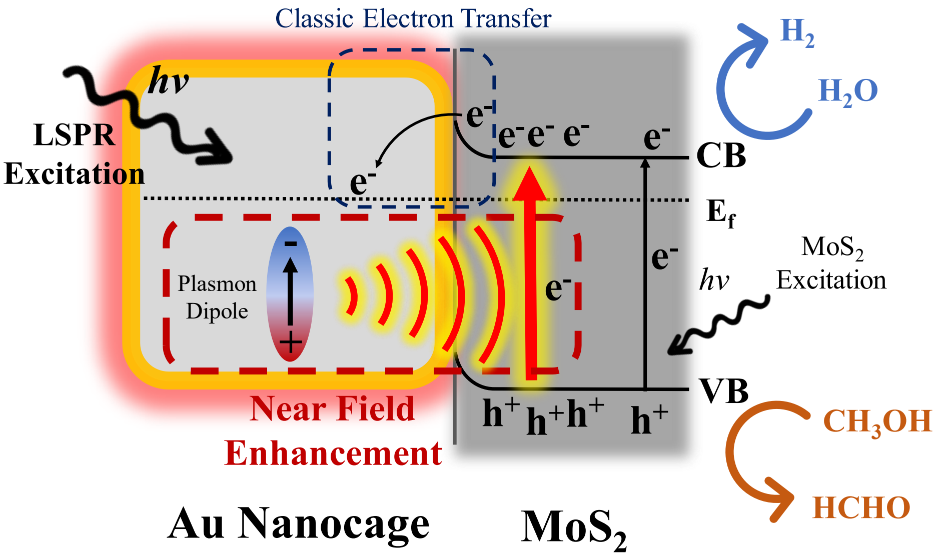

Figure 3.13 Scheme of the proposed working mechanisms in AMA-680.

Based on the above discussion, a possible mechanism is illustrated for the LSPR promoted photocatalytic hydrogen evolution reaction in the Au/MoS_2 composite as shown in **Figure 3.13**. For simplicity, only AMA-680 is presented, and 1T-like MoS_2 phase is not shown.

Under the illumination of visible light, Au-680 and MoS_2 nanosheets will be excited simultaneously. Some electrons located at the CB of MoS_2 will migrate to the Fermi level (E_f) of Au-680 by overcoming the Schottky barrier at the interface. Meanwhile, the surface plasma on Au-680 will promote the generation of electron-hole pairs in MoS_2 through the NFE process. As the LSPR wavelength of Au-680 perfectly matches the absorption edge of MoS_2 nanosheets, the ultra-efficient NFE process completely dominates the AMA-680 and hence, significantly enhances the photocatalytic performance. From our previous study on the single layer multiphasic MoS_2, we showed that the 1T-like phase of MoS_2 is more favorable for electron acceptance and hydrogen evolution. Hence, with the presence of 1T-like MoS_2, all the excited electrons in this catalyst system are more inclined and readily to transfer to 1T-like MoS_2 region to reduce water into H_2 gas. On the other side, the holes left in the VB of MoS_2 are consumed by the scavenger, methanol, to prevent the electron hole recombination as stated in Chapter 1. Through such a synergy between LSPR effect and the favorable phase structure of MoS_2, photon energy can be efficiently utilized for hydrogen evolution reaction.

3.4 Conclusions

In this chapter, MoS_2 nanosheets were successfully used as a photocatalyst to generate H_2, and the loading of Au nanocages as the metal cocatalyst has also been confirmed to have a profoundly positive impact on the catalytic activity of MoS_2. More interestingly, as a special family of metals materials with LSPR effect, the LSPR wavelength of Au nanocages was found to be a critical factor in this plasmonic photocatalyst system. Investigation of Au nanocages with various LSPR wavelengths were conducted in order to understand the effect of the LSPR wavelength on the photocatalytic hydrogen evolution reaction. The introduction of Au nanocages generally enhances the hydrogen evolution rate of the MoS_2 nanosheets. Particularly, the sample loaded with Au nanocages with the LSPR wavelength at 680 nm displayed an impressive 40-fold increase in HER rate regarding the bare MoS_2 nanosheets. Results from time-resolved TAS suggest that the key to this enhancement is related to the ultra-efficient energy transfer from Au nanocages to MoS_2 through the NFE process when the LSPR wavelength of Au nanocages matches the light absorption edge of MoS_2.

This finding gives us an inspiration that when designing a highly active plasmonic photocatalyst system, a strong interaction between the metal species and the semiconductor across the interface should be obtained. To realize this, the optical properties of both parts should be considered. A considerate selection and/or tuning of the materials should be done to obtain a perfect spectrum match between the metal and the semiconductor. In all, this chapter not only highlights the important role of the metal-semiconductor interface interaction in enhancing the photocatalytic activity of the plasmonic photocatalyst system but also presents a potentially general strategy when designing a high-performance plasmonic photocatalysts.

CHAPTER FOUR

ENHANCING THE PHOTOCATALYTIC SEMI-HYDROGENATION OF PHENYLACETYLENE BY TUNING SYNERGY BETWEEN NICKEL SITES AND SURFACE VACANCIES OF Ni/g-C_3N_4

4.1 Introduction

Following the research map in **Figure 1.8**, the research on the application of 2D material in photocatalytic TH is discussed in this chapter. As learned from the previous chapters, defects and interface interaction have been proved as key factors to the activity. Specially for the heterostructured photocatalyst system, the optical properties of the two parts are also critical to the overall performance as their perfect match is the key to achieve the optimal interface interaction. In this chapter, we aim to bring all threads together. By finely tuning the interface interaction between the two parts in the heterostructured photocatalyst via defect control, a perfect match should be achieved to yield an optimal performance.

The semi-hydrogenation of phenylacetylene (PA) is used as a model reaction in this research as it has an impressive real value in industry and can be realized through photocatalytic TH process. Polystyrene (PS), produced via the polymerization of styrene, is a widely used plastic mainly for packaging. However, in industry, the styrene feedstock obtained by dehydrogenation of ethylbenzene usually contains a portion of PA as an unwanted side product[201]. PA can deactivate the styrene polymerization catalyst and hence a poisonous component which should be controlled below 10 ppm in styrene[202, 203]. Selective hydrogenation of PA to styrene, also known as semi-hydrogenation, is thus of fundamental importance in the PS fabrication process[204].

So far, thermocatalysis is still considered as the most effective way to convert PA to styrene with appreciable selectivity[205-209]. However, this process usually requires pressurized H_2 as H source and is often accompanied with elevated temperatures (100 ~ 300 °C)[205-209]. The use of high pressure H_2 is a safety hazard while elevated temperature will lead to undesired side reactions, both of which prompt the needs of alternative routes to the thermocatalytic method[210-214].

In comparison, photocatalysis offers a greener way to conduct the reaction with satisfying selectivity (> 90%) since it requires milder conditions (typically at ambient condition)[211-217]. Additionally, it offers the possibility of TH methods that use biomass-derived like methanol[213, 214], ethanol[217] and isopropanol[212] as the H source. Combining the aforementioned merits of photocatalysis and TH in Chapter 1, photocatalytic semi-hydrogenation of PA through TH method not only prevents the use of expensive H_2, but also takes place at room temperature[211-215, 217], both of which are beneficial to build a sustainable industry as well as cut down the energy input and carbon emission from the reaction.

However, as this topic is still in its infancy in photocatalysis field, all the studies done so far are still far away from satisfactory in terms of activity. Given the limitations of photocatalysis, researchers either turned back to use H_2[211, 215, 216] or used UV light as the light source[212, 214, 217], which sabotages the potential superiority of photocatalysis. Therefore, a highly active visible-light-responsive photocatalyst that can conduct TH is desired.

As introduced in Chapter 1, a lot of efforts have been made to developing visible-light-active photocatalyst system[218-220], among which g-C_3N_4 has drawn significant attention for its 2D nature, tunable band structure, tunable surface chemistry, earth-abundant composition, etc[81]. However, the work on visible-light-active photocatalysts for PA semi-hydrogenation is quite limited. To my best knowledge, the only work was done by Jia *et al*[213]. They successfully realized the selective conversion from PA to styrene (97% styrene selectivity under 100% PA conversion) using g-C_3N_4 loaded with Ni nanoparticles. But due to the lack of detailed discussion on the interaction between the Ni species and g-C_3N_4, the understanding of how their chemical properties can affect each other and how the interface interaction between Ni and g-C_3N_4 can impact the PA semi-hydrogenation activity has not been well-established. Hence, no general guideline has been proposed for designing a highly efficient photocatalyst for the reaction.

As stated above, the motivation of this research is to figure out if tuning interface interaction can help us to exploit the full potential of a given heterogeneous photocatalyst system. In this research, the Ni/g-C_3N_4 system was adopted as the photocatalyst system for two reasons: (1) g-C_3N_4 has rich tunable surface features; (2) Ni has already been proved to have good selectivity to styrene in PA semi-hydrogenation. Introduced in Chapter 1, surface defect (*e.g.*, vacancies and dopants) engineering has been reported as an effective way to regulate the chemical properties of photocatalysts[116, 221, 222], especially 2D photocatalyst, where most atoms are exposed for defect engineering. Therefore, vacancy is selected as the tuning parameter of g-C_3N_4 for its easiness to realize and control via H_2 treatment. For Ni, as a metal species, the easiest way to tune its property is adjusting the loading. Hence, simultaneous tuning of Ni loading and surface vacancies on g-C_3N_4 is conducted in this research, and we find a unique volcano relationship between the photocatalytic performance and these two factors. Hence, a synergistic effect of metal loading and surface defect is revealed, and by controlling the two aspects to reach an optimal match, a highly active photocatalyst system is synthesized with excellent styrene selectivity (> 95%) at 100% conversion under the mildest reaction condition so far.

4.2 Experimental

4.2.1 Preparation of Ni/g-C_3N_4 photocatalyst

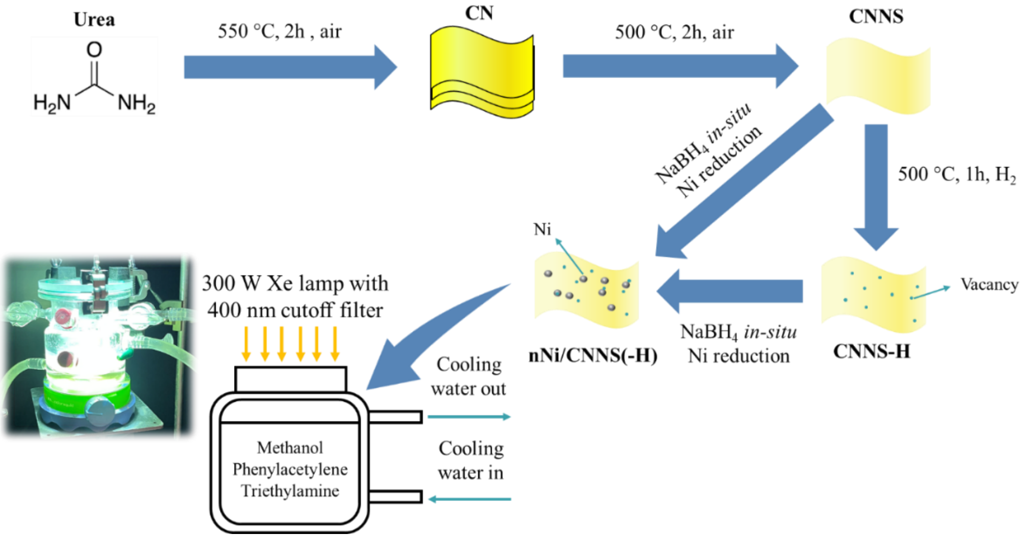

Figure 4.1 Scheme of the synthesis procedures of Ni/CNNS and Ni/CNNS-H. Inserted is a real photo of the photoreactor under illumination.

Figure 4.1 schematically shows the synthesis procedures of the Ni/g-C_3N_4 photocatalyst. Typically, 30 g urea was placed in a closed crucible with a lid and calcined under 550 °C for 2 h in a muffle furnace with a heating rate of 3 °C/min. The obtained yellow solid was bulk g-C_3N_4 (denoted as CN). Afterwards, the CN was grinded into fine powder and placed in an open crucible. Then it was calcined again under 500 ºC for 2 h in a muffle furnace with a heating rate of 5 ºC/min. The resulted pale-yellow powder was g-C_3N_4 nanosheets and labeled as CNNS.

The H_2-treated g-C_3N_4 nanosheets were obtained through a facile thermal treatment. 150 mg CNNS was placed in an open crucible and then transferred into a tube furnace. After being purged with pure H_2 for 30 min, the furnace was heated to 500 ºC with a heating rate of 5 °C/min and held for 1 h under continuous H_2 flow. The resulting powder was collected after cooling down to room temperature and labeled as CNNS-H.

To analyze the gas products during the H_2 treatment, an AMI-200 system connected to an online gas chromatograph (GC, BUCK 910) and a mass spectrometer (MS, Pfeiffer Vacuum) was used. 30 mg of CNNS was placed in the U-shape quartz tube and sealed with quartz wool. The tube was then purged with H_2/He (H_2:He = 11:4) mixed gas with a flow rate of 30 mL/min for 30 min. Then the sample was heated to 475 ºC with a heating rate of 5 ºC/min and then held for 2 h under the same atmosphere. Finally, the sample was heated to 600 ºC with a heating rate of 5 ºC/min and held for another 2 h under the same atmosphere. The GC and MS were continuously analyzing the gas product during the treatment.

Ni species were loaded on g-C_3N_4 nanosheets by an *in situ* reduction method modified from the previous work[213], which uses $Ni(NO_3)_2$ as the Ni source and $NaBH_4$ as reducing agent. Typically, 100 mg prepared g-C_3N_4 nanosheets (CNNS or CNNS-H) was dispersed in 20 ml water containing various amounts of $Ni(NO_3)_2{\cdot}6H_2O$ and stirred for 30 min in an ice-water bath. Meanwhile, 2.9 mg $NaBH_4$ was dissolved in 5 ml 0.01 M KOH aqueous solution at 0 °C, and the solution was then added dropwise into the nanosheets dispersion in 10 min using a syringe pump. During the process, the dispersion was kept under stirring in the ice-water bath. Then the dispersion was taken out of the bath and kept stirring overnight (~ 17 h). The resulting precipitation was collected and washed with DI water until neutral using a centrifuge. The final sample was obtained by vacuum-drying the solid under 60 °C, labeled as nNi/CNNS and nNi/CNNS-H (n represented the calculated Ni loading varied from 0.025 to 1 in wt.%).

4.2.2 Characterizations

XRD measurements were performed on a PANalytical X'Pert MPD Pro powder diffractometer equipped with Si-based position-sensitive one-dimensional detector and Ni-filtered Cu Kα radiation source, and the X-rays were generated with a beam wavelength of λ = 1.5416 Å (Cu Kα radiation). A Zeiss Merlin scanning electron microscope with an acceleration voltage of 2.0 kV was used for SEM imaging. The Brunauer–Emmett–Teller (BET) surface area of the samples was measured with the Micromeritics Gemini VII Surface Analyzer using N_2 as the probe gas. The UV–vis DRS was recorded using a Cary 5000 UV/Vis spectrophotometer. Photoluminescence (PL) spectra were performed on a Horiba Jobin Yvon Fluorolog fluorescence spectrometer with the excitation wavelength set to be 375 nm.

The time-resolved PL (TRPL) was measured using a time correlated single photon counting (TCSPC) (Horiba Scientific with Picosecond Photon Detection Module, PPD-850 and Fluorohub, Horiba JY IBH). The PPD-850 was mounted to a second port of a spectrometer (Acton SP2300) equipped with a CCD (Princeton Instruments, Pixis 256). The spectrometer was coupled to an upright microscope. The samples were excited using a second harmonic (400 nm) of a Ti:sapphire laser (Coherent, Mira 900) (800 nm, 5ps pulses, 76 MHz repetition rate). To match the TCSPC repetition rate requirements the laser repetition rate was reduced to ~ 5 kHz using a pulse picker (Coherent). The output of the pulse picker was frequency doubled using an ultrafast harmonic generator (Coherent 5-050) and was directed into a microscope to illuminate the samples through a 100x microscope objective (beam spot size ~ 1 μm).

XPS was performed on a Thermo Scientific K-Alpha spectrometer at an operating pressure under 3.0×10^{-7} Pa and a spot size of 400 μm using an Al-Kα microfused monochromatized source (1486.6 eV) with a resolution of 0.1 eV. All XPS data was processed using Avantage Data System, which is a software package provided by Thermo Scientific. The elemental analysis was performed by inductively coupled plasma optical emission spectroscopy (ICP-OES) on a PerkinElmer Avio 500 model instrument.

X-ray absorption spectroscopy (XAS) measurements were performed at Beamline 7-BM (QAS) of National Synchrotron Light Source II, Brookhaven National Laboratory. The samples were prepared in pellets using a hydraulic press. The Ni K edge XAS data were collected over the samples under ambient conditions in fluorescence mode.

4.2.3 Photocatalytic semi-hydrogenation of PA

As shown in **Figure 4.1**, 40 mg prepared photocatalyst was dispersed homogeneously in a reaction solution containing 40 mL methanol (0.99 mol), 140 μL triethylamine (1.00 mmol, used as hole scavenger) and 11 μL phenylacetylene (0.10 mmol) by sonication. The dispersion was then transferred into a quartz photoreactor connected to a water-cooled system to keep the reaction temperature at 25 °C. The reaction system was then purged with Ar for 20 min. Afterwards, the photoreactor was sealed tightly and illuminated by a 300 W Xe lamp (Newport) with a 400 nm cutoff filter for 21 h. The light irradiance was measured to be ~ 570 mW/cm^2 by an optical power meter equipped with a thermopile sensor from Newport. During the reaction, photoreactor was connected to a water-cooled system to keep the system temperature at 25 ºC. Liquid samples were taken at 0, 2, 4, 6, and 21 h after the beginning of the reaction and analyzed by a BUCK 910 gas chromatograph (GC) equipped with a Stabilwax column from Restek and a flame ionization detector (FID) using argon as the carrier gas. The temperature of the injection port was set as 250 ºC to gasify all the liquid chemicals. Considering the overwhelming amount of methanol in the system, it was used as the internal standard in the analysis. The conversion (%) and selectivity (%) at a given time t (h) were calculated with following equations:

$$Conversion\ (t) = \frac{C_t(PA)}{C_0(PA)}; \qquad Selectivity\ (t) = \frac{C_t(Styrene)}{C_0(PA) - C_t(PA)}$$

C_t (PA) and C_t (Styrene) refers to the concentration of PA and styrene at the given time t and C_0 (PA) means the original conversion of PA.

Considering too much catalyst dose might block the incident light during the rection, the 40 mg catalyst dose used in this research is rationalized by conducting the controlling experiment with varying doses of 0.25Ni/CNNS. As shown in **Figure 4.2**, the 6-h conversions of 20, 40 and 60 mg catalyst almost fall into a straight line passing the zero point, indicating that the light absorption efficiency can be maintained when the catalyst loading is lower than 60 mg.

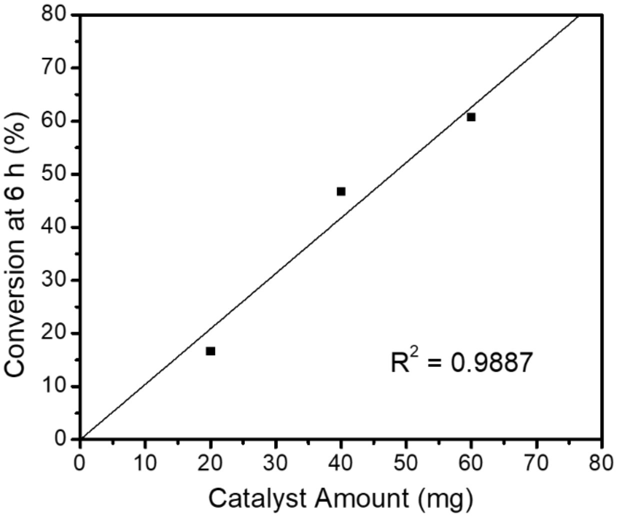

Figure 4.2 Controlling experiment with varying amount of 0.25Ni/CNNS.

4.3 Results and discussion

4.3.1 Structure and morphology

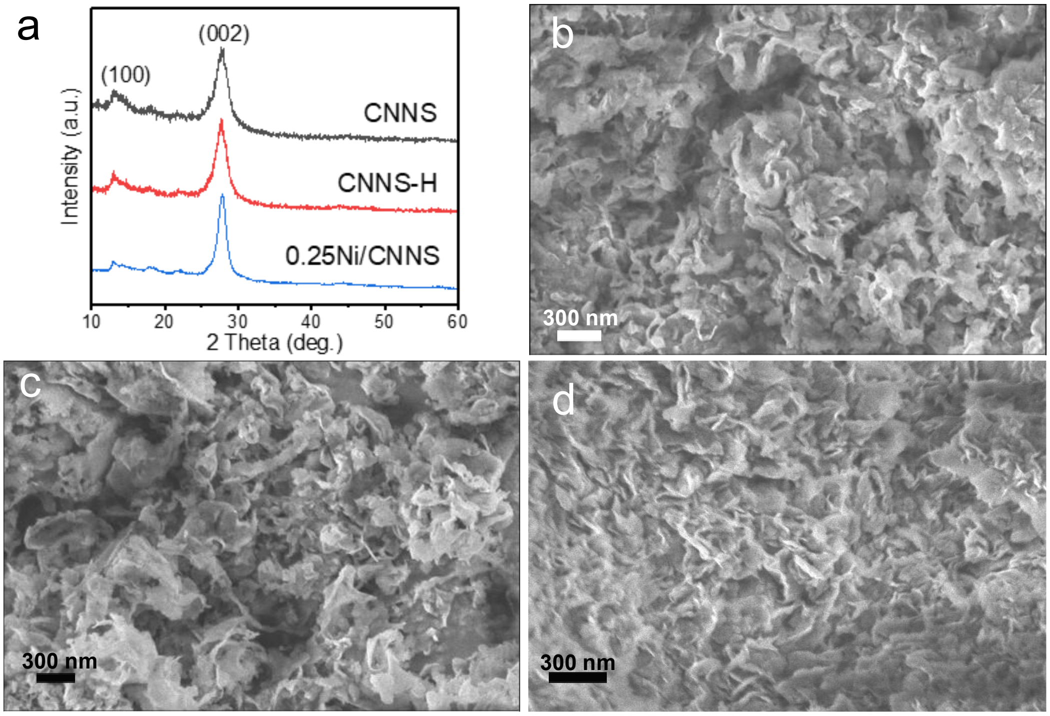

Figure 4.3 (a) XRD of CNNS, CNNS-H and 0.25Ni/CNNS, (b-d) SEM images of CNNS, CNNS-H and 0.25Ni/CNNS, respectively.

Figure 4.3 shows the XRD patterns and SEM images of CNNS, CNNS-H and Ni loaded CNNS. Since all samples show similar results, 0.25Ni/CNNS is chosen as the representative for all Ni loaded samples. As shown in **Figure 4.3 (a),** all the XRD patterns demonstrate two major characteristic peaks of g-C_3N_4. The one around 13.0° can be assigned to the (100) plane and the one around 27.7° due to (002) plane. The unnoticeable difference in XRD patterns between CNNS and CNNS-H suggests that the H_2 treatment applied in this work does not result in obvious changes of the crystal structure of g-C_3N_4. Compared with CNNS, Ni/CNNS also demonstrates a similar XRD pattern. The only difference is that the (002) peak of Ni/CNNS is sharper compared with that of CNNS, suggesting a higher crystallinity. This is because the nanosheets are packed more compactly after the vacuum drying in the Ni loading procedure. This can also be observed from SEM images of the samples [**Figure 4.3 (b-d)**], where CNNS and CNNS-H demonstrate typical loosely packed layer morphology while 0.25Ni/CNNS shows a more compact morphology. The specific surface area shown in **Table 4.1** also reveals this change. Additionally, no Ni (NiO or Ni metal) signal is observed from XRD due to the low loading and high dispersion nature as illustrated in more details in the XAS part.

Table 4.1 The specific surface area of CNNS, CNNS-H and 0.25Ni/CNNS

Sample	S_{BET} (m^2/g)
CNNS	160
CNNS-H	153
0.25Ni/CNNS	56

XPS is conducted to inspect the elemental composition of the synthesized g-C_3N_4 nanosheets before and after the H_2 treatment. **Figure 4.4** shows the full survey spectra of CNNS and CNNS-H. Three major peaks corresponding to C, N and O are clearly observed. The detailed peak fitting results of the C 1s peak and N 1s peak are shown in **Figure 4.5**. Both CNNS and CNNS-H can be fitted using the same mode. The C 1s peak can be deconvoluted into 4 peaks [**Figure 4.5 (a)**]. N=C-N (~288.0 eV) refers to C atoms in the aromatic system of g-C_3N_4, while O=C-O/CO_3 (~289.3 eV) and C-O/C-NH_x (~285.9 eV) refer to the surface groups associated with the vacancies around them. C-C (~284.6 eV) can be assigned to the adventitious carbon. The N 1s peak, on the other hand, can be deconvoluted into three peaks, as indicated in **Figure 4.5 (b)**. N-$(C)_3$ (~399.6 eV) and C=N-C (~398.4 eV) are two different types (sp^3 and sp^2-coordinated, respectively) of N atoms in the aromatic system of g-C_3N_4. N-H_x (~400.8 eV) corresponds to the surface groups. As adventitious carbon cannot be regarded as a part of the material system, the C, N and O compositions are calculated by excluding the C-C peak and listed in **Table 4.2**. C/N ratio is a widely accepted parameter to provide essential information about the vacancies in g-C_3N_4. As shown in **Table 4.2**, the CNNS has a slightly higher C/N ratio (0.87) than the theoretical value (0.75 for pristine g-C_3N_4), indicating that the as-synthesized CNNS intrinsically have N vacancies or have more N vacancies than C vacancies. After H_2 treatment, the C/N ratio of CNNS-H decreases from 0.87 to 0.73, implying that more C vacancies are further introduced during the process. By comparing **Figure 4.5 (a)** and **(b)**, the only appreciable difference is the peak intensity decrease of the C-O/C-NH_x species after the treatment. Considering the O atoms are largely removed after H_2 treatment (shown in **Figure 4.4** and **Table 4.2**), this decrease is very likely to be a result of O removal.

Another clue for the C vacancies is the identification of CH_4 produced during the H_2 treatment. With the help of online MS and GC, it is possible to monitor the exhaust gas during the H_2 treatment, and the results are shown in **Figure 4.6**. As the generation of C vacancy will produce CH_4 (possibly some other hydrocarbons) and the generation of N vacancy will produce NH_3, 4 typical m/z signals, namely 13, 15, 16 and 17 are monitored based on the standard mass spectra from National Institute of Standards and Technology (NIST). Due to the low concentration of the two produced chemicals and the high background level at 16 and 17 from system moisture, no obvious signal change is observed for their strongest signal (16 for CH_4 and 17 for NH_3) at temperatures below 475 °C. However, as indicated in **Figure 4.6**, the signals of 13 and 15 with low background start to show an uplift at a temperature around 380 °C. Although both CH_4 and NH_3 can contribute to the signal at 15, the signal 13 can only be produced from CH_4 and is hence a strong evidence for the generation of CH_4 during the process. The existence of CH_4 is also detected by GC FID and the signal is displayed as the dark yellow symbolled line in **Figure 4.6**. It almost follows the same trend as the mass spectra of 13 and 15, further confirming the production of CH_4 during the treatment starting at ~ 380 °C. Additionally, during the 2 h holding time at 475 °C, both MS and GC show a continuous generation of CH_4. Upon further temperature increase, the m/z signals at 13 and 15 show significant increase along with the signal at 16 and 17. Considering the fragmentation patterns of CH_4 and NH_3 and intensity ratio of 16/15, the intensity increase of signal at 16 can only be explained by the production NH_3 in addition to CH_4, suggesting that NH_3 is also produced during the H_2 treatment. Therefore, both MS and GC results strongly suggest that CH_4 and NH_3 can be continuously produced under 500 °C H_2 treatment temperature, which is a direct proof of the generation of both C and N vacancies. But considering the results from XPS, the C vacancies created are more than N vacancies.

The successful Introduction of surface vacancies can also be confirmed by EPR. As shown in **Figure 4.7 (a)**, a new signal with a g factor of 2.018 is observed after the H_2 treatment. It has been reported that the signal is caused by the unpaired π-electrons in the aromatic tri-s-triazine unit of g-C_3N_4 [shown in **Figure 4.7 (b)**] [106, 223], which builds the structure of g-C_3N_4 via connecting each other by the bridging N atoms at the 3 corners [indicated in **Figure 4.7 (b)**]. Therefore, the appearance of the signal is attributed to the unpaired electrons generated by the the introduction of both C and N vacancies after H_2 treatment.

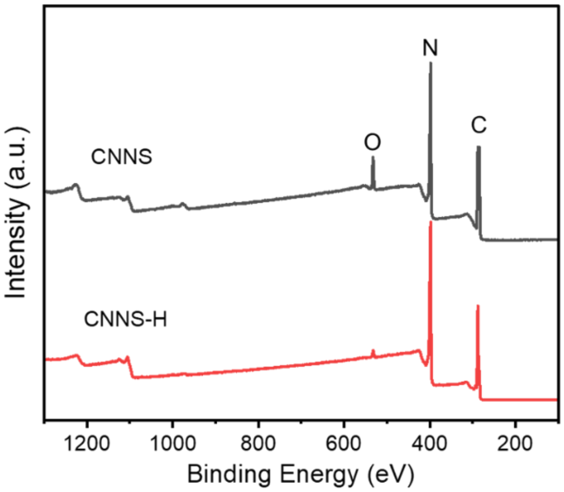

Figure 4.4 XPS survey spectra of CNNS and CNNS-H

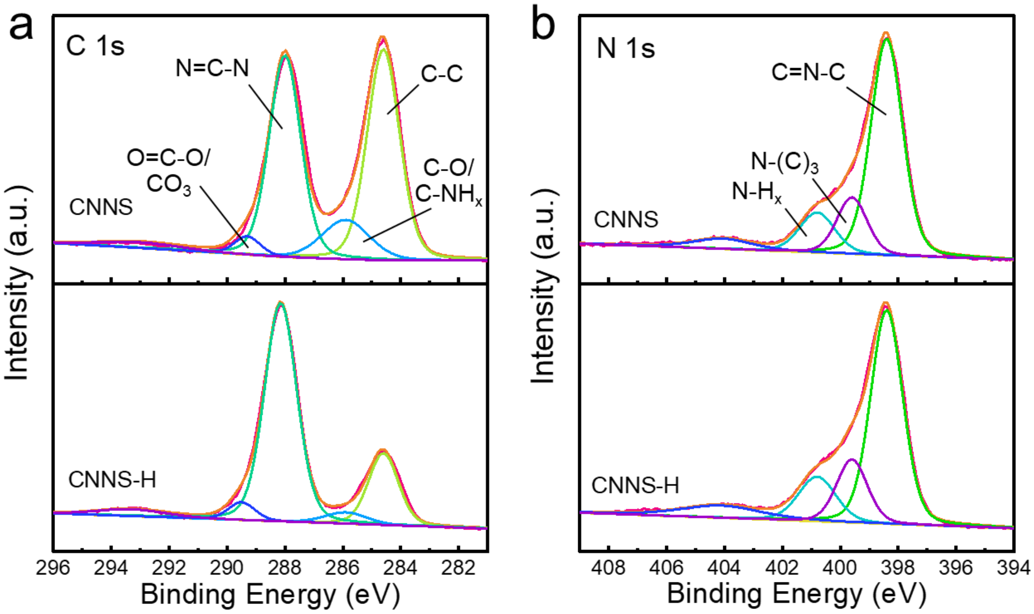

Figure 4.5 Detailed XPS peak fitting results of (a) C 1s and (b) N 1s of CNNS and CNNS-H.

Table 4.2 Element composition and calculated C/N ratio of CNNS and CNNS-H

Sample	C	N	O	C/N
CNNS	42.88	49.10	7.88	0.87
CNNS-H	41.24	56.18	2.13	0.73

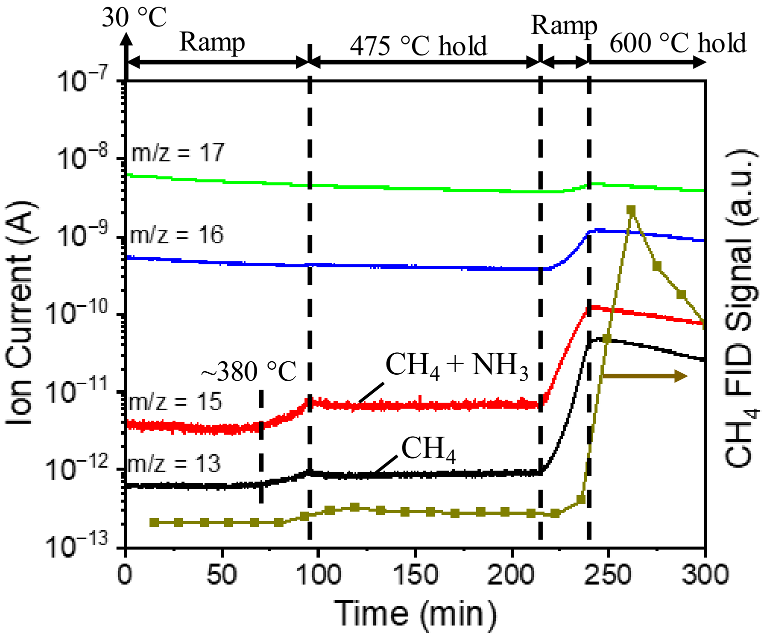

Figure 4.6 Mass spectra of 4 selected m/z signals (lines in figure) and the detected GC FID signal of CH_4 (dark yellow line with symbols in figure) as a function of H_2 treatment time. Above is the indication of the temperature program.

Considering that CNNS-H has N and C vacancies simultaneously, it is then necessary to refine the types of atomic sites in this structure. As indicated in **Figure 4.7 (b)**, besides the bridging N sites mentioned above, we herein define the 9 atomic sites outside of the red circle as the external C/N sites and the 4 sites in the circle as internal C/N sites. Therefore, there are 5 different types of atomic sites in total and they are indicated in **Figure 4.7 (b)**. Unfortunately, no further information can be obtained about the detailed locations of the vacancies, hence all 5 kinds of atomic sites are treated as potential vacancy sites here.

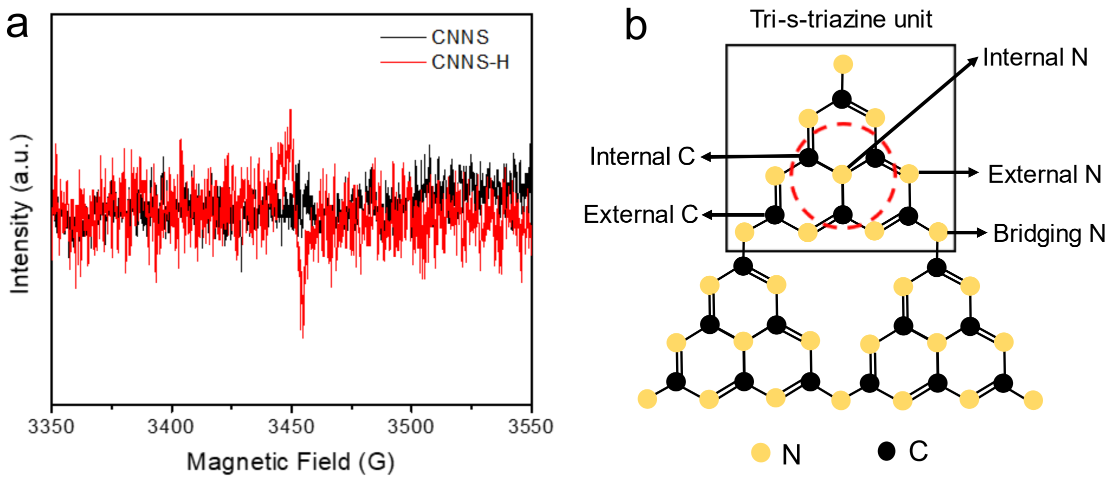

Figure 4.7 (a) EPR spectra of CNNS and CNNS-H and (b) the scheme of the g-C_3N_4 molecular structure.

It is well-known that the introduction of vacancies can alter the optical property of photocatalysts by the formation of defect level[116, 221, 222]. Therefore, UV-vis DRS and photoluminescence (PL) are conducted to inspect the optical properties of CNNS and CNNS-H. The obtained absorption spectra are shown in **Figure 4.8 (a)**. Clearly revealed in this figure is the visible light absorption enhancement from the H_2-treated sample. The optical bandgap is derived from the Tauc plot using Kubelka-Munk function versus photon energy [**Figure 4.8 (b)**]. The Kubelka-Munk function is expressed as:

$$F(R) = \frac{(1-R)^2}{2R}$$

The R refers to the collected diffuse reflectance. As listed in **Figure 4.8 (b)**, the obtained bandgaps (E_g) for CNNS and CNNS-H are 2.94 and 2.91 eV, respectively. The slight decrease in bandgap confirms the formation of sub-band defect level after H_2 treatment. The PL spectra shown in **Figure 4.8 (c)** demonstrate that after H_2 treatment, 86% of the radiative electron-hole recombination in CNNS was suppressed. Based on Chapter 1, this is because the introduced vacancies can trap electrons and holes, hence suppressing the electro-hole recombination[48, 88, 112].

Therefore, the optical property results suggest a positive effect of vacancies on photocatalytic performance as CNNS-H demonstrates a stronger visible light absorption as well as more efficient electron-hole separation.

However, as a complete photocatalysis consists of two processes, namely (1) electron-hole generation and separation and (2) surface reaction, the superiority demonstrated by CNNS-H in optical behaviors does not necessarily guarantee its higher performance in the PA semi-hydrogenation. This is not an uncommon phenomenon observed in many other semiconductor photocatalysts.

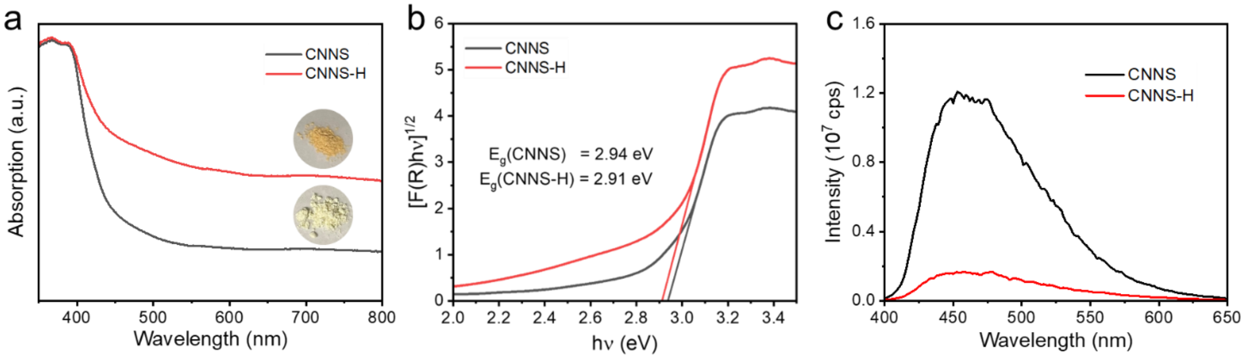

Figure 4.8 (a) UV-vis DRS of CNNS and CNNS-H (inserted were the images of the two powder samples), (b) their corresponding Tauc plots using Kubelka-Munk function versus photon energy *hν*, and (c) PL spectra of CNNS and CNNS-H.

4.3.2 Photocatalytic performance

Figure 4.9 (a-c) show the photocatalytic performance in PA conversion using Ni/ CNNS and Ni/CNNS-H samples. **Figure 4.9 (a)** displays the PA conversion versus time using Ni/CNNS samples with various loadings ranging from 0.025 wt.% to 1 wt.%. The detailed conversion and the corresponding selectivity are given in **Table 4.3**. All the samples tested demonstrate high selectivity (mostly ≥ 95 %) to styrene regardless of the conversion. Controlling experiments have been done (results shown in

Table 4.4) to demonstrate the essential roles of light illumination, TEA (scavenger), Ni metal and the catalyst (entries 1 – 4 in the table). Additionally, to better reveal the origin of the catalyst's excellent selectivity, two extra experiments are done. For entry 5, a mixed substrate containing 1% PA and 99% styrene is fed to the catalyst and only 1% of the substrate is found to be over-hydrogenated to ethylbenzene, which suggests that the 1% ethylbenzene comes from the PA, not styrene. For entry 6, pure styrene is fed to the system and no product is identified. Therefore, it is quite reasonable to assume that the good selectivity originates from the poor adsorption of styrene on the catalyst surface. Based on the above analysis, selectivity is not a challenge for this catalyst system and only the conversion rate will be discussed in this research.

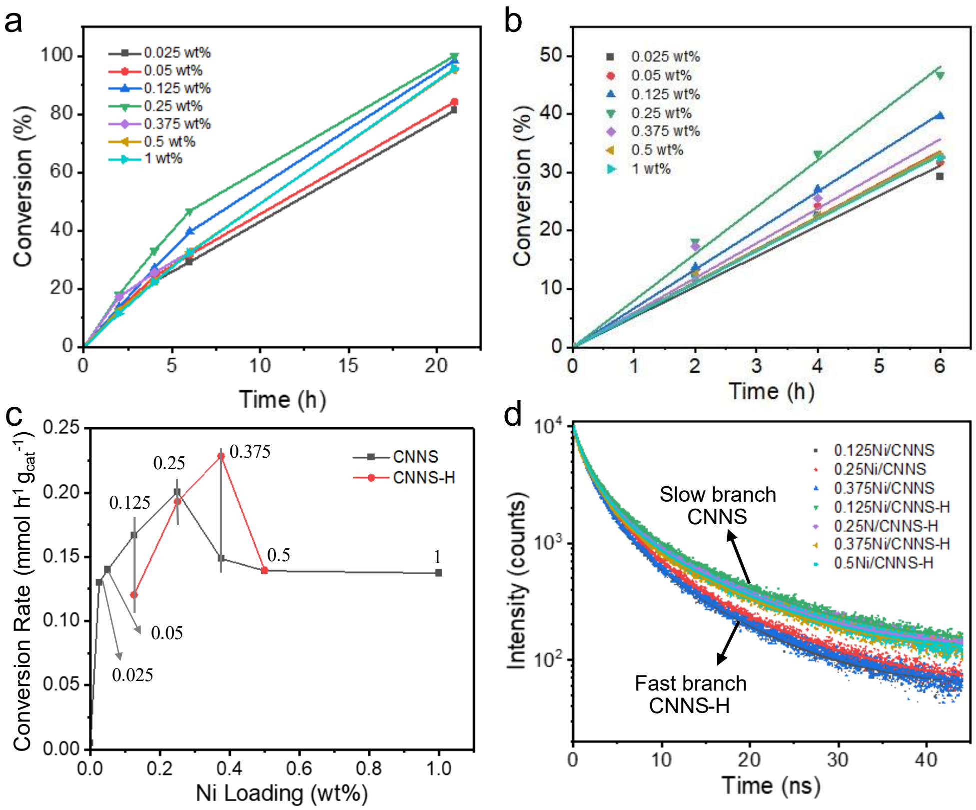

Figure 4.9 Photocatalytic performance of CNNS loaded with various amount Ni in terms of PA conversion versus time. (b)Linear fitting of the PA conversion in the first 6 h. (c) The obtained PA conversion rate of CNNS and CNNS-H versus Ni loading. (d) TRPL spectra of selected Ni/g-C_3N_4 samples.

Since the reaction is conducted in a batch reactor it is necessary to determine the reaction order of the reaction. Considering the original amount of PA is 0.10 mmol, both the scavenger (TEA, 1.00 mmol) and H donor (methanol, 0.99 mol) are in great access, they are zero-order to this reaction. To determine the reaction order of PA, three different initial PA concentrations are fed to the reaction system and the styrene yields listed in

Table 4.5 are almost constant, suggesting that this is a zero-order reaction to PA. Therefore, **Figure 4.9 (b)** shows linear fitting results of the Ni/CNNS samples' activity in the first 6 h using zero-order reaction model and the derived slopes are hence the reaction rates.

To better investigate the relationship between activity and Ni loading, all the obtained reaction rates are plotted against their corresponding Ni loadings for Ni/CNNS as the black line in **Figure 4.9 (c)**. An obvious volcano trend is observed as loading increases from 0.025 to 1 wt.% with 0.25 wt.% being the optimal point. This phenomenon might suggest that the increase of Ni loading can lead to more than one outcome that have opposite impacts on the activity, the balance of which leads to the volcano trend. When the interplay of these impacts reaches the most balanced point, the optimal activity can be achieved. In order to inspect how vacancies on g-C_3N_4 can influence this trend, the derived reaction rates of 0.125, 0.25, 0.375 and 0.5Ni/CNNS-H (red line) are plotted in **Figure 4.9 (c)**. A similar volcano trend is observed as well but shifts to the higher loading side. We therefore hypothesize that this shift is caused by the higher surface vacancy level on g-C_3N_4 support.

Additionally, it is interesting to find that the activity depends more on the Ni loading than the optical properties of the g-C_3N_4 supports. Considering the loading of 0.375 wt.%, CNNS-H is apparently better than CNNS. For higher loading like 0.5 wt.%, CNNS and CNNS-H demonstrate no obvious difference. For lower loadings like 0.125 and 0.25 wt.%, CNNS-H even shows inferior performance. Therefore, it possibly implies that the surface reaction part is more decisive than the optical process part in this photocatalytic rection system.

Given that cocatalyst can facilitate electron-hole recombination, it may bring extra change to the optical behavior of the support. However, considering the small variance of the Ni loadings among the samples, the ordinary optical characterization techniques cannot be used to observe the subtle change. Time-resolved PL (TRPL) is an advanced PL technique that monitors the decay of PL signal at a given wavelength instantly after the excitation. It aims to provide more information of samples that have undistinguishable PL behavior and is hence an useful tool to disentangle the Ni-loaded samples. **Figure 4.9 (d)** displays the TRPL spectra of the 7 selected key samples, and two distinct spectrum groups can be clearly observed. The one that decays faster is purely composed by the CNNS samples and the other group that decays slower consists of the CNNS-H samples.. The decay spectra are fitted to a tri-exponential model:

$$I(t) = A_1 e^{-\frac{t}{t_1}} + A_2 e^{-\frac{t}{t_2}} + A_3 e^{-\frac{t}{t_3}}$$

$I(t)$ is the transient PL intensity at a given time t (ns), A_i are the weighing factors (i = 1, 2, or 3) and t_i (i = 1, 2, or 3) are the time variants. The average lifetime <t> (ns) of the excited electrons can then be calculated using the equation:

$$< t >= \frac{A_1 t_1^2 + A_2 t_2^2 + A_3 t_3^2}{A_1 t_1 + A_2 t_2 + A_3 t_3}$$

.

Table 4.3 The corresponding PA conversion and styrene selectivity of all the data points shown in **Figure 4.9 (c)**

Substrate	Ni/wt.%	Conversion/%	Selectivity/%
CNNS	0.025	81	98
	0.05	84	97
	0.125	95	>99
	0.25	100	>99
	0.375	100	>99
	0.5	100	>99
	1	96	95
CNNS-H	0.125	35	>99
	0.25	98	>99
	0.375	100	95
	0.5	98	93

Table 4.4 Control experiments using 0.25Ni/CNNS as the catalyst.

Entry	Condition change	Styrene yield/%	Ethylbenzene yield /%
1	No light	-	-
2	No TEA	2	-
3	No catalyst	-	-
4	No Ni loaded	4	-
5	1% PA in styrene	99	1
6	Styrene instead of PA	100	-

Table 4.5 Styrene yields after 6 h reaction under different PA initial concentrations.

Initial PA concentration (mM)	Styrene yield after 6 h (μmol)
1.25	45.6
2.50*	46.7
5.00	47.0

*The standard concentration used in all the other reactions.

Table 4.6 Fitting results of the TRPL spectra of the 7 selected samples and the calculated average lifetime.

Support	Ni/wt.%	A_1/%	T_1/ns	A_2/%	t_2/ns	A_3/%	t_3/ns	<t>/ns
CNNS	0.125	0.27	0.65	0.55	2.19	0.17	7.92	4.92
	0.25	0.40	1.14	0.43	3.19	0.12	10.18	5.69
	0.375	0.33	0.87	0.48	2.5	0.15	8.54	5.11
CNNS-H	0.125	0.27	0.72	0.51	2.52	0.21	9.98	6.78
	0.25	0.25	0.66	0.49	2.39	0.20	9.49	6.46
	0.375	0.24	0.47	0.54	2.09	0.20	9.01	6.13
	0.5	0.29	0.68	0.51	2.4	0.19	9.67	6.39

As listed in **Table 4.6**, the variance of the obtained <t> for the same support is quite small (6.25 % for CNNS and 3.60 % for CNNS-H) while all CNNS samples demonstrate much shorter <t> than CNNS-H samples. Therefore, we postulate that the optical properties of the bare g-C_3N_4 nanosheets have a negligible impact on the optical properties of Ni-loaded samples in our study. Therefore, the photocatalytic activity of the Ni/g-C_3N_4 samples in this reaction is controlled by the surface reaction process, which will be delineated below.

4.3.3 Discussion on the impact of Ni loading and vacancy level on the activity

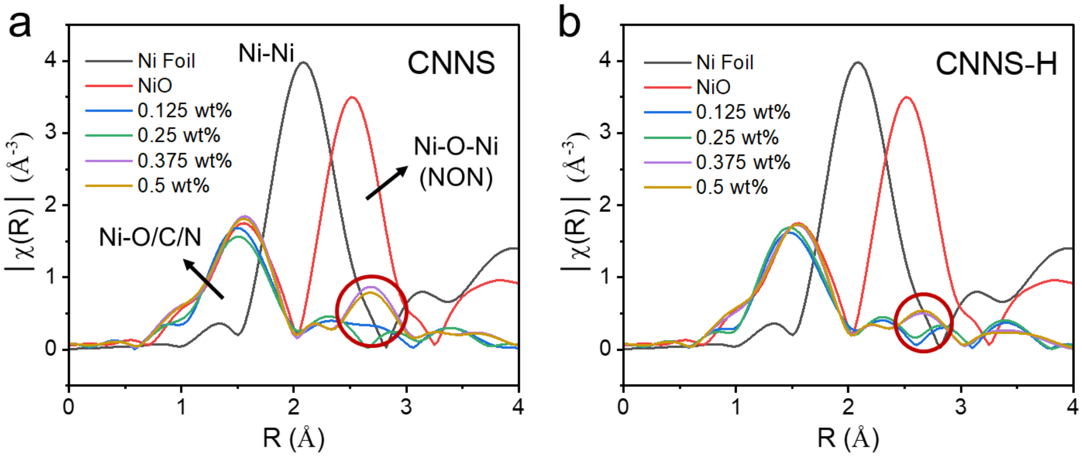

Figure 4.10 EXAFS spectra of (a) CNNS and (b) CNNS-H loaded with 0.125, 0.25, 0.375 and 0.5 wt.% Ni along with Ni foil and NiO as references.

Since the cocatalyst is regarded as the real reaction center, inspection on the nature of surface Ni species is then critical to study the surface reaction process of the catalyst system. Therefore, Extended X-ray Absorption Fine Structure (EXAFS) is conducted as it is a powerful weapon in X-ray Absorption Spectroscopy (XAS) family for investigating the coordination environment around metal species. **Figure 4.10** showed the EXAFS spectra of CNNS and CNNS-H with various loadings of Ni. The loadings of 0.125, 0.25, 0.375 and 0.5 wt.% are selected for both supports to study the structural change of Ni species near their turning point. With Ni foil being the reference, it is clearly shown that the Ni-Ni bond signal around 2.0 Å is absent for all the 8 samples examined, meaning that the Ni species on all these samples are in the form of single-atoms (SAs). Instead of forming metal bonds, the Ni SAs tend to bond to the surface atoms on g-C_3N_4, displaying a signal around 1.5 Å that can be assigned to Ni-O/C/N. Unfortunately, as EXAFS cannot distinguish C, N or O from each other, the exact assignment of this signal cannot be made. An interesting finding is that when the Ni loading on CNNS increases to 0.375 wt.% [purple line in **Figure 4.10 (a)**], a new peak (circled in the figure) around 2.7 Å is observed. As 0.375 wt.% Ni is right at the activity turning point of Ni/CNNS samples [**Figure 4.9 (c)**], it implies that the appearance of the new signal could be related to the abrupt activity decrease. Based on the reference spectrum of NiO, it is found that the new peak is quite close to the Ni-O-Ni (NON) bonding of NiO. Therefore, the new peak can probably be assigned to Ni-C-Ni or Ni-N-Ni. But as stated above, EXAFS is quite ambiguous on C, N and O, we herein refer to this new peak as NON-like bonding mode. This peak suggests that when Ni loading increases to a critical level, a new bonding mode will come into play where two Ni SAs are getting close and bonding to the same atom. As reported previously, metal SA inclines to anchor on vacancy sites, no matter C vacancy[224] or N vacancy[225] and form Ni-C and/or Ni-N bonds with the surrounding atoms. Therefore, we assumed that there should be a critical Ni loading that is just enough to occupy all the vacancy sites. Once the loading exceeds the critical value, there will be an emerging possibility where two Ni atoms anchor on the same vacancy site, forming a NON-like bonding mode with the surface C or N atoms being the bridging atoms. The hypothesized detailed bonding modes in the g-C_3N_4 structure are schematically shown in **Figure 4.11**. According to the previous discussion, 5 different types of vacancy sites are shown in the figure. Under all 5 cases, there is a possibility of the formation of NON-like bonding [indicated with red outline in **Figure 4.11 (b)**]. Therefore, this hypothesis could account for the appearance of the new signal around 2.7 Å.

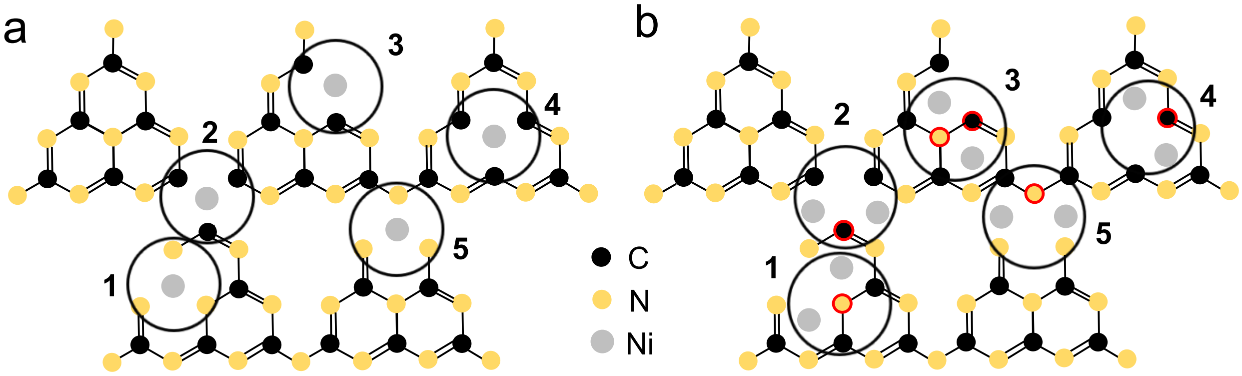

Figure 4.11 Schematic illustration of (a) completely isolated Ni SAs anchored on the vacancy sites and (b) the formation of NON-like bonding mode when Ni loading is beyond the critical value. All 5 kinds of vacancy sites are shown here, namely (1) internal C vacancy, (2) bridging N vacancy, (3) external N vacancy (4) internal N vacancy and (5) external C vacancy. All the possible bridging atoms for NON-like bonding modes are highlighted with red outlines.

For CMMS-H [**Figure 4.10 (b)**], like CNNS, the NON-like peak signal is also observed when Ni loading reaches 0.375 wt.%. The only difference is that the NON-like peaks are weaker than those of CNNS. This can be attributed to the higher vacancy level on the CNNS-H surface. The larger amount of vacancies can provide more anchoring sites and hence suppress the formation of the NON-like bonding mode, which also means that Ni SAs are more separated on CNNS-H.

Electronic structure is another aspect that could have a significant impact on the surface reaction process as it controls the adsorption behaviors of the reactants. Hence, X-ray Absorption Near Edge Spectroscopy (XANES), another branch of XAS, is also performed to inspect the electronic structure of the Ni SAs and the results are shown in **Figure 4.12**. The XANES spectra of all the Ni/g-C_3N_4 samples exhibit the similar profile to that of NiO. However, compared with NiO, the Ni/g-C_3N_4 samples show lower intensity of the peak at 8350 eV. Given that g-C_3N_4 has been widely accepted to have a negatively charged surface for its negative zeta potential under neutral condition[226-228], the relatively lower peak intensity can be explained by the electron-donating feature of g-C_3N_4 surface. When the Ni SAs are loaded on the surface as a cation, their electron density increases due to the electron-donating effect from g-C_3N_4. Another important finding is that for both CNNS [**Figure 4.12 (a)**] and CNNS-H [**Figure 4.12 (b)**], the peak intensities demonstrate a tendency to increase when Ni loading increases, indicating that the electron density of Ni SAs will decrease as more Ni SAs are loaded on g-C_3N_4. This is because as more Ni SAs are loaded as cations, the electron-donating effect of g-C_3N_4 will become less obvious for every Ni SA. The decreased electron density of Ni can lead to two significant outcomes: strong adsorption of PA on Ni and slow dissociation of H from methanol on Ni[229]. According to the reaction mechanism introduced in Chapter 1, both the substrate and H dissociation on metal are essential intermediate steps of the hydrogenation reaction. Hence as what we hypothesized previously, these two outcomes can pose two opposite effects on the reaction, forming a volcano relationship between the intrinsic activity of Ni SAs and the electron density of them with a turning (optimal) point somewhere in between, as illustrated in **Figure 4.13**. This volcano is thought to be the foundation of the volcano trend showed in **Figure 4.9 (c)**.

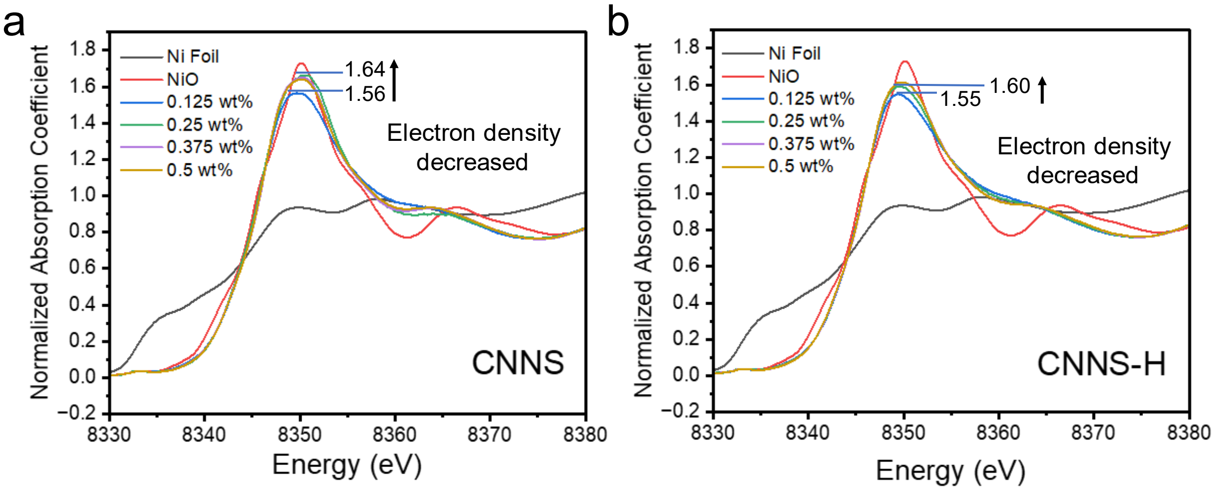

Figure 4.12 XANES spectra of (a) CNNS and (b) CNNS-H loaded with various amount of Ni.

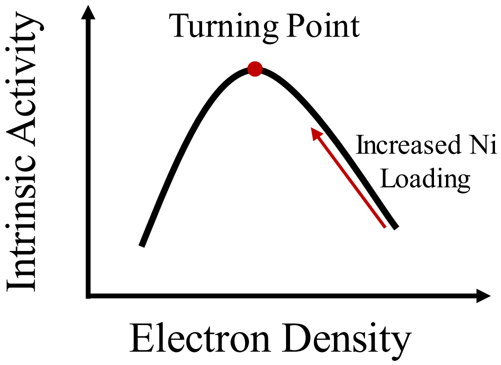

Figure 4.13 Illustration of the relationship between the intrinsic activity of Ni SAs and their electron density. The electron density of each Ni SA will decrease as Ni loading increases, indicated by the red arrow in the figure.

Additionally, comparing CNNS [**Figure 4.12 (a)**] and CNNS-H [**Figure 4.12 (b)**], it is found that Ni/CNNS-H samples generally show lower peak intensity at similar Ni loading than the Ni/CNNS samples, which suggests that the introduction of vacancies can enhance the electron-donating effect of g-C_3N_4. The stronger electron-donating effect from CNNS-H hinders the Ni electron density decrease as we increase the Ni loading. Besides, as known from EXAFS, CNNS tend to have more NON-like bonding modes as a result of the limit of vacancy sites while CNNS-H has more separated Ni SAs on the surface. The different bonding modes also can have an impact on the electronic structure of Ni SAs, as schematically shown in **Figure 4.14**. For NON-like bonding [**Figure 4.14 (a)**], the electron-donating effect posed by one vacancy site will be shared by two Ni atoms while under highly separated situation [**Figure 4.14 (b)**], all the electron-donating effect of one vacancy site will pose on one Ni atom. Therefore, from the viewpoint of both the total electron-donating effect and the Ni bonding mode, the Ni SAs on CNNS-H would have higher electron density due to the electron-donating effect from the vacancies in the support than on CNNS. Consequently, as the Ni loading increases, the electron density of the Ni SAs on CNNS-H will decrease slower than those on CNNS, making it slower for CNNS-H to reach the turning point shown in **Figure 4.13**.

Finally, a full explanation can be made to address the different activity trends demonstrated by CNNS and CNNS-H in **Figure 4.9**. As analyzed above, a volcano relationship exists in the Ni/g-C_3N_4 system between the intrinsic activity and the electron density of every Ni SAWith the increase of Ni loading, the electron density of Ni SAs on CNNS-H will reach the turning point of the volcano shape (**Figure 4.13**) slower than those on CNNS-H, which accounts for the total activity turning point of CNNS-H shifted to a higher Ni loading (from 0.25 wt.% for CNNS to 0.375 wt.% for CNNS-H). Since CNNS-H can host a higher density of Ni SAs at the turning point than CNNS, it demonstrates higher photocatalytic activity than CNNS at the own turning point.

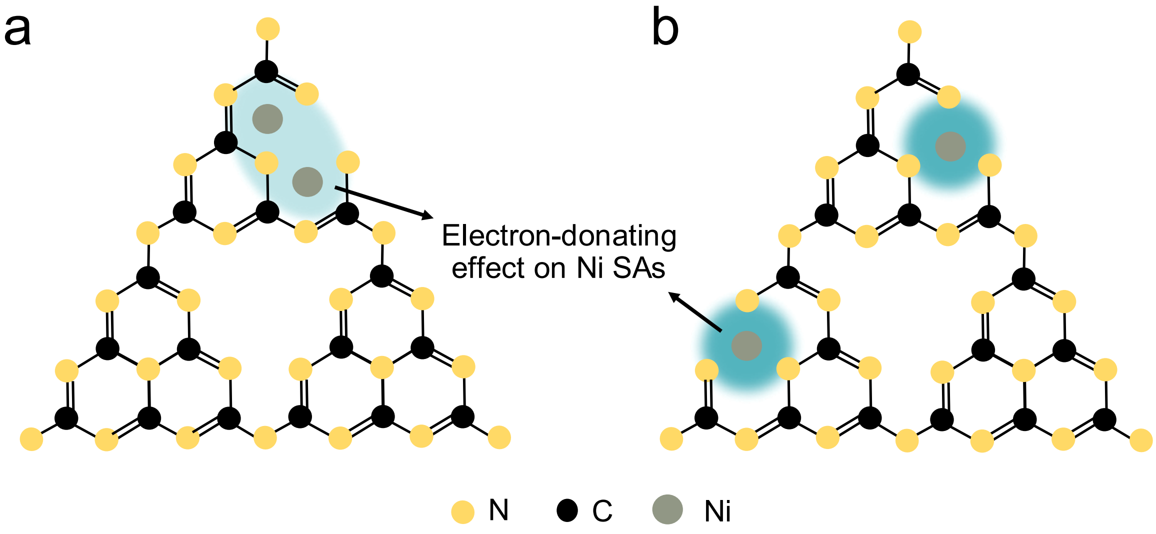

Figure 4.14 Schematic illustration of the electron-donating effect of g-C3N4 on Ni SAs under (a) NON-like bonding mode and (b) highly separated bonding mode .

4.4.4 Stability test

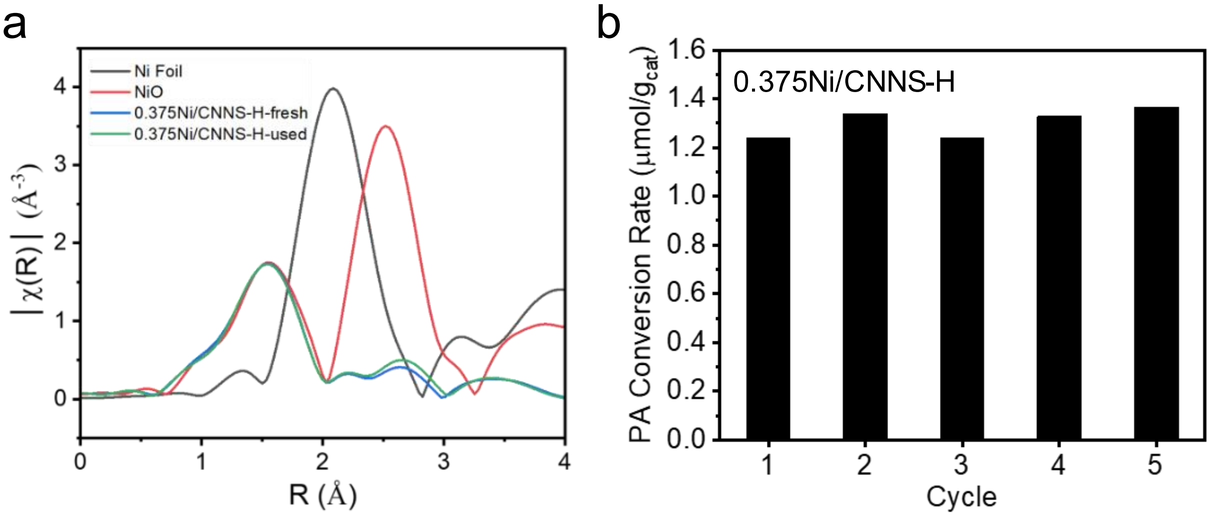

Figure 4.15 (a) the EXAFS spectra of 0.375Ni/CNNS-H before and after one standard 21 h run with Ni foil and NiO being the references (b) 6 h short-time stability test of 0.375Ni/CNNS-H for 5 cycles and.

Finally, as the most active photocatalyst, 0.375Ni/CNNS-H is used as a representative to study the stability of the materials. In **Figure 4.15 (a)**, EXAFS spectrum of the used 0.375Ni/CNNS-H after a 21 h standard run is shown along with the spectrum of the fresh sample. Both spectra are almost the same except that a slight intensity increase on the NON-like bond signal is observed, suggesting that the majority of the isolated Ni SAs can still maintain the atomic dispersion on the surface while they indeed show a slight tendency to aggregate. However, this slight aggregation tendency does not impact the catalytic stability under our testing conditions. As displayed in **Figure 4.15 (b)**, after 5 cycles of short-term (6 h) cyclic performance test, the PA conversion rate can be maintained, which strongly suggests the good stability of the as-synthesized Ni/g-C_3N_4 samples in this reaction.

4.4 Conclusions

In this chapter, the complicated relationship between activity, Ni SA loading and g-C_3N_4 surface vacancies are studied in the Ni/g-C_3N_4 photocatalyst system using PA semi-hydrogenation as a model reaction. H_2 treatment is used to create vacancies on g-C_3N_4 nanosheets. By combining XPS, MS and GC, the creation of more C vacancies is confirmed after the treatment. It is found that the activity of Ni/g-C_3N_4 demonstrates a volcano shape with respect to Ni SA loading. The introduction of vacancies is proved as a potential way to increase the activity of the catalyst while guaranteeing a good stability. With the help of XAS techniques (EXANES and EXAFS), we found two important phenomena: (1) the electron density of the Ni SAs on g-C_3N_4 decreases as their loading increases and (2) the decrease trend can be slow down when more vacancies are introduced to the surface of g-C_3N_4. Considering that the electron density can neither be too high or too low for hydrogenation reaction, the first information gives us a volcano relationship between intrinsic activity and electron density of Ni SAs with an optimal point and the second one implies that the g-C_3N_4 support with higher vacancy level would be able host more Ni SAs to reach the optimal intrinsic activity, which in turn gives the g-C_3N_4 higher activity.

In all, this research provides some insights into the interplay between vacancy level and Ni SA loading and demonstrates that the simultaneous tuning of chemical properties of both cocatalyst and semiconductor is an effective methodology to improve the catalytic performance. The results and proposed explanation can provide a potentially general designing strategy for metal-SA-loaded photocatalysts used for organic transformations: for a semiconductor support with stable surface chemistry, the critical value should be found to achieve the optimal performance. For a semiconductor support with tunable surface chemistry like g-C_3N_4, the maximal defect level that the material can hold should be achieved first, followed by the determination of the corresponding critical metal loading. Then it is obvious that the 2D materials with tunable surface chemistry should have a greater potential as a support since they can provide more defect sites to metal SAs.

CHAPTER FIVE

SUMMARY AND CONCLUSIONS

In this dissertation, the research map shown in **Figure 1.8** is followed to design highly active electrocatalyst and photocatalyst for HER and TH using 2D materials. Thanks to the unique physiochemical and optoelectronic properties of 2D materials, an ideal platform is offered to conduct comprehensive and in-depth studies that can potentially provide general designing strategies for highly performance electro/photocatalysts that can be used in achieving the hydrogen economy.

Firstly, the potential of defective MoS_2 nanosheets in electrocatalytic HER is demonstrated by fabricating the MoS_2/CFP PEM electrode via a facile one-step synthesis procedure. The fabricated electrode demonstrates a superior electrocatalytic HER activity in a PEM cell with an extra low MoS_2 loading. The ultrahigh activity of the as-synthesized electrode was attributed to the intimate contact between MoS_2 and CFP from the in situ growth, vertical alignment of MoS_2 nanosheets on CFP, the coexistence of 1T and 2H multiphase MoS_2 and the existence of various defects on MoS_2 nanosheets like atomic vacancies, pinholes and distorted edges. The results manifest that MoS_2 has a great potential for catalytic HER and the surface defects are valuable merits of 2D material that can be taken advantage of when designing the HER catalysts. In particular, the intimate contact between MoS_2 and CFP support is also considered a key contributor to its superior performance, which gives us an inspiration that a strong interaction between the different parts of the catalyst is also critical to obtain a high performance.

Next, considering the potential of MoS_2 for catalytic HER, it is further adopted as the photocatalyst for HER, but modified by loading Au nanocages to facilitate the electron-hole generation and separation. By combining it with Au nanocage, which has strong LSPR effect and tunable LSPR wavelength, the fabricated heterogeneous Au/MoS_2 photocatalyst offers us a great opportunity to study the impact of LSPR properties on MoS_2. Interestingly, it is found that the LSPR wavelength of Au nanocages is a critical factor for the activity of the system. When the LSPR wavelength of Au nanocages matches the optical absorption edge of MoS_2, the activity is boosted the most. After detailed characterizations and analysis, it is concluded that there is a competition between classic electron transfer (from MoS_2 to Au) and plasmonic energy transfer (from Au to MoS_2) and near field enhancement (NFE) is regarded as the governing LSPR mechanism in this system. This research further confirms that the synergistic interaction between the components of the catalyst system is a noteworthy designing factor. Finally, built upon the learning of the important roles played by surface defects and metal-semiconductor interaction in catalysis, the last research work moves forward to study how we can manipulate the catalytic activity by controlling both aspects. A photocatalyst system composed by Ni SA and g-C_3N_4 nanosheets is fabricated for their tunable physical and chemical properties and PA semi-hydrogenation reaction is selected as a model reaction for its real industrial value. By conducting a series of deliberately designed experiments and characterizations, the synergistic effect of defect, Ni loading and metal-semiconductor interaction on activity is completely revealed and well explained, and a general strategy for designing highly active SA loaded catalyst for organic transformation is proposed.

In summary, the primary objective of this dissertation is to provide a comprehensive guideline for designing high-performance electro/photocatalysts used in realizing the hydrogen economy. Through the experiments and discussions presented in the above chapters, the pivotal roles of surface defects and interface interactions on the catalytic behavior of heterostructured materials have been illustrated. Hopefully, this work will inspire future research endeavors aimed at establishing generalized design strategies for highly active catalysts not just for hydrogen-related reactions, but also for a broader spectrum of chemical processes.

REFERENCES

1. Bullock, M.; More, K., Basic Energy Sciences Roundtable: Foundational Science for Carbon-Neutral Hydrogen Technologies (Report). DOESC Office of Basic Energy Sciences: 2022.
2. Nazir, H.; Louis, C.; Jose, S.; Prakash, J.; Muthuswamy, N.; Buan, M. E. M.; Flox, C.; Chavan, S.; Shi, X.; Kauranen, P.; Kallio, T.; Maia, G.; Tammeveski, K.; Lymperopoulos, N.; Carcadea, E.; Veziroglu, E.; Iranzo, A.; Kannan, A. M., Is the H_2 economy realizable in the foreseeable future? Part I: H_2 production methods. *Int J Hydrogen Energ* **2020,** *45* (27), 13777-13788.
3. Kuang, P. Y.; Sayed, M.; Fan, J. J.; Cheng, B.; Yu, J. G., 3D Graphene-Based H_2-Production Photocatalyst and Electrocatalyst. *Adv Energy Mater* **2020,** *10* (14).
4. Abe, J. O.; Popoola, A. P. I.; Ajenifuja, E.; Popoola, O. M., Hydrogen energy, economy and storage: Review and recommendation. *Int J Hydrogen Energ* **2019,** *44* (29), 15072-15086.
5. Liu, H. Z., Ammonia synthesis catalyst 100 years: Practice, enlightenment and challenge. *Chinese J Catal* **2014,** *35* (10), 1619-1640.
6. Wang, Q. R.; Guo, J. P.; Chen, P., Recent progress towards mild-condition ammonia synthesis. *J Energy Chem* **2019,** *36*, 25-36.
7. Chinchen, G. C.; Waugh, K. C.; Whan, D. A., The Activity and State of the Copper Surface in Methanol Synthesis Catalysts. *Appl Catal* **1986,** *25* (1-2), 101-107.
8. Liu, G. B.; Yang, G. H.; Peng, X. B.; Wu, J. H.; Tsubaki, N., Recent advances in the routes and catalysts for ethanol synthesis from syngas. *Chem Soc Rev* **2022,** *51* (13), 5606-5659.
9. Stanislaus, A.; Cooper, B. H., Aromatic Hydrogenation Catalysis - a Review. *Catal Rev* **1994,** *36* (1), 75-123.
10. Liu, Z. P.; Zhang, L.; Ren, Z. P.; Zhang, J., Advances in Selective Electrocatalytic Hydrogenation of Alkynes to Alkenes. *Chem-Eur J* **2023**.
11. Iulianelli, A.; Liguori, S.; Wilcox, J.; Basile, A., Advances on methane steam reforming to produce hydrogen through membrane reactors technology: A review. *Catal Rev* **2016,** *58* (1), 1-35.
12. Zhang, H. T.; Sun, Z. X.; Hu, Y. H., Steam reforming of methane: Current states of catalyst design and process upgrading. *Renew Sust Energ Rev* **2021,** *149*.
13. Barelli, L.; Bidini, G.; Gallorini, F.; Servili, S., Hydrogen production through sorption-enhanced steam methane reforming and membrane technology: A review. *Energy* **2008,** *33* (4), 554-570.
14. Gong, M.; Wang, D. Y.; Chen, C. C.; Hwang, B. J.; Dai, H. J., A mini review on nickel-based electrocatalysts for alkaline hydrogen evolution reaction. *Nano Res* **2016,** *9* (1), 28-46.
15. Wu, Z. P.; Lu, X. F.; Zang, S. Q.; Lou, X. W., Non-Noble-Metal-Based Electrocatalysts toward the Oxygen Evolution Reaction. *Adv Funct Mater* **2020,** *30* (15).
16. Yuan, N. N.; Jiang, Q. Q.; Li, J.; Tang, J. G., A review on non-noble metal based electrocatalysis for the oxygen evolution reaction. *Arab J Chem* **2020,** *13* (2), 4294-4309.
17. Chen, Z. W.; Higgins, D.; Yu, A. P.; Zhang, L.; Zhang, J. J., A review on non-precious metal electrocatalysts for PEM fuel cells. *Energ Environ Sci* **2011,** *4* (9), 3167-3192.
18. Jayabal, S.; Saranya, G.; Wu, J.; Liu, Y. Q.; Geng, D. S.; Meng, X. B., Understanding the high-electrocatalytic performance of two-dimensional MoS_2 nanosheets and their composite materials. *J Mater Chem A* **2017,** *5* (47), 24540-24563.

19. Li, X.; Yu, J. G.; Wageh, S.; Al-Ghamdi, A. A.; Xie, J., Graphene in Photocatalysis: A Review. *Small* **2016,** *12* (48), 6640-6696.

20. Li, X.; Yu, J. G.; Low, J. X.; Fang, Y. P.; Xiao, J.; Chen, X. B., Engineering heterogeneous semiconductors for solar water splitting. *J Mater Chem A* **2015,** *3* (6), 2485-2534.

21. Graetz, J., New approaches to hydrogen storage. *Chem Soc Rev* **2009,** *38* (1), 73-82.

22. Zuttel, A., Hydrogen storage methods. *Naturwissenschaften* **2004,** *91* (4), 157-172.

23. Wang, G. B.; Xie, K. H.; Kan, J. L.; Xu, H. P.; Zhao, F.; Wang, Y. J.; Geng, Y.; Dong, Y. B., In situ utilization of photogenerated hydrogen for hydrogenation reaction over a covalent organic framework. *Chem Commun* **2023,** *59* (11), 1493-1496.

24. Xie, K. Y.; Kamali, A. R., Molten salt electrochemical production and in situ utilization of hydrogen for iron production. *Int J Hydrogen Energ* **2019,** *44* (45), 24353-24359.

25. Kumar, A.; Bhardwaj, R.; Mandal, S. K.; Choudhury, J., Transfer Hydrogenation of CO_2 and CO_2 Derivatives using Alcohols as Hydride Sources: Boosting an H_2-Free Alternative Strategy. *Acs Catal* **2022,** *12* (15), 8886-8903.

26. Ito, J.; Nishiyama, H., Recent topics of transfer hydrogenation. *Tetrahedron Lett* **2014,** *55* (20), 3133-3146.

27. Wang, D.; Astruc, D., The Golden Age of Transfer Hydrogenation. *Chem Rev* **2015,** *115* (13), 6621-6686.

28. Jin, X.; Yin, B.; Xia, Q.; Fang, T. Q.; Shen, J.; Kuang, L. Q.; Yang, C. H., Catalytic Transfer Hydrogenation of Biomass-Derived Substrates to Value-Added Chemicals on Dual-Function Catalysts: Opportunities and Challenges. *Chemsuschem* **2019,** *12* (1), 71-92.

29. Deng, D. H.; Novoselov, K. S.; Fu, Q.; Zheng, N. F.; Tian, Z. Q.; Bao, X. H., Catalysis with two-dimensional materials and their heterostructures. *Nat Nanotechnol* **2016,** *11* (3), 218-230.

30. Luo, B.; Liu, G.; Wang, L. Z., Recent advances in 2D materials for photocatalysis. *Nanoscale* **2016,** *8* (13), 6904-6920.

31. Zhou, M.; Lou, X. W.; Xie, Y., Two-dimensional nanosheets for photoelectrochemical water splitting: Possibilities and opportunities. *Nano Today* **2013,** *8* (6), 598-618.

32. Sun, Y. F.; Gao, S.; Lei, F. C.; Xie, Y., Atomically-thin two-dimensional sheets for understanding active sites in catalysis. *Chem Soc Rev* **2015,** *44* (3), 623-636.

33. Sun, Y. F.; Liu, Q. H.; Gao, S.; Cheng, H.; Lei, F. C.; Sun, Z. H.; Jiang, Y.; Su, H. B.; Wei, S. Q.; Xie, Y., Pits confined in ultrathin cerium(IV) oxide for studying catalytic centers in carbon monoxide oxidation. *Nat Commun* **2013,** *4*.

34. Bai, S.; Wang, X. J.; Hu, C. Y.; Xie, M. L.; Jiang, J.; Xiong, Y. J., Two-dimensional g-C_3N_4: an ideal platform for examining facet selectivity of metal co-catalysts in photocatalysis. *Chem Commun* **2014,** *50* (46), 6094-6097.

35. Lipkowski, J.; Ross, P. N., Electrocatalysis. **1998**.

36. Appleby, A. J., Electrocatalysis. *Comprehensive Treatise of Electrochemistry: Volume 7 Kinetics and Mechanisms of Electrode Processes* **1983**, 173-239.

37. Zhu, J.; Hu, L. S.; Zhao, P. X.; Lee, L. Y. S.; Wong, K. Y., Recent Advances in Electrocatalytic Hydrogen Evolution Using Nanoparticles. *Chem Rev* **2020,** *120* (2), 851-918.

38. Bard, A. J.; Faulkner, L. R.; White, H. S., *Electrochemical methods: fundamentals and applications*. John Wiley & Sons: 2022.

39. Eliaz, N.; Gileadi, E., *Physical electrochemistry: fundamentals, techniques, and applications*. John Wiley & Sons: 2019.

40. You, B.; Sun, Y. J., Innovative Strategies for Electrocatalytic Water Splitting. *Accounts Chem Res* **2018,** *51* (7), 1571-1580.

41. Chadderdon, X. H.; Chadderdon, D. J.; Matthiesen, J. E.; Qiu, Y.; Carraher, J. M.; Tessonnier, J. P.; Li, W. Z., Mechanisms of Furfural Reduction on Metal Electrodes: Distinguishing Pathways for Selective Hydrogenation of Bioderived Oxygenates. *J Am Chem Soc* **2017,** *139* (40), 14120-14128.

42. Akhade, S. A.; Singh, N.; Gutierrez, O. Y.; Lopez-Ruiz, J.; Wang, H. M.; Holladay, J. D.; Liu, Y.; Karkamkar, A.; Weber, R. S.; Padmaperuma, A. B.; Lee, M. S.; Whyatt, G. A.; Elliott, M.; Holladay, J. E.; Male, J. L.; Lercher, J. A.; Rousseau, R.; Glezakou, V. A., Electrocatalytic Hydrogenation of Biomass-Derived Organics: A Review. *Chem Rev* **2020,** *120* (20), 11370-11419.

43. Huang, H. J.; Yan, M. M.; Yang, C. Z.; He, H. Y.; Jiang, Q. G.; Yang, L.; Lu, Z. Y.; Sun, Z. Q.; Xu, X. T.; Bando, Y.; Yamauchi, Y., Graphene Nanoarchitectonics: Recent Advances in Graphene-Based Electrocatalysts for Hydrogen Evolution Reaction. *Adv Mater* **2019,** *31* (48).

44. Yin, H. J.; Dou, Y. H.; Chen, S.; Zhu, Z. J.; Liu, P. R.; Zhao, H. J., 2D Electrocatalysts for Converting Earth-Abundant Simple Molecules into Value-Added Commodity Chemicals: Recent Progress and Perspectives. *Adv Mater* **2020,** *32* (18).

45. Toh, R. J.; Sofer, Z.; Luxa, J.; Sedmidubsky, D.; Pumera, M., 3R phase of MoS_2 and WS_2 outperforms the corresponding 2H phase for hydrogen evolution. *Chem Commun* **2017,** *53* (21), 3054-3057.

46. Zhao, B.; Wan, Z.; Liu, Y.; Xu, J. Q.; Yang, X. D.; Shen, D. Y.; Zhang, Z. C.; Guo, C. H.; Qian, Q.; Li, J.; Wu, R. X.; Lin, Z. Y.; Yan, X. X.; Li, B. L.; Zhang, Z. W.; Ma, H. F.; Li, B.; Chen, X.; Qiao, Y.; Shakir, I.; Almutairi, Z.; Wei, F.; Zhang, Y.; Pan, X. Q.; Huang, Y.; Ping, Y.; Duan, X. D.; Duan, X. F., High-order superlattices by rolling up van der Waals heterostructures. *Nature* **2021,** *591* (7850), 385-+.

47. Lin, Z.; Carvalho, B. R.; Kahn, E.; Lv, R. T.; Rao, R.; Terrones, H.; Pimenta, M. A.; Terrones, M., Defect engineering of two-dimensional transition metal dichalcogenides. *2d Mater* **2016,** *3* (2).

48. Feng, C. Y.; Wu, Z. P.; Huang, K. W.; Ye, J. H.; Zhang, H. B., Surface Modification of 2D Photocatalysts for Solar Energy Conversion. *Adv Mater* **2022,** *34* (23).

49. Meng, C.; Chen, X. D.; Gao, Y. F.; Zhao, Q. Q.; Kong, D. Q.; Lin, M. C.; Chen, X. M.; Li, Y. X.; Zhou, Y., Recent Modification Strategies of MoS2 for Enhanced Electrocatalytic Hydrogen Evolution. *Molecules* **2020,** *25* (5).

50. Liu, Y. Y.; Wu, J. J.; Hackenberg, K. P.; Zhang, J.; Wang, Y. M.; Yang, Y. C.; Keyshar, K.; Gu, J.; Ogitsu, T.; Vajtai, R.; Lou, J.; Ajayan, P. M.; Wood, B. C.; Yakobson, B. I., Self-optimizing, highly surface-active layered metal dichalcogenide catalysts for hydrogen evolution. *Nat Energy* **2017,** *2* (9).

51. Hinnemann, B.; Moses, P. G.; Bonde, J.; Jørgensen, K. P.; Nielsen, J. H.; Horch, S.; Chorkendorff, I.; Nørskov, J. K., Biomimetic hydrogen evolution: MoS_2 nanoparticles as catalyst for hydrogen evolution. *J Am Chem Soc* **2005,** *127* (15), 5308-5309 %@ 0002-7863.

52. Jaramillo, T. F.; Jorgensen, K. P.; Bonde, J.; Nielsen, J. H.; Horch, S.; Chorkendorff, I., Identification of active edge sites for electrochemical H_2 evolution from MoS_2 nanocatalysts. *Science* **2007,** *317* (5834), 100-102.

53. Zhang, X.; Jia, F. F.; Song, S. X., Recent advances in structural engineering of molybdenum disulfide for electrocatalytic hydrogen evolution reaction. *Chem Eng J* **2021,** *405*.

54. Zhou, Q. S.; Feng, J. R.; Peng, X. W.; Zhong, L. X.; Sun, R. C., Porous carbon coupled with an interlaced MoP-MoS_2 heterojunction hybrid for efficient hydrogen evolution reaction. *J Energy Chem* **2020,** *45*, 45-51.

55. Li, H.; Tsai, C.; Koh, A. L.; Cai, L.; Contryman, A. W.; Fragapane, A. H.; Zhao, J.; Han, H. S.; Manoharan, H. C.; Abild-Pedersen, F., Activating and optimizing MoS_2 basal planes for hydrogen evolution through the formation of strained sulphur vacancies. *Nat Mater* **2016,** *15* (1), 48-53.

56. Chen, S. R.; Liu, X.; Xiong, J. B.; Mi, L. W.; Li, Y. Q., Engineering strategies for boosting the nitrogen reduction reaction performance of MoS_2-based electrocatalysts. *Mater Today Nano* **2022,** *18*.

57. Liu, J.; Kelley, M. S.; Wu, W. Q.; Banerjee, A.; Douvalis, A. P.; Wu, J. S.; Zhang, Y. B.; Schatz, G. C.; Kanatzidis, M. G., Nitrogenase-mimic iron-containing chalcogels for photochemical reduction of dinitrogen to ammonia. *P Natl Acad Sci USA* **2016,** *113* (20), 5530-5535.

58. Shi, S. L.; Sun, Z. X.; Hu, Y. H., Synthesis, stabilization and applications of 2-dimensional 1T metallic MoS_2. *J Mater Chem A* **2018,** *6* (47), 23932-23977.

59. Mohammadi, A. V.; Rosen, J.; Gogotsi, Y., The world of two-dimensional carbides and nitrides (MXenes). *Science* **2021,** *372* (6547), 1165-+.

60. Su, T. M.; Ma, X. H.; Tong, J. H.; Ji, H. B.; Qin, Z. Z.; Wu, Z. L., Surface engineering of MXenes for energy and environmental applications. *J Mater Chem A* **2022,** *10* (19), 10265-10296.

61. Kang, Z. M.; Khan, M. A.; Gong, Y. M.; Javed, R.; Xu, Y.; Ye, D. X.; Zhao, H. B.; Zhang, J. J., Recent progress of MXenes and MXene-based nanomaterials for the electrocatalytic hydrogen evolution reaction. *J Mater Chem A* **2021,** *9* (10), 6089-6108.

62. Allain, A.; Kang, J. H.; Banerjee, K.; Kis, A., Electrical contacts to two-dimensional semiconductors. *Nat Mater* **2015,** *14* (12), 1195-1205.

63. Pan, H., Ultra-high electrochemical catalytic activity of MXenes. *Sci Rep-Uk* **2016,** *6*.

64. Nemiwal, M.; Zhang, T. C.; Kumar, D., Graphene-based electrocatalysts: Hydrogen evolution reactions and overall water splitting. *Int J Hydrogen Energ* **2021,** *46* (41), 21401-21418.

65. Wang, F.; Mao, L. M.; Xie, H. T.; Mao, J., Graphene Derivatives and Graphene Composite Electrocatalysts for N_2 Reduction Reaction. *Small Struct* **2021,** *2* (2).

66. Sick, T.; Hufnagel, A. G.; Kampmann, J.; Kondofersky, I.; Calik, M.; Rotter, J. M.; Evans, A.; Doblinger, M.; Herbert, S.; Peters, K.; Bohm, D.; Knochel, P.; Medina, D. D.; Fattakhova-Rohlfing, D.; Bein, T., Oriented Films of Conjugated 2D Covalent Organic Frameworks as Photocathodes for Water Splitting. *J Am Chem Soc* **2018,** *140* (6), 2085-2092.

67. Ding, S. Y.; Gao, J.; Wang, Q.; Zhang, Y.; Song, W. G.; Su, C. Y.; Wang, W., Construction of Covalent Organic Framework for Catalysis: Pd/COF-LZU1 in Suzuki-Miyaura Coupling Reaction. *J Am Chem Soc* **2011,** *133* (49), 19816-19822.

68. Li, X. L.; Wang, Z. L.; Wang, L. Z., Metal-Organic Framework-Based Materials for Solar Water Splitting. *Small Sci* **2021,** *1* (5).

69. Xia, T. L.; Lin, Y. C.; Li, W. Z.; Ju, M. T., Photocatalytic degradation of organic pollutants by MOFs based materials: A review. *Chinese Chem Lett* **2021,** *32* (10), 2975-2984.

70. Xue, Y. P.; Zhao, G. C.; Yang, R. Y.; Chu, F.; Chen, J.; Wang, L.; Huang, X. B., 2D metal-organic framework-based materials for electrocatalytic, photocatalytic and thermocatalytic applications. *Nanoscale* **2021,** *13* (7), 3911-3936.

71. Chen, H.; Zhou, Y. S.; Guo, W.; Xia, B. Y., Emerging two-dimensional nanocatalysts for electrocatalytic hydrogen production. *Chinese Chem Lett* **2022,** *33* (4), 1831-1840.
72. Yang, J. H.; Wang, D. G.; Han, H. X.; Li, C., Roles of Cocatalysts in Photocatalysis and Photoelectrocatalysis. *Accounts Chem Res* **2013,** *46* (8), 1900-1909.
73. Zhang, F. B.; Wang, X. M.; Liu, H. N.; Liu, C. L.; Wan, Y.; Long, Y. Z.; Cai, Z. Y., Recent Advances and Applications of Semiconductor Photocatalytic Technology. *Appl Sci-Basel* **2019,** *9* (12).
74. Zhang, J.; Tian, B.; Wang, L.; Xing, M.; Lei, J.; Zhang, J.; Tian, B.; Wang, L.; Xing, M.; Lei, J., Mechanism of photocatalysis. *Photocatalysis: Fundamentals, Materials and Applications* **2018**, 1-15.
75. Bobo, M. V.; Kuchta, J. J.; Vannucci, A. K., Recent advancements in the development of molecular organic photocatalysts. *Org Biomol Chem* **2021,** *19* (22), 4816-4834.
76. Xiao, N.; Li, S. S.; Li, X. L.; Ge, L.; Gao, Y. Q.; Li, N., The roles and mechanism of cocatalysts in photocatalytic water splitting to produce hydrogen. *Chinese J Catal* **2020,** *41* (4), 642-671.
77. Yates, J. T., Photochemistry on TiO_2: Mechanisms behind the surface chemistry. *Surf Sci* **2009,** *603* (10-12), 1605-1612.
78. Wu, Y. Q.; Wang, P.; Zhu, X. L.; Zhang, Q. Q.; Wang, Z. Y.; Liu, Y. Y.; Zou, G. Z.; Dai, Y.; Whangbo, M. H.; Huang, B. B., Composite of $CH_3NH_3PbI_3$ with Reduced Graphene Oxide as a Highly Efficient and Stable Visible-Light Photocatalyst for Hydrogen Evolution in Aqueous HI Solution. *Adv Mater* **2018,** *30* (7).
79. Ding, M. Y.; Han, C. H.; Yuan, Y. J.; Xu, J. S.; Yang, X. F., Advances and Promises of 2D MXenes as Cocatalysts for Artificial Photosynthesis. *Sol Rrl* **2021,** *5* (12).
80. He, K. L.; Xie, J.; Yang, Z. H.; Shen, R. C.; Fang, Y. P.; Ma, S.; Chen, X. B.; Li, X., Earth-abundant WC nanoparticles as an active noble-metal-free co-catalyst for the highly boosted photocatalytic H_2 production over g-C_3N_4 nanosheets under visible light. *Catal Sci Technol* **2017,** *7* (5), 1193-1202.
81. Zhu, Q. H.; Xu, Z. H.; Qiu, B. C.; Xing, M. Y.; Zhang, J. L., Emerging Cocatalysts on g-C_3N_4 for Photocatalytic Hydrogen Evolution. *Small* **2021,** *17* (40).
82. Vinodgopal, K.; Kamat, P. V., Enhanced Rates of Photocatalytic Degradation of an Azo-Dye Using SnO_2/TiO_2 Coupled Semiconductor Thin-Films. *Environ Sci Technol* **1995,** *29* (3), 841-845.
83. Phoon, B. L.; Lai, C. W.; Juan, J. C.; Show, P. L.; Pan, G. T., Recent developments of strontium titanate for photocatalytic water splitting application. *Int J Hydrogen Energ* **2019,** *44* (28), 14316-14340.
84. Lin, S.; Huang, H. W.; Ma, T. Y.; Zhang, Y. H., Photocatalytic Oxygen Evolution from Water Splitting. *Adv Sci* **2021,** *8* (1).
85. Ma, D. G.; Zhai, S.; Wang, Y.; Liu, A. A.; Chen, C. C., TiO_2 Photocatalysis for Transfer Hydrogenation. *Molecules* **2019,** *24* (2).
86. Nahar, S.; Zain, M. F. M.; Kadhum, A. A. H.; Hasan, H. A.; Hasan, M. R., Advances in Photocatalytic CO_2 Reduction with Water: A Review. *Materials* **2017,** *10* (6).
87. Shehzad, N.; Tahir, M.; Johari, K.; Murugesan, T.; Hussain, M., A critical review on TiO_2 based photocatalytic CO_2 reduction system: Strategies to improve efficiency. *Journal of CO_2 Utilization* **2018,** *26*, 98-122.

88. Zhou, Y. S.; Wang, Z. T.; Huang, L.; Zaman, S.; Lei, K.; Yue, T.; Li, Z. A.; You, B.; Xia, B. Y., Engineering 2D Photocatalysts toward Carbon Dioxide Reduction. *Adv Energy Mater* **2021,** *11* (8).

89. Song, J. J.; Huang, Z. F.; Pan, L.; Li, K.; Zhang, X. W.; Wang, L.; Zou, J. J., Review on selective hydrogenation of nitroarene by catalytic, photocatalytic and electrocatalytic reactions. *Appl Catal B-Environ* **2018,** *227*, 386-408.

90. Daghrir, R.; Drogui, P.; Robert, D., Modified TiO_2 For Environmental Photocatalytic Applications: A Review. *Ind Eng Chem Res* **2013,** *52* (10), 3581-3599.

91. Zhao, Y. X.; Zhang, S.; Shi, R.; Waterhouse, G. I. N.; Tang, J. W.; Zhang, T. R., Two-dimensional photocatalyst design: A critical review of recent experimental and computational advances. *Mater Today* **2020,** *34*, 78-91.

92. Wu, C.; Zhang, J.; Tong, X.; Yu, P.; Xu, J. Y.; Wu, J.; Wang, Z. M. M.; Lou, J.; Chueh, Y. L., A Critical Review on Enhancement of Photocatalytic Hydrogen Production by Molybdenum Disulfide: From Growth to Interfacial Activities. *Small* **2019,** *15* (35).

93. Zhang, Y. C.; He, S.; Guo, W. X.; Hu, Y.; Huang, J. W.; Mulcahy, J. R.; Wei, W. D., Surface-Plasmon-Driven Hot Electron Photochemistry. *Chem Rev* **2018,** *118* (6), 2927-2954.

94. Liang, Z. Z.; Shen, R. C.; Ng, Y. H.; Zhang, P.; Xiang, Q. J.; Li, X., A review on 2D MoS_2 cocatalysts in photocatalytic H_2 production. *J Mater Sci Technol* **2020,** *56*, 89-121.

95. Peng, R.; Liang, L. B.; Hood, Z. D.; Boulesbaa, A.; Puretzky, A.; Ievlev, A. V.; Come, J.; Ovchinnikova, O. S.; Wang, H.; Ma, C.; Chi, M. F.; Sumpter, B. G.; Wu, Z. L., In-Plane Heterojunctions Enable Multiphasic Two-Dimensional (2D) MoS_2 Nanosheets As Efficient Photocatalysts for Hydrogen Evolution from Water Reduction. *Acs Catal* **2016,** *6* (10), 6723-6729.

96. Choi, J. H.; Cui, P.; Lan, H. P.; Zhang, Z. Y., Linear Scaling of the Exciton Binding Energy versus the Band Gap of Two-Dimensional Materials. *Phys Rev Lett* **2015,** *115* (6).

97. Wang, H.; Jin, S.; Zhang, X. D.; Xie, Y., Excitonic Effects in Polymeric Photocatalysts. *Angew Chem Int Edit* **2020,** *59* (51), 22828-22839.

98. Ong, W. J.; Tan, L. L.; Ng, Y. H.; Yong, S. T.; Chai, S. P., Graphitic Carbon Nitride (g-C_3N_4)-Based Photocatalysts for Artificial Photosynthesis and Environmental Remediation: Are We a Step Closer To Achieving Sustainability? *Chem Rev* **2016,** *116* (12), 7159-7329.

99. Sano, T.; Tsutsui, S.; Koike, K.; Hirakawa, T.; Teramoto, Y.; Negishi, N.; Takeuchi, K., Activation of graphitic carbon nitride (g-C_3N_4) by alkaline hydrothermal treatment for photocatalytic NO oxidation in gas phase. *J Mater Chem A* **2013,** *1* (21), 6489-6496.

100. Wang, X. C.; Maeda, K.; Thomas, A.; Takanabe, K.; Xin, G.; Carlsson, J. M.; Domen, K.; Antonietti, M., A metal-free polymeric photocatalyst for hydrogen production from water under visible light. *Nat Mater* **2009,** *8* (1), 76-80.

101. Sun, Y. F.; Cheng, H.; Gao, S.; Sun, Z. H.; Liu, Q. H.; Liu, Q.; Lei, F. C.; Yao, T.; He, J. F.; Wei, S. Q.; Xie, Y., Freestanding Tin Disulfide Single-Layers Realizing Efficient Visible-Light Water Splitting. *Angew Chem Int Edit* **2012,** *51* (35), 8727-8731.

102. Janczarek, M.; Kowalska, E., Defective Dopant-Free TiO_2 as an Efficient Visible Light-Active Photocatalyst. *Catalysts* **2021,** *11* (8).

103. Li, Z. J.; Raziq, F.; Liu, C.; Bai, L. L.; Jing, L. Q., Surface-engineering strategies for g-C_3N_4 as efficient visible-light photocatalyst. *Curr Opin Green Sust* **2017,** *6*, 57-62.

104. Iqbal, O.; Ali, H.; Li, N.; Al-Sulami, A. I.; Alshammari, K. F.; Abd-Rabboh, H. S. M.; Al-Hadeethi, Y.; Din, I. U.; Alharthi, A. I.; Altamimi, R.; Zada, A.; Wang, Z. Y.; Hayat, A.;

Ansari, M. Z., A review on the synthesis, properties, and characterizations of graphitic carbon nitride (g-C_3N_4) for energy conversion and storage applications. *Mater Today Phys* **2023,** *34*.

105. Majdoub, M.; Anfar, Z.; Amedlous, A., Emerging Chemical Functionalization of g-C_3N_4: Covalent/Noncovalent Modifications and Applications. *Acs Nano* **2020,** *14* (10), 12390-12469.

106. Xia, P. F.; Cheng, B.; Jiang, J. Z.; Tang, H., Localized pi-conjugated structure and EPR investigation of g-C_3N_4 photocatalyst. *Appl Surf Sci* **2019,** *487*, 335-342.

107. Haque, F.; Daeneke, T.; Kalantar-zadeh, K.; Ou, J. Z., Two-Dimensional Transition Metal Oxide and Chalcogenide-Based Photocatalysts. *Nano-Micro Lett* **2018,** *10* (2).

108. Sun, Z. Q.; Liao, T.; Dou, Y. H.; Hwang, S. M.; Park, M. S.; Jiang, L.; Kim, J. H.; Dou, S. X., Generalized self-assembly of scalable two-dimensional transition metal oxide nanosheets. *Nat Commun* **2014,** *5*.

109. Tang, R. D.; Xiong, S.; Gong, D. X.; Deng, Y. C.; Wang, Y. C.; Su, L.; Ding, C. X.; Yang, L. H.; Liao, C. J., Ti_3C_2 2D MXene: Recent Progress and Perspectives in Photocatalysis. *Acs Appl Mater Inter* **2020,** *12* (51), 56663-56680.

110. Sun, T.; Zhang, G. Q.; Xu, D.; Lian, X.; Li, H. X.; Chen, W.; Su, C. L., Defect chemistry in 2D materials for electrocatalysis. *Mater Today Energy* **2019,** *12*, 215-238.

111. Shao, W.; Zhang, X. D., Atomic-level engineering of two-dimensional electrocatalysts for CO_2 reduction. *Nanoscale* **2021,** *13* (15), 7081-7095.

112. Yu, X. N.; Ng, S. F.; Putri, L. K.; Tan, L. L.; Mohamed, A. R.; Ong, W. J., Point-Defect Engineering: Leveraging Imperfections in Graphitic Carbon Nitride (g-C_3N_4) Photocatalysts toward Artificial Photosynthesis. *Small* **2021,** *17* (48).

113. Banerjee, T.; Podjaski, F.; Kroger, J.; Biswal, B. P.; Lotsch, B. V., Polymer photocatalysts for solar-to-chemical energy conversion. *Nat Rev Mater* **2021,** *6* (2), 168-190.

114. Yan, D. F.; Li, Y. X.; Huo, J.; Chen, R.; Dai, L. M.; Wang, S. Y., Defect Chemistry of Nonprecious-Metal Electrocatalysts for Oxygen Reactions. *Adv Mater* **2017,** *29* (48).

115. Chen, S. C.; Wang, H.; Kang, Z. X.; Jin, S.; Zhang, X. D.; Zheng, X. S.; Qi, Z. M.; Zhu, J. F.; Pan, B. C.; Xie, Y., Oxygen vacancy associated single-electron transfer for photofixation of CO_2 to long-chain chemicals. *Nat Commun* **2019,** *10*.

116. Xiong, J.; Di, J.; Xia, J. X.; Zhu, W. S.; Li, H. M., Surface Defect Engineering in 2D Nanomaterials for Photocatalysis. *Adv Funct Mater* **2018,** *28* (39).

117. Li, H.; Du, M.; Mleczko, M. J.; Koh, A. L.; Nishi, Y.; Pop, E.; Bard, A. J.; Zheng, X. L., Kinetic Study of Hydrogen Evolution Reaction over Strained MoS_2 with Sulfur Vacancies Using Scanning Electrochemical Microscopy. *J Am Chem Soc* **2016,** *138* (15), 5123-5129.

118. Li, J. N.; Huang, J. H.; Zeng, G. M.; Zhang, C. Y.; Yu, H. B.; Wan, Q. F.; Yi, K. X.; Zhang, W.; Pang, H. L.; Liu, S.; Li, S. Z.; He, W. J., Efficient photosynthesis of H_2O_2 via two-electron oxygen reduction reaction by defective g-C3N4 with terminal cyano groups and nitrogen vacancies. *Chem Eng J* **2023,** *463*.

119. Liu, Y. W.; Cheng, H.; Lyu, M. J.; Fan, S. J.; Liu, Q. H.; Zhang, W. S.; Zhi, Y. D.; Wang, C. M.; Xiao, C.; Wei, S. Q.; Ye, B. J.; Xie, Y., Low Overpotential in Vacancy-Rich Ultrathin $CoSe_2$ Nanosheets for Water Oxidation. *J Am Chem Soc* **2014,** *136* (44), 15670-15675.

120. Li, Y. H.; He, Z. J.; Liu, L.; Jiang, Y.; Ong, W. J.; Duan, Y. Y.; Ho, W. K.; Dong, F., Inside-and-out modification of graphitic carbon nitride (g-C_3N_4) photocatalysts via defect engineering for energy and environmental science. *Nano Energy* **2023,** *105*.

121. Huang, S. Q.; Ge, F. Y.; Yan, J.; Li, H. P.; Zhu, X. W.; Xu, Y. G.; Xu, H.; Li, H. M., Synthesis of carbon nitride in moist environments: A defect engineering strategy toward superior photocatalytic hydrogen evolution reaction. *J Energy Chem* **2021,** *54*, 403-413.
122. Liu, H. J.; He, Q.; Jiang, H. L.; Lin, Y. X.; Zhang, Y. K.; Habib, M.; Chen, S. M.; Song, L., Electronic Structure Reconfiguration toward Pyrite NiS_2 via Engineered Heteroatom Defect Boosting Overall Water Splitting. *Acs Nano* **2017,** *11* (11), 11574-11583.
123. Li, Y.; Zuo, S. W.; Li, Q. H.; Wu, X.; Zhang, J.; Zhang, H. B.; Zhang, J., Vertically Aligned MoS_2 with In-Plane Selectively Cleaved Mo-S Bond for Hydrogen Production. *Nano Lett* **2021,** *21* (4), 1848-1855.
124. Li, H.; Tan, Y. W.; Liu, P.; Guo, C. G.; Luo, M.; Han, J. H.; Lin, T. Q.; Huang, F. Q.; Chen, M. W., Atomic-Sized Pores Enhanced Electrocatalysis of TaS_2 Nanosheets for Hydrogen Evolution. *Adv Mater* **2016,** *28* (40), 8945-8949.
125. Su, H.; Pan, X. D.; Li, S. Q.; Zhang, H.; Zou, R. Q., Defect-engineered two-dimensional transition metal dichalcogenides towards electrocatalytic hydrogen evolution reaction. *Carbon Energy* **2023**.
126. Lim, A.; Kim, J.; Lee, H. J.; Kim, H.-J.; Yoo, S. J.; Jang, J. H.; Young Park, H.; Sung, Y.-E.; Park, H. S., Low-loading IrO_2 supported on Pt for catalysis of PEM water electrolysis and regenerative fuel cells. *Applied Catalysis B: Environmental* **2020,** *272*, 118955.
127. Song, D.; Zheng, J.; Myung, N. V.; Xu, J.; Zhang, M., Sandwich-type electrochemical immunosensor for CEA detection using magnetic hollow Ni/C@SiO_2 nanomatrix and boronic acid functionalized CPS@PANI@Au probe. *Talanta* **2021,** *225*, 122006.
128. Chen, Z.; Duan, X.; Wei, W.; Wang, S.; Ni, B.-J., Electrocatalysts for acidic oxygen evolution reaction: Achievements and perspectives. *Nano Energy* **2020,** *78*, 105392.
129. Pham, C. V.; Bühler, M.; Knöppel, J.; Bierling, M.; Seeberger, D.; Escalera-López, D.; Mayrhofer, K. J. J.; Cherevko, S.; Thiele, S., IrO_2 coated TiO_2 core-shell microparticles advance performance of low loading proton exchange membrane water electrolyzers. *Applied Catalysis B: Environmental* **2020,** *269*, 118762.
130. Kumar, S. S.; Himabindu, V., Hydrogen production by PEM water electrolysis–A review. *Materials Science for Energy Technologies* **2019,** *2* (3), 442-454.
131. Lim, T.; Kim, S.-K., Non-precious hydrogen evolution reaction catalysts: Stepping forward to practical polymer electrolyte membrane-based zero-gap water electrolyzers. *Chem Eng J* **2021**, 133681.
132. Huang, H.; Kim, H.; Lee, A.; Kim, S.; Lim, W.-G.; Park, C.-Y.; Kim, S.; Kim, S.-K.; Lee, J., Structure engineering defective and mass transfer-enhanced RuO_2 nanosheets for proton exchange membrane water electrolyzer. *Nano Energy* **2021,** *88*, 106276.
133. Wang, S.; Lv, H.; Tang, F.; Sun, Y.; Ji, W.; Zhou, W.; Shen, X.; Zhang, C., Defect engineering assisted support effect:IrO2/N defective g-C_3N_4 composite as highly efficient anode catalyst in PEM water electrolysis. *Chem Eng J* **2021,** *419*, 129455.
134. Yang, G.; Yu, S.; Kang, Z.; Li, Y.; Bender, G.; Pivovar, B. S.; Green Jr, J. B.; Cullen, D. A.; Zhang, F.-Y., Building Electron/Proton Nanohighways for Full Utilization of Water Splitting Catalysts. *Adv Energy Mater* **2020,** *10* (16), 1903871.
135. Wei, J.; He, P.; Wu, J.; Chen, N.; Xu, T.; Shi, E.; Pan, C.; Zhao, X.; Zhang, Y., Conversion of 2H MoS_2 to 1 T MoS_2 via lithium ion doping: Effective removal of elemental mercury. *Chem Eng J* **2022,** *428*, 131014.

136. Gao, B.; Zhao, Y.; Du, X.; Li, D.; Ding, S.; Li, Y.; Xiao, C.; Song, Z., Electron injection induced phase transition of 2H to 1T MoS_2 by cobalt and nickel substitutional doping. *Chem Eng J* **2021,** *411*, 128567.

137. Xu, J.; Zhao, Z.; Wei, W.; Chang, G.; Xie, Z.; Guo, W.; Liu, D.; Qu, D.; Tang, H.; Li, J., Tuning the Intrinsic Activity and Electrochemical Surface Area of MoS_2 via Tiny Zn Doping: Toward an Efficient Hydrogen Evolution Reaction (HER) Catalyst. *Chemistry – A European Journal* **2021,** *27* (64), 15992-15999.

138. Le, K.; Zhang, X.; Zhao, Q.; Liu, Y.; Yi, P.; Xu, S.; Liu, W., Controllably Doping Nitrogen into 1T/2H MoS_2 Heterostructure Nanosheets for Enhanced Supercapacitive and Electrocatalytic Performance by Low-Power N_2 Plasma. *Acs Appl Mater Inter* **2021,** *13* (37), 44427-44439.

139. Chen, W.; Wang, Z.; Bets, K. V.; Luong, D. X.; Ren, M.; Stanford, M. G.; McHugh, E. A.; Algozeeb, W. A.; Guo, H.; Gao, G.; Deng, B.; Chen, J.; Li, J. T.; Carsten, W. T.; Yakobson, B. I.; Tour, J. M., Millisecond Conversion of Metastable 2D Materials by Flash Joule Heating. *Acs Nano* **2021,** *15* (1), 1282-1290.

140. Tang, Q.; Jiang, D. E., Mechanism of Hydrogen Evolution Reaction on 1T-MoS_2 from First Principles. *Acs Catal* **2016,** *6* (8), 4953-4961.

141. Holzapfel, P. K. R.; Bühler, M.; Escalera-López, D.; Bierling, M.; Speck, F. D.; Mayrhofer, K. J. J.; Cherevko, S.; Pham, C. V.; Thiele, S., Fabrication of a Robust PEM Water Electrolyzer Based on Non-Noble Metal Cathode Catalyst: $[Mo_3S\text{-}_{13}]^{2-}$ Clusters Anchored to N-Doped Carbon Nanotubes. *Small* **2020,** *16* (37), 2003161.

142. Ampurdanés, J.; Chourashiya, M.; Urakawa, A., Cobalt oxide-based materials as non-PGM catalyst for HER in PEM electrolysis and in situ XAS characterization of its functional state. *Catal Today* **2019,** *336*, 161-168.

143. Mo, J.; Wu, S.; Lau, T. H. M.; Kato, R.; Suenaga, K.; Wu, T. S.; Soo, Y. L.; Foord, J. S.; Tsang, S. C. E., Transition metal atom–doped monolayer MoS_2 in a proton-exchange membrane electrolyzer. *Materials Today Advances* **2020,** *6*, 100020.

144. Corrales-Sánchez, T.; Ampurdanés, J.; Urakawa, A., MoS_2-based materials as alternative cathode catalyst for PEM electrolysis. *Int J Hydrogen Energ* **2014,** *39* (35), 20837-20843.

145. Giovanni, C. D.; Reyes-Carmona, Á.; Coursier, A.; Nowak, S.; Grenèche, J. M.; Lecoq, H.; Mouton, L.; Rozière, J.; Jones, D.; Peron, J.; Giraud, M.; Tard, C., Low-Cost Nanostructured Iron Sulfide Electrocatalysts for PEM Water Electrolysis. *Acs Catal* **2016,** *6* (4), 2626-2631.

146. Xie, Z. Q.; Yu, S. L.; Ma, X. H.; Li, K.; Ding, L.; Wang, W. T.; Cullen, D. A.; Iii, H. M. M.; Yu, H. R.; Tong, J. H.; Wu, Z. L.; Zhang, F. Y., MoS_2 nanosheet integrated electrodes with engineered 1T-2H phases and defects for efficient hydrogen production in practical PEM electrolysis. *Appl Catal B-Environ* **2022,** *313*.

147. Liu, Z.; Gao, Z.; Liu, Y.; Xia, M.; Wang, R.; Li, N., Heterogeneous Nanostructure Based on 1T-Phase MoS_2 for Enhanced Electrocatalytic Hydrogen Evolution. *Acs Appl Mater Inter* **2017,** *9* (30), 25291-25297.

148. Lei, Z.; Zhan, J.; Tang, L.; Zhang, Y.; Wang, Y., Recent Development of Metallic (1T) Phase of Molybdenum Disulfide for Energy Conversion and Storage. *Adv Energy Mater* **2018,** *8* (19), 1703482.

149. Zhang, Y.; Kuwahara, Y.; Mori, K.; Louis, C.; Yamashita, H., Hybrid phase 1T/2H-MoS_2 with controllable 1T concentration and its promoted hydrogen evolution reaction. *Nanoscale* **2020,** *12* (22), 11908-11915.

150. Liu, Y.; Li, Y.; Peng, F.; Lin, Y.; Yang, S.; Zhang, S.; Wang, H.; Cao, Y.; Yu, H., 2H- and 1T- mixed phase few-layer MoS_2 as a superior to Pt co-catalyst coated on TiO_2 nanorod arrays for photocatalytic hydrogen evolution. *Applied Catalysis B: Environmental* **2019,** *241*, 236-245.

151. Wu, K.; Cao, X.; Li, M.; Lei, B.; Zhan, J.; Wu, M., Bottom-Up Synthesis of MoS_2/CNTs Hollow Polyhedron with 1T/2H Hybrid Phase for Superior Potassium-Ion Storage. *Small* **2020,** *16* (43), 2004178.

152. Yang, J.-C. E.; Zhu, M.-P.; Duan, X.; Wang, S.; Yuan, B.; Fu, M.-L., The mechanistic difference of 1T-2H MoS_2 homojunctions in persulfates activation: Structure-dependent oxidation pathways. *Applied Catalysis B: Environmental* **2021,** *297*, 120460.

153. Peng, R.; Liang, L.; Hood, Z. D.; Boulesbaa, A.; Puretzky, A.; Ievlev, A. V.; Come, J.; Ovchinnikova, O. S.; Wang, H.; Ma, C.; Chi, M.; Sumpter, B. G.; Wu, Z., In-Plane Heterojunctions Enable Multiphasic Two-Dimensional (2D) MoS2 Nanosheets As Efficient Photocatalysts for Hydrogen Evolution from Water Reduction. *Acs Catal* **2016,** *6* (10), 6723-6729.

154. Liu, X.; Guo, R.; Ni, K.; Xia, F.; Niu, C.; Wen, B.; Meng, J.; Wu, P.; Wu, J.; Wu, X.; Mai, L., Reconstruction-Determined Alkaline Water Electrolysis at Industrial Temperatures. *Adv Mater* **2020,** *32* (40), 2001136.

155. Liu, X.; Meng, J.; Zhu, J.; Huang, M.; Wen, B.; Guo, R.; Mai, L., Comprehensive Understandings into Complete Reconstruction of Precatalysts: Synthesis, Applications, and Characterizations. *Adv Mater* **2021,** *33* (32), 2007344.

156. Adofo, L. A.; Kim, H. J.; Agyapong-Fordjour, F. O.-T.; Thanh Nguyen, H. T.; Jin, J. W.; Kim, Y. I.; Kim, S. J.; Kim, J. H.; Boandoh, S.; Choi, S. H.; Lee, S. J.; Yun, S. J.; Kim, Y.-M.; Kim, S. M.; Han, Y.-K.; Kim, K. K., Hydrogen evolution reaction catalyst with high catalytic activity by interplay between organic molecules and transition metal dichalcogenide monolayers. *Mater Today Energy* **2022,** *25*, 100976.

157. Ye, Z. W.; Xu, Z. H.; Yue, W. H.; Liu, X. Y.; Wang, L. Z.; Zhang, J. L., Exploiting the LSPR effect for an enhanced photocatalytic hydrogen evolution reaction. *Phys Chem Chem Phys* **2023,** *25* (4), 2706-2716.

158. Tian, Y.; Tatsuma, T., Mechanisms and Applications of Plasmon-Induced Charge Separation at TiO2 Films Loaded with Gold Nanoparticles. *J Am Chem Soc* **2005,** *127* (20), 7632-7637.

159. Awazu, K.; Fujimaki, M.; Rockstuhl, C.; Tominaga, J.; Murakami, H.; Ohki, Y.; Yoshida, N.; Watanabe, T., A Plasmonic Photocatalyst Consisting of Silver Nanoparticles Embedded in Titanium Dioxide. *J Am Chem Soc* **2008,** *130* (5), 1676-1680.

160. Yang, J. L.; He, Y. L.; Ren, H.; Zhong, H. L.; Lin, J. S.; Yang, W. M.; Li, M. D.; Yang, Z. L.; Zhang, H.; Tian, Z. Q.; Li, J. F., Boosting Photocatalytic Hydrogen Evolution Reaction Using Dual Plasmonic Antennas. *Acs Catal* **2021,** *11* (9), 5047-5053.

161. Tada, H., Overall water splitting and hydrogen peroxide synthesis by gold nanoparticle-based plasmonic photocatalysts. *Nanoscale Adv* **2019,** *1* (11), 4238-4245.

162. Dao, D. V.; Nguyen, T. T. D.; Uthirakumar, P.; Cho, Y. H.; Kim, G. C.; Yang, J. K.; Tran, D. T.; Le, T. D.; Choi, H.; Kim, H. Y.; Yu, Y. T.; Lee, I. H., Insightful understanding of hot-carrier generation and transfer in plasmonic Au@CeO2 core-shell photocatalysts for light-driven hydrogen evolution improvement. *Appl Catal B-Environ* **2021,** *286*.

163. Pockrand, I.; Swalen, J. D.; Gordon, J. G.; Philpott, M. R., Surface-Plasmon Spectroscopy of Organic Monolayer Assemblies. *Surf Sci* **1978,** *74* (1), 237-244.

164. Kumar, A.; Choudhary, P.; Kumar, A.; Camargo, P. H. C.; Krishnan, V., Recent Advances in Plasmonic Photocatalysis Based on TiO(2) and Noble Metal Nanoparticles for Energy Conversion, Environmental Remediation, and Organic Synthesis. *Small* **2022,** *18* (1), e2101638.
165. Ma, X. C.; Dai, Y.; Yu, L.; Huang, B. B., Energy transfer in plasmonic photocatalytic composites. *Light Sci Appl* **2016,** *5* (2), e16017.
166. Ye, Z.; Xu, Z.; Yue, W.; Liu, X.; Wang, L.; Zhang, J., Exploiting the LSPR effect for an enhanced photocatalytic hydrogen evolution reaction. *Phys Chem Chem Phys* **2023**.
167. Linic, S.; Christopher, P.; Ingram, D. B., Plasmonic-metal nanostructures for efficient conversion of solar to chemical energy. *Nat Mater* **2011,** *10* (12), 911-921.
168. Ingram, D. B.; Linic, S., Water Splitting on Composite Plasmonic-Metal/Semiconductor Photoelectrodes: Evidence for Selective Plasmon-Induced Formation of Charge Carriers near the Semiconductor Surface. *J Am Chem Soc* **2011,** *133* (14), 5202-5205.
169. Erwin, W. R.; Zarick, H. F.; Talbert, E. M.; Bardhan, R., Light trapping in mesoporous solar cells with plasmonic nanostructures. *Energ Environ Sci* **2016,** *9* (5), 1577-1601.
170. Li, J. T.; Cushing, S. K.; Meng, F. K.; Senty, T. R.; Bristow, A. D.; Wu, N. Q., Plasmon-induced resonance energy transfer for solar energy conversion. *Nat Photonics* **2015,** *9* (9), 601-+.
171. Shi, Y.; Wang, J.; Wang, C.; Zhai, T.-T.; Bao, W.-J.; Xu, J.-J.; Xia, X.-H.; Chen, H.-Y., Hot Electron of Au Nanorods Activates the Electrocatalysis of Hydrogen Evolution on MoS2 Nanosheets. *J Am Chem Soc* **2015,** *137* (23), 7365-7370.
172. Irfan, I.; Golovynskyi, S.; Yeshchenko, O. A.; Bosi, M.; Zhou, T.; Xue, B.; Li, B. K.; Qu, J. L.; Seravalli, L., Plasmonic enhancement of exciton and trion photoluminescence in 2D MoS2 decorated with Au nanorods: Impact of nonspherical shape. *Physica E Low Dimens. Syst. Nanostruct.* **2022,** *140*, 115213.
173. Bar-Ziv, R.; Ranjan, P.; Lavie, A.; Jain, A.; Garai, S.; Bar Hen, A.; Popoyitz-Biro, R.; Tenne, R.; Arenal, R.; Ramasubramaniam, A.; Lajaunie, L.; Bar-Sadan, M., Au-MoS2 Hybrids as Hydrogen Evolution Electrocatalysts. *Acs Applied Energy Materials* **2019,** *2* (8), 6043-6050.
174. Garai, M.; Zhu, Z. Y.; Shi, J.; Li, S. S.; Xu, Q. H., Single-particle studies on plasmon enhanced photoluminescence of monolayer MoS2 by gold nanoparticles of different shapes. *Journal of Chemical Physics* **2021,** *155* (23).
175. Najmaei, S.; Mlayah, A.; Arbouet, A.; Girard, C.; Léotin, J.; Lou, J., Plasmonic Pumping of Excitonic Photoluminescence in Hybrid MoS2–Au Nanostructures. *Acs Nano* **2014,** *8* (12), 12682-12689.
176. Li, J.; Chen, Z.; Yang, H.; Yi, Z.; Chen, X.; Yao, W.; Duan, T.; Wu, P.; Li, G.; Yi, Y., Tunable Broadband Solar Energy Absorber Based on Monolayer Transition Metal Dichalcogenides Materials Using Au Nanocubes. *Nanomaterials (Basel)* **2020,** *10* (2).
177. Yu, Y.; Ji, Z.; Zu, S.; Du, B.; Kang, Y.; Li, Z.; Zhou, Z.; Shi, K.; Fang, Z., Ultrafast Plasmonic Hot Electron Transfer in Au Nanoantenna/MoS2 Heterostructures. *Adv Funct Mater* **2016,** *26* (35), 6394-6401.
178. Yang, X.; Liu, W.; Xiong, M.; Zhang, Y.; Liang, T.; Yang, J.; Xu, M.; Ye, J.; Chen, H., Au nanoparticles on ultrathin MoS2 sheets for plasmonic organic solar cells. *J Mater Chem A* **2014,** *2* (36), 14798-14806.
179. Kang, Y.; Najmaei, S.; Liu, Z.; Bao, Y.; Wang, Y.; Zhu, X.; Halas, N. J.; Nordlander, P.; Ajayan, P. M.; Lou, J.; Fang, Z., Plasmonic Hot Electron Induced Structural Phase Transition in a MoS2 Monolayer. *Adv Mater* **2014,** *26* (37), 6467-6471.

180. Rani, A.; Patel, A. S.; Chakraborti, A.; Singh, K.; Sharma, P., Enhanced photocatalytic activity of plasmonic Au nanoparticles incorporated MoS2 nanosheets for degradation of organic dyes. *Journal of Materials Science-Materials in Electronics* **2021,** *32* (5), 6168-6184.
181. Thimsen, E.; Le Formal, F.; Grätzel, M.; Warren, S. C., Influence of Plasmonic Au Nanoparticles on the Photoactivity of Fe2O3 Electrodes for Water Splitting. *Nano Lett* **2011,** *11* (1), 35-43.
182. Collins, G.; Lonergan, A.; McNulty, D.; Glynn, C.; Buckley, D.; Hu, C. Y.; O'Dwyer, C., Semiconducting Metal Oxide Photonic Crystal Plasmonic Photocatalysts. *Adv Mater Interfaces* **2020,** *7* (8), 1901805.
183. Li, J. T.; Cushing, S. K.; Bright, J.; Meng, F. K.; Senty, T. R.; Zheng, P.; Bristow, A. D.; Wu, N. Q., Ag@Cu2O Core-Shell Nanoparticles as Visible-Light Plasmonic Photocatalysts. *Acs Catal* **2013,** *3* (1), 47-51.
184. Yue, X.; Hou, J.; Zhang, Y.; Wu, P.; Guo, Y.; Peng, S.; Liu, Z.; Jiang, H., Improved CdS photocatalytic H(2) evolution using Au-Ag nanoparticles with tunable plasmon-enhanced resonance energy transfer. *Dalton Trans* **2020,** *49* (22), 7467-7473.
185. Skrabalak, S. E.; Au, L.; Li, X. D.; Xia, Y. N., Facile synthesis of Ag nanocubes and Au nanocages. *Nat Protoc* **2007,** *2* (9), 2182-2190.
186. Zhang, H. M.; Zhu, T.; Li, M., Quantitative Analysis of the Shape Effect of Thermoplasmonics in Gold Nanostructures. *J Phys Chem Lett* **2023,** *14* (16), 3853-3860.
187. Zhang, Q.; Li, W.; Wen, L. P.; Chen, J.; Xia, Y., Facile synthesis of Ag nanocubes of 30 to 70 nm in edge length with CF3COOAg as a precursor. *Chem-Eur J* **2010,** *16* (33), 10234-10239.
188. Skrabalak, S. E.; Au, L.; Li, X.; Xia, Y., Facile synthesis of Ag nanocubes and Au nanocages. *Nat Protoc* **2007,** *2* (9), 2182.
189. Skrabalak, S. E.; Chen, J.; Sun, Y.; Lu, X.; Au, L.; Cobley, C. M.; Xia, Y., Gold nanocages: synthesis, properties, and applications. *Accounts Chem Res* **2008,** *41* (12), 1587-1595.
190. Boulesbaa, A.; Huang, B.; Wang, K.; Lin, M.-W.; Mahjouri-Samani, M.; Rouleau, C.; Xiao, K.; Yoon, M.; Sumpter, B.; Puretzky, A.; Geohegan, D., Observation of two distinct negative trions in tungsten disulfide monolayers. *Phys Rev B* **2015,** *92* (11), 115443.
191. Lee, C.; Yan, H.; Brus, L. E.; Heinz, T. F.; Hone, J.; Ryu, S., Anomalous Lattice Vibrations of Single- and Few-Layer MoS2. *Acs Nano* **2010,** *4* (5), 2695-2700.
192. Gupta, U.; Naidu, B. S.; Maitra, U.; Singh, A.; Shirodkar, S. N.; Waghmare, U. V.; Rao, C. N. R., Characterization of few-layer 1T-$MoSe_2$ and its superior performance in the visible-light induced hydrogen evolution reaction. *Apl Mater* **2014,** *2* (9), 092802.
193. Eda, G.; Yamaguchi, H.; Voiry, D.; Fujita, T.; Chen, M.; Chhowalla, M., Photoluminescence from Chemically Exfoliated MoS2. *Nano Lett* **2011,** *11* (12), 5111-5116.
194. Mubeen, S.; Lee, J.; Singh, N.; Krämer, S.; Stucky, G. D.; Moskovits, M., An autonomous photosynthetic device in which all charge carriers derive from surface plasmons. *Nat Nanotechnol* **2013,** *8*, 247.
195. Linic, S.; Christopher, P.; Ingram, D. B., Plasmonic-metal nanostructures for efficient conversion of solar to chemical energy. *Nat Mater* **2011,** *10*, 911.
196. Yu, Y.; Yu, Y.; Cai, Y.; Li, W.; Gurarslan, A.; Peelaers, H.; Aspnes, D. E.; Van de Walle, C. G.; Nguyen, N. V.; Zhang, Y.-W.; Cao, L., Exciton-dominated Dielectric Function of Atomically Thin MoS2 Films. *Sci Rep-Uk* **2015,** *5*, 16996.

197. Sim, S.; Park, J.; Song, J.-G.; In, C.; Lee, Y.-S.; Kim, H.; Choi, H., Exciton dynamics in atomically thin MoS$${}_{2}$: Interexcitonic interaction and broadening kinetics. *Physical Review B* **2013,** *88* (7), 075434.

198. Eroglu, Z. E.; Contreras, D.; Bahrami, P.; Azam, N.; Mahjouri-Samani, M.; Boulesbaa, A., Filling Exciton Trap-States in Two-Dimensional Tungsten Disulfide (WS2) and Diselenide (WSe2) Monolayers. *Nanomaterials-Basel* **2021,** *11* (3), 770.

199. Eroglu, Z. E.; Comegys, O.; Quintanar, L. S.; Azam, N.; Elafandi, S.; Mahjouri-Samani, M.; Boulesbaa, A., Ultrafast dynamics of exciton formation and decay in two-dimensional tungsten disulfide (2D-WS_2) monolayers. *Phys Chem Chem Phys* **2020,** *22* (30), 17385-17393.

200. Li, C. J.; Chai, O. J. H.; Yao, Q. F.; Liu, Z. H.; Wang, L.; Wang, H. J.; Xie, J. P., Electrocatalysis of gold-based nanoparticles and nanoclusters. *Mater Horiz* **2021,** *8* (6), 1657-1682.

201. Vergunst, T.; Kapteijn, F.; Moulijn, J. A., Optimization of geometric properties of a monolithic catalyst for the selective hydrogenation of phenylacetylene. *Ind Eng Chem Res* **2001,** *40* (13), 2801-2809.

202. Dominguez-Dominguez, S.; Berenguer-Murcia, A.; Cazorla-Amoros, D.; Linares-Solano, A., Semihydrogenation of phenylacetylene catalyzed by metallic nanoparticles containing noble metals. *J Catal* **2006,** *243* (1), 74-81.

203. Dominguez-Dominguez, S.; Berenguer-Murcia, W.; Pradhan, B. K.; Linares-Solano, A.; Cazorla-Amoros, D., Semihydrogenation of phenylacetylene catalyzed by palladium nanoparticles supported on carbon materials. *J Phys Chem C* **2008,** *112* (10), 3827-3834.

204. Arena, F.; Cum, G.; Gallo, R.; Parmaliana, A., Palladium catalysts supported on oligomeric aramides in the liquid-phase hydrogenation of phenylacetylene. *J Mol Catal a-Chem* **1996,** *110* (3), 235-242.

205. Huang, Y.; Yan, H.; Zhang, C.; Wang, Y.; Wei, Q.; Zhang, R., Interfacial Electronic Effects in Co@N-Doped Carbon Shells Heterojunction Catalyst for Semi-Hydrogenation of Phenylacetylene. *Nanomaterials (Basel)* **2021,** *11* (11).

206. Wang, X. D.; Keane, M. A., Gas phase selective hydrogenation of phenylacetylene to styrene over Au/Al2O3. *J Chem Technol Biot* **2019,** *94* (12), 3772-3779.

207. Li, Z. X.; Hu, M. L.; Liu, J. H.; Wang, W. W.; Li, Y. J.; Fan, W. B.; Gong, Y. X.; Yao, J. S.; Wang, P.; He, M.; Li, Y. L., Mesoporous silica stabilized MOF nanoreactor for highly selective semi-hydrogenation of phenylacetylene via synergistic effect of Pd and Ru single site. *Nano Research* **2022,** *15* (3), 1983-1992.

208. Fan, Q.; He, S.; Hao, L.; Liu, X.; Zhu, Y.; Xu, S.; Zhang, F., Photodeposited Pd Nanoparticles with Disordered Structure for Phenylacetylene Semihydrogenation. *Sci Rep* **2017,** *7*, 42172.

209. Wang, Y.; Chen, Z.; Shen, R. G.; Cao, X.; Chen, Y. G.; Chen, C.; Wang, D. S.; Peng, Q.; Li, Y. D., Pd-dispersed CuS hetero-nanoplates for selective hydrogenation of phenylacetylene. *Nano Research* **2016,** *9* (4), 1209-1219.

210. Huang, Y. M.; Liu, Z.; Gao, G. P.; Xiao, Q.; Martens, W.; Du, A. J.; Sarina, S.; Guo, C.; Zhu, H. Y., Visible light-driven selective hydrogenation of unsaturated aromatics in an aqueous solution by direct photocatalysis of Au nanoparticles. *Catal Sci Technol* **2018,** *8* (3), 726-734.

211. Wang, Z. W.; Wang, H.; Shi, Y. Z.; Liu, C.; Wu, L., CuPd alloy decorated SnNb2O6 nanosheets as a multifunctional photocatalyst for semihydrogenation of phenylacetylene under visible light. *Chem Eng J* **2022,** *429*.
212. Kominami, H.; Higa, M.; Nojima, T.; Ito, T.; Nakanishi, K.; Hashimoto, K.; Imamura, K., Copper-Modified Titanium Dioxide: A Simple Photocatalyst for the Chemoselective and Diastereoselective Hydrogenation of Alkynes to Alkenes under Additive-Free Conditions. *Chemcatchem* **2016,** *8* (12), 2019-2022.
213. Jia, T. T.; Meng, D.; Ji, H. W.; Sheng, H.; Chen, C. C.; Song, W. J.; Zhao, J. C., Visible-light-driven semihydrogenation of alkynes via proton reduction over carbon nitride supported nickel. *Appl Catal B-Environ* **2022,** *304*.
214. Lian, J. H.; Chai, Y. C.; Qi, Y.; Guo, X. Y.; Guan, N. J.; Li, L. D.; Zhang, F. X., Unexpectedly selective hydrogenation of phenylacetylene to styrene on titania supported platinum photocatalyst under 385 nm monochromatic light irradiation. *Chinese J Catal* **2020,** *41* (4), 598-603.
215. Bi, Q. Y.; Song, E. H.; Chen, J. C.; Riaz, M. S.; Zhu, M. H.; Liu, J. J.; Han, Y. F.; Huang, F. Q., Nano gold coupled black titania composites with enhanced surface plasma properties for efficient photocatalytic alkyne reduction. *Appl Catal B-Environ* **2022,** *309*.
216. Wang, J.; Wang, M. X.; Li, X. C.; Gu, X. M.; Kong, P.; Wang, R. Y.; Ke, X. B.; Yu, G. T.; Zheng, Z. F., Bidentate ligand modification strategy on supported Ni nanoparticles for photocatalytic selective hydrogenation of alkynes. *Appl Catal B-Environ* **2022,** *313*.
217. Su, K. Y.; Wang, Y. H.; Zhang, C. F.; Gao, Z. Y.; Han, J. Y.; Wang, F., Tuning the Pt species on Nb2O5 by support-induced modification in the photocatalytic transfer hydrogenation of phenylacetylene. *Appl Catal B-Environ* **2021,** *298*.
218. Dong, S. Y.; Feng, J. L.; Fan, M. H.; Pi, Y. Q.; Hu, L. M.; Han, X.; Liu, M. L.; Sun, J. Y.; Sun, J. H., Recent developments in heterogeneous photocatalytic water treatment using visible light-responsive photocatalysts: a review. *Rsc Adv* **2015,** *5* (19), 14610-14630.
219. Djurisic, A. B.; He, Y. L.; Ng, A. M. C., Visible-light photocatalysts: Prospects and challenges. *Apl Mater* **2020,** *8* (3).
220. Pelaez, M.; Nolan, N. T.; Pillai, S. C.; Seery, M. K.; Falaras, P.; Kontos, A. G.; Dunlop, P. S. M.; Hamilton, J. W. J.; Byrne, J. A.; O'Shea, K.; Entezari, M. H.; Dionysiou, D. D., A review on the visible light active titanium dioxide photocatalysts for environmental applications. *Appl Catal B-Environ* **2012,** *125*, 331-349.
221. Bai, S.; Zhang, N.; Gao, C.; Xiong, Y. J., Defect engineering in photocatalytic materials. *Nano Energy* **2018,** *53*, 296-336.
222. Pan, R. R.; Liu, J.; Zhang, J. T., Defect Engineering in 2D Photocatalytic Materials for CO2 Reduction. *Chemnanomat* **2021,** *7* (7), 737-747.
223. Li, Y. M.; Zhong, J. B.; Li, J. Z., Rich carbon vacancies facilitated solar light-driven photocatalytic hydrogen generation over g-C_3N_4 treated in H2 atmosphere. *Int J Hydrogen Energ* **2022,** *47* (94), 39886-39897.
224. Liu, G. M.; Huang, Y.; Lv, H. Q.; Wang, H.; Zeng, Y. B.; Yuan, M. Z.; Meng, Q. G.; Wang, C. Y., Confining single-atom Pd on g-C_3N_4 with carbon vacancies towards enhanced photocatalytic NO conversion. *Appl Catal B-Environ* **2021,** *284*.
225. Zhou, P.; Lv, F.; Li, N.; Zhang, Y. L.; Mu, Z. J.; Tang, Y. H.; Lai, J. P.; Chao, Y. G.; Luo, M. C.; Lin, F.; Zhou, J. H.; Su, D.; Guo, S. J., Strengthening reactive metal-support interaction to stabilize high-density Pt single atoms on electron-deficient g-C_3N_4 for boosting photocatalytic H_2 production. *Nano Energy* **2019,** *56*, 127-137.

226. Liu, H.; Yu, D. Q.; Sun, T. B.; Du, H. Y.; Jiang, W. T.; Muhammad, Y.; Huang, L., Fabrication of surface alkalinized g-C_3N_4 and TiO_2 composite for the synergistic adsorption-photocatalytic degradation of methylene blue. *Appl Surf Sci* **2019,** *473*, 855-863.
227. Ong, W. J.; Tan, L. L.; Chai, S. P.; Yong, S. T.; Mohamed, A. R., Surface charge modification via protonation of graphitic carbon nitride (g-C_3N_4) for electrostatic self-assembly construction of 2D/2D reduced graphene oxide (rGO)/g-C_3N_4 nanostructures toward enhanced photocatalytic reduction of carbon dioxide to methane. *Nano Energy* **2015,** *13*, 757-770.
228. Zhu, B. C.; Xia, P. F.; Ho, W. K.; Yu, J. G., Isoelectric point and adsorption activity of porous g-C_3N_4. *Appl Surf Sci* **2015,** *344*, 188-195.
229. Zhang, L. L.; Zhou, M. X.; Wang, A. Q.; Zhang, T., Selective Hydrogenation over Supported Metal Catalysts: From Nanoparticles to Single Atoms. *Chem Rev* **2020,** *120* (2), 683-733.

PUBLICATIONS

1. **Co-first author:** Xie, Z., Yu, S., **Ma, X.**, Li, K., Ding, L., Wang, W., ... & Zhang, F. Y. (2022). MoS_2 nanosheet integrated electrodes with engineered 1T-2H phases and defects for efficient hydrogen production in practical PEM electrolysis. *Applied Catalysis B: Environmental*, 313, 121458.
2. **Co-first author:** Su, T., **Ma, X.**, Tong, J., Ji, H., Qin, Z. Z., & Wu, Z. (2022). Surface engineering of MXenes for energy and environmental applications. *Journal of Materials Chemistry A*, 10 (19), 10265-10296.
3. **Co-first author:** Peng, R., **Ma, X.**, Hood, Z. D., Boulesbaa, A., Puretzky, A. A., Tong, J., & Wu, Z. (2023). Synergizing plasmonic Au nanocages with 2D MoS 2 nanosheets for significant enhancement in photocatalytic hydrogen evolution. *Journal of Materials Chemistry A*, *11*(31), 16714-16723.
4. **Co-author:** Kammert, J., Moon, J., Cheng, Y., Daemen, L., Irle, S., Fung, V., **Ma, X.**, ... & Wu, Z. (2020). Nature of reactive hydrogen for ammonia synthesis over a Ru/C12A7 electride catalyst. *Journal of the American Chemical Society*, 142(16), 7655-7667.
5. **Manuscript in progress:** Enhancing the photocatalytic semi-hydrogenation of phenylacetylene by tuning synergy between nickel sites and surface vacancies of Ni/g-C_3N_4.